UNIVERSITÀ DEGLI STUDI
DI MODENA E REGGIO EMILIA

"ENZO FERRARI" Ph.D. COURSE
IN INDUSTRIAL AND ENVIRONMENTAL ENGINEERING

Cycle XXXV

Development of an automotive wheel rim with non-conventional materials

Candidate: Michele ZANCHINI

Tutor: Prof.ssa Sara MANTOVANI
Co-Tutor: Prof. Matteo GIACOPINI

Coordinator of the PhD Course: Prof. Alberto MUSCIO

Title: Development of an automotive wheel rim with non-conventional materials

Key-words (MAX 5): automotive, wheels, composites, aluminium, fatigue, *(corrosion, thermal)*

Abstract (UK):

In the last decades of sports passenger cars field, aluminium alloys were selected as the most suitable material for the wheel rims manufacturing. These alloys are inherently lightweight, stiff and provide a good stylistic and design freedom.

While steel wheels are now mostly adopted for commercial vehicles with a not comparable weight performance with respect to the aluminium one, magnesium alloys wheels have always struggled to break through the market for economic reasons, technological challenges and corrosion issues.

This thesis deals with the adoption of composite materials in the design of wheel.

The use of these materials into wheel rims development represents an innovation for the automotive market which has required a deep review of the OEM type-approval standards. Furthermore, a detailed Failure Mode and Effect Analysis (FMEA) at the very beginning of the project has been needed.

The resulting composite wheel has been manufactured with two different types of cores made from randomly oriented short carbon fibres and from polyurethane foam. These cores are coupled with unidirectional and plain weave carbon fibre plies, embedded into epoxy matrix injected via Resin Transfer Moulding (RTM).

Five relevant topics come up from FMEA, reflecting the weaknesses of the material for this application: the rolling on the roughness of ground, the withstanding of vertical loads while dealing with transmission of high lateral loads, the wheels fastening on vehicle, the thermal loads generated from sudden braking manoeuvres and the environmental aging.

These aspects have been critically analysed and discussed by comparing the composites wheel with a forged aluminium wheel.

Aluminium alloy and Carbon Fibre Reinforced Polymer (CFRP) exhibit different behaviour both under fatigue and under impact loads. First, the aluminium alloys behave as isotropic materials, whereas CFRP behave as orthotropic ones. This peculiarity of composites increases the complexity of numerical simulations performed during the design of the wheel on mimicking its failures.

The wheel fastening to the suspension is crucial. The minimum tightening preload to keep the wheel in contact with the vehicle hub has been provided, and the stiffness of the bolted joint has been analysed on the loading distribution.

On the thermal loads admissible by composites, a detailed analysis of the track performance of a sports vehicle has been carried out. The maximum temperature needs to be lower than the glass transition temperature of the matrix. Since higher temperatures

have been collected, the composite wheel has been safeguarded by a protective plasma spray coating. Its effectiveness has been validated by experimental tests.

Finally, to ensure the safety of the component during daily use, corrosion tests have been carried out to avoid aesthetic damages and the dangerous effects of stress corrosion cracking.

In conclusion, the result of all these tests has brought to the development of a non-conventional wheel 28% lighter than the reference forged aluminium wheel and with similar stiffness.

This design has proved that the composites and the RTM technology are ready for high-performance automotive applications.

Titolo Italiano: Sviluppo di un cerchio ruota per autovettura con materiali non convenzionali

Parole chiave (MAX 5): automotive, cerchi, compositi, alluminio, fatica

Abstract (ITA):

Negli ultimi decenni nel campo delle autovetture sportive, le leghe di alluminio sono state scelte come il materiale più idoneo per la realizzazione dei cerchi ruota. Queste leghe sono intrinsecamente leggere, rigide e offrono una buona libertà stilistica e progettuale.

Mentre le ruote in acciaio sono oggi perlopiù adottate per veicoli commerciali con prestazioni di peso non paragonabili a quelle in alluminio, le ruote in lega di magnesio hanno sempre faticato a conquistare il mercato per motivi economici, produttivi e per problemi di corrosione.

Questa tesi si occupa dell'adozione dei materiali compositi nella progettazione delle ruote.

L'uso di tali materiali nello sviluppo dei cerchi ruota rappresenta un'innovazione mondiale per il mercato automobilistico e ciò ha comportato un'importante revisione degli standard di omologazione dell'OEM. Inoltre, questa progettazione ha reso necessaria un'analisi dettagliata della Failure Mode and Effect Analysis (FMEA).

La ruota in composito risultante è stata prodotta con due diversi tipi di riempitivi realizzati con fibre di carbonio corte orientate casualmente e con schiuma di poliuretano. Tali riempitivi sono accoppiati con strati di fibra di carbonio unidirezionali e incrociati, incorporati in una matrice epossidica iniettata tramite la tecnologia Resin Transfer Moulding (RTM).

Dalla FMEA emergono cinque temi rilevanti che riflettono i punti deboli del materiale per questa applicazione: il rotolamento sulle asperità del terreno, la resistenza ai carichi verticali mentre si affronta la trasmissione di elevati carichi laterali, il fissaggio delle ruote al veicolo, i carichi termici generati dalle brusche frenate e l'invecchiamento ambientale.

Questi aspetti sono stati analizzati e discussi confrontando la ruota in composito con una ruota in alluminio forgiato.

La lega di alluminio e il polimero rinforzato con la fibra di carbonio (CFRP) mostrano un comportamento diverso quando sottoposte a carichi affaticanti e a carichi di impatto. Infatti, le leghe di alluminio si comportano come materiali isotropi, mentre i CFRP si comportano come materiali ortotropi. Questa peculiarità dei compositi aumenta la complessità delle simulazioni numeriche eseguite durante la progettazione della ruota simulandone i guasti.

Il fissaggio della ruota alla sospensione è fondamentale; è stato calcolato il precarico minimo di serraggio per mantenere la ruota a contatto con il mozzo del veicolo ed è stata analizzata la rigidezza del giunto imbullonato sulla distribuzione del carico.

Da un'analisi dettagliata delle prestazioni in pista di un veicolo sportivo sui carichi termici ammissibili dai compositi è emerso che la temperatura massima deve essere inferiore alla temperatura di transizione vetrosa della matrice. Poiché sono state raccolte temperature più elevate, la ruota composita è stata protetta da un rivestimento protettivo al *"plasma spray"*. La sua efficacia è convalidata da prove sperimentali.

Infine, per garantire la sicurezza del componente durante l'uso quotidiano, sono state effettuate prove di corrosione per evitare i danni estetici e i pericolosi effetti di tenso-corrosione.

In conclusione, il risultato di tutti questi test ha portato allo sviluppo di una ruota in materiale non convenzionale più leggera del 28% rispetto alla ruota di riferimento in alluminio forgiato con simile rigidezza.

Questo progetto ha dimostrato che i compositi e la tecnologia RTM sono pronti per applicazioni automobilistiche ad alte prestazioni.

Summary

Chapter 1
INTRODUCTION

1.1 A brief of history: behind the idea

The on-line Merriam-Webster dictionary [1] defines wheel as "*a circular frame of hard material that may be solid, partly solid, or spoked and that is capable of turning on an axle*". The wheel was born way before motor vehicles [2,3], being the first historical evidence of a wheeled vehicle found in Mesopotamia (3500 B.C).

The wheel's main function was to support weight, but after the advent of the propulsion on the vehicle itself, a new function of transmitting the loads generated by the vehicle to the ground has been added. The first metal wheels for motor vehicles appeared in the 1920s: they were cast from steel and characterised by a cyclic pattern of solid spokes. They have progressively been substituted in favour of aluminium or magnesium alloys. Nowadays, the wheels of road vehicles may be distinct in spoke-type and disk-type wheels. Steel wheels are still adopted for heavy-duty or for large-series production vehicles with a disk-type design. In the last decades, another new function has taken considerable importance: aesthetics. Wheels do up to 25% of the aesthetics of a vehicle, they are literally considered by car designers as "the shoes" of the vehicle. Also for this reason, steel wheels with disk-type design have progressively been substituted in favour of aluminium alloys with spoke-style design. Moreover, vehicles are designed to strike a balance between daily comfort, cost-effectiveness for end-users, and environmental sustainability by minimizing emissions and fuel consumption. These are now essential requirements of automobiles, and wheels must play their part in achieving them.

During their motion, wheels are subjected to dynamic, impact and fatigue loads [3,4]; unexpected wheel failure could lead to the driver losing control of the vehicle, potentially resulting in severe consequences. Therefore, over the years, to improve wheel design a list of testing with different durability and impact loading conditions have been developed and then, employed: radial, cornering [5–9] and biaxial fatigue [10–12].

The literature largely deals with cornering fatigue about failures and designs of spoke-type metal wheels [13–15]. Ballo *et al.* [13] found a crack at the root of one spoke after 3.5 million cycles in an aluminium A356-T6 wheel. The crack originated from the inner edge at the root of one spoke. Also Shang *et al.* [14] experienced a similar failure. Raju *et al.* [15] found a crack near the bolt holes on the hub housing, in contrast to a different outcome observed by previous researchers. From these examples, it's clear that the wheel style and its design highly influence the crack location.

Through the use of stress-life (S-N) method, the development of Finite Element (FE) simulation in fatigue testing has enabled the prediction of areas prone to failure in the wheel [13–16]. The criteria adopted include Sines and Matake [13], Goodman [14], and equivalent stress amplitude [16]. Firat *et al.* [17] proposed an alternative approach that involves forecasting the wheel damage with a strain-life method. The fatigue resistance can be well predicted by using the Fatemi-Socie parameter.

About disk-type wheels, the scientific literature includes research on both finite element simulations [18–20] and experiments [21,22]. These wheels' critical spots include the bolted holes [23], the ventilation holes [24–26] and the weld seam connecting the disk and rim [22,27].

Radial fatigue of wheels is another experimental test extensively covered in the literature. Raju *et al.* [28] conducted simulation and physical test on an A356-T6 spoke-type wheel. The test outcome revealed that a fracture started from the root of the spoke and cut through the entire section. Another time, the fatigue life is estimated using a stress-life method in numerical simulation. The simulation results are correlated with the test outcomes. The design and estimation of the fatigue life for steel disk-type wheels are also discussed [25,27,29].

To improve the simulations' reliability, the material of the wheel needs to be sampled to get reliable data on the fatigue resistance [4,13,15,28,30] and every point of the wheel needs to be evaluated for critical stresses [12]. Furthermore, the importance of the manufacturing processes on the mechanical properties and fatigue characteristics of the wheel, for example stamping [31], punching [24], or rim interference fit [26,29] on disk-type wheels, or post-casting solidification [32] in spoke-type wheels, necessitates obtaining samples directly from the wheel. Undoubtedly, the microstructure as well as the defects caused by manufacturing have a significant impact on the overall fatigue resistance of the wheel as reported in [21,23,33].

Sports cars must deal also with "*fun-to-drive*" concept, which can be defined as the excitement produced by the responsiveness of the vehicle when subjected to sudden manoeuvres as the sudden braking or acceleration. Enhancing performance and this perception of responsiveness while maintaining ride comfort and fuel efficiency is an area of intense research for many sports vehicle manufacturers. Improving comfort means reduce the vertical acceleration of the body, and hence the driver and passengers [34]. The unsprung masses, including the wheels, are responsible for transferring vertical forces and accelerations from the road to the vehicle body [35]. According to the literature, a reduction in unsprung mass results in an enhancement of the ride comfort. Several research has been conducted on ride comfort optimization for in-wheel motor vehicles [36–39]. As reported by Hrovat *et al.* [40], lightweight has a positive effect on both passive and active suspensions. Besides, decreasing rotational inertia helps in reducing fuel consumption. Thus, it can be stated that the decrease in unsprung mass along with the reduction of rotational inertia is a definite benefit. Moreover, the demand for improved performance on both roads and racetracks in new sports cars has resulted in a general rise in the loads exerted on the wheels during operation.

To fulfil the various demands for lightweight and stylish wheel designs, two main approaches are used, namely, material selection [41,42] and structural optimization. The approaches of the latter are employed to achieve a light rim with variable thickness [43,44], optimal spoke topology [45,46], as well as enhanced vibration response [47] and impact resistance of the whole wheel [48,49].

Wheels designed for motorsports can benefit from the lightness and formability of magnesium alloys, which make them a preferred choice among the metals used for wheel

manufacturing [41,48,49]. Nevertheless, their low fatigue strength and poor galvanic corrosion resistance when compared to aluminium alloys have limited their adoption in the automotive sector.

Since the 1980s, composite materials have led to increased interest in the use in automotive applications, particularly for sports cars and racing vehicles, due to their high stiffness-to-weight ratio. However, the use of carbon fibre in the automotive industry has become more widespread in recent years due to advancements in manufacturing technology and increased demand for lightweight and high-performance materials. Recently, these materials have been taken into consideration for wheel design. The SAE J3204 standard [50] categorizes composite wheels into two categories: *hybrid* and *full composite wheels*. *Hybrid composite wheels* typically feature both metallic alloys and composite materials in either the rim or spokes [47,49,51], which are joined or bonded together. In contrast, *full composite wheels* are made entirely of composite materials, with both the rim and spokes composed of such materials [45,52,53]. Rondina *et al.* [52] introduced a High-Pressure Resin Transfer Moulding (HP-RTM) method for producing wheels for sports cars that shows promise for mass production. The authors explored how severe environmental conditions can affect the mechanical properties of CFRP and provided numerical simulations for the injection process to reduce defects and shorten production time. Chai *et al.* [53] introduced a spoke-type wheel made of polymer reinforced with glass-fibre (GFRP), produced through injection moulding. To determine the most vulnerable areas of the wheel, they conducted finite element simulations on static bending and verified the findings through experiments. However, the investigation did not encompass the prediction of composite material fatigue life under multiaxial loads, which is still a significant challenge in current studies [54–57]. Fuji and Lin [58] noted that the stress-life curves of glass fibres reinforced polymers decrease with the presence of tension and shear forces. They tuned the Tsai-Wu [59] failure criterion using the S-N curve to predict structural damage on the composite caused by cyclic loading.

The goal of this dissertation is to provide evidence that composite materials can be effectively employed in the design of wheel rims by presenting a case study of a full composite wheel rim developed for a Ferrari sports car.

In order to provide context for the development of a composite wheel, a review of Ferrari's wheel rim designs from 2009 to the present is presented, including classifications based on weight and stiffness, and manufacturing methods such as forging and casting for aluminium alloys, as well as RTM for composite materials [60]. A comparison is made between the structural criteria outlined in the type-approval standards and the internal norms set by Ferrari S.p.A. The OEM aesthetic and functional tests carried out to ensure full safety and functionality of the new wheel are also presented. Furthermore, the Design Failure Mode and Effect Analysis (D-FMEA) result reveals the limitations of the current approval standards, developed for isotropic materials. Five functional and fatigue relevant topics are critically discussed, and the proposed composite wheel has been compared with a reference wheel made from forged aluminium.

To evaluate the fatigue life of the wheels, finite element analysis was conducted using the Dang Van [61,62] fatigue criterion for the reference wheel, and the Tsai-Wu criterion for the composite wheel.

The impacts, radial, and cornering fatigue were among the testing procedures performed on the wheels. Both wheels met the standards for homologation and Ferrari norms. The failure analysis of the wheels was conducted through non-destructive methods such as dye penetrants and Computerised Tomography (CT).

The wheel attachment is just as crucial to design as the wheel's structural strength, ensuring the vehicle's safe operation. The differences between the two wheels are pointed out, including the materials used to tighten them and the stiffness of involved parts. A method for calculating the minimum preload required for proper tightening is presented. Laboratory tests helped determine the composite rim's specific characteristics, while OEM validation tests were used to evaluate and confirm the component's effectiveness.

In recent years, the increase in the performance of Ferrari vehicles and the research for the "*fun-to-drive*" concept have led to exponential increases in accelerating and braking powers. The heat dissipated during heavy braking, especially when used on the track, was the subject of work for the development of a protective Plasma Spray application. This protection was then validated with specific laboratory tests and dynamic activities in the vehicle.

The results of numerous salt spray tests are presented, describing the fine-tuning carried out to ensure that the various materials involved in wheel fastening can provide safety and serviceability over time.

Lastly, an experimental comparison of impact resistance performance between the two materials is discussed, revealing an interesting outcome that emphasizes how the developed product is comparable to the many aluminum wheels used in every aspect.

Many of the technical data contained within this dissertation are subject to intellectual property rights. In order to proceed with publication, it was necessary to de-identify these data using specific ratios presented on a case-by-case basis.

1.2 Ferrari sports car wheel collection

Recent wheel types equipped on sports cars produced by Ferrari are shown in Table 1 [60]. The following data are detailed:

- Vehicle characteristics: model name, year and powertrain,
- Style and number of spokes,
- Material of the wheel,
- Manufacturing process,
- Divided between front and rear wheels:
    - Rim dimensions: width (w) and diameter (D),
    - Wheels mass ratio,
    - Stiffness ratio, determined through a quasi-static bending test,
    - Load ratio adopted to design.

The wheel taken as the reference is the front wheel from 488 GTB, thus the three last quantities of the table are normalized relative to their respective counterparts.

Aluminium alloys are currently the most widely employed materials in the design of automotive structural components, including wheels. Metal wheels are typically produced using low-pressure casting techniques or forged. Then, to achieve the final shape of the rim, flow-forming is applied.

In the last years, every new vehicle designed has increased steadily the performance, with an increase of vertical and lateral forces exerted on wheels. There are two main reasons for this. Firstly, the integration of new vehicle systems such as hybrid powertrains, battery packs, passive and active safety tools have caused a rise in vehicle mass. Secondly, enhancements in aerodynamic downforce have allowed higher cornering speeds. As a result, wheel design loads have steadily increased. To better manage the transmission of higher forces to the ground, it was necessary to increase the contact area between the tyre and the asphalt. Over time, this made it necessary to increase the size of the tyres with the widening of the rim (see Table 1); nevertheless, the wheel diameter has been kept constant at 20". Indeed, the size of the wheel typically relies on various factors, including the size and the type of the vehicle, the driving performance required and the desired aesthetic style.

This trend contradicts the goal of a sports vehicles manufacturer to minimize or contain its mass, thus numerical optimizations have been performed to reduce the weight of the hub section and the bolted area. This can be observed by comparing the casted wheel rim of the 458 Italia (2009) with the forged wheel of the 812 Competizione (2021).

Improving performance also means increasing top cruise speed and generating more heating during braking manoeuvres, which in turn requires effective dissipation of the heat through the wheel. Therefore, an optimization process to improve air flow and the casting of rims has been carried out on the spokes from the hub to the rim radially. Two approaches to achieve these are reducing spoke thickness or implementing specific ventilation fins between the spokes [63]. The added benefit of these fins is improved vehicle aerodynamics, demonstrated in the SF90 Stradale.

Furthermore, Table 1 highlights the number of spokes for each wheel, which has gradually increased from 5 to 10 over the years: this choice is primarily driven by aesthetic considerations, even if 10 spokes can ensure an homogeneous distribution of the operating loads.

Through optimization techniques, it became possible to create aluminium rims that can withstand loads up to 75% greater than that of the reference rim. Nevertheless, this has resulted in new wheels having an increased mass of up to 45% compared to the reference.

The optimization of the aluminium wheel reached its peak in 2015 with the development of the 10-spoke forged wheel (F12tdf), which had a technical style design that was highly optimized for the mass versus lateral stiffness ratio. This design was then replicated on the subsequent wheel (488 Pista, 2019).

The asymptote had been reached, and in order to be able to further lower the mass of the vehicle components it was necessary to study which other materials for the wheel

could be used. New materials chosen were the composite materials. These have been incorporated in wheel design, resulting in three wheel rims (488 Pista in 2019, SF90 Stradale in 2020, 812 Competizione in 2021) that are lighter than forged reference. These wheels have been manufactured using the Resin Transfer Moulding process (RTM, see *2.5 Carbon fibre technology for wheels*).

Figure 1 from [60] provides a broader perspective on how material selection and manufacturing processes impact the overall bending stiffness and normalized mass, with each bubble representing a different manufacturing process. Rear wheels have a higher bending stiffness ratio than front wheels. For the same bending stiffness value, forged aluminium wheels have a lighter design than cast parts. Composite wheels offer a promising alternative to traditional metal alloys, as they can achieve a significant weight reduction while maintaining a high bending stiffness. The green area on the graph shows that the RTM wheel design is located to the left of the forged technology, indicating a lighter weight and higher bending stiffness [60].

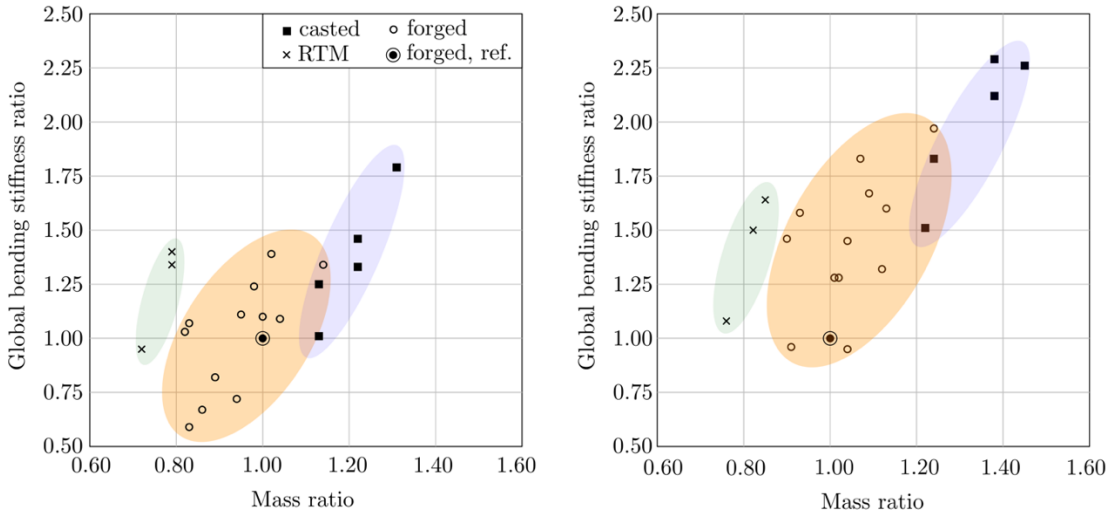

Figure 1: comparison of the overall bending stiffness ratio on the normalized mass ratio between different manufacturing processes of (a) front and (b) rear wheel rims. From [60]

							FRONT				REAR			
Model	**Year**	**Powertrain**	**Style**	**No. spokes**	**Material**	**Technology**	**Dimensions [W x D]**	**Mass ratio**	**Stiffness ratio**	**Design load ratio**	**Dimensions [W x D]**	**Mass ratio**	**Stiffness ratio**	**Design load ratio**
458 Italia	2009	Rear-mid ICE		5	AlMg1SiCu 6061-T6	Forged + Flow-forming	8,5J x 20"	0.94	0.72	0.91	10,5J x 20"	1.04	0.95	1.20
458 Italia	2009	Rear-mid ICE		5	AlSi7Mg0.3 A356-T6	LPD Casting + Flow-forming	8,5J x 20"	1.13	1.01	0.98	10,5J x 20"	1.22	1.51	1.29
F12	2012	Front ICE		Multi spokes	AlSi1MgMn 6082-T6	Forged + Flow-forming	9,5J x 20"	0.89	0.82	1.09	11,5J x 20"	1.01	1.28	1.47
F12	2012	Front ICE		5	AlSi7Mg0.3 A356-T6	LPD Casting + Flow-forming	9,5J x 20"	1.22	1.33	1.10	11,5J x 20"	1.38	2.12	1.47
458 Speciale	2013	Rear-mid ICE		5	AlSi1MgMn 6082-T6	Forged + Flow-forming	9J x 0"	0.83	0.59	0.90	11J x 20"	0.91	0.96	1.23
458 Speciale A	2014	Rear-mid ICE		5	AlSi1MgMn 6082-T6	Forged + Flow-forming	9J x 20"	0.86	0.67	0.90	11J x 20"	0.96	1.11	1.23
488 GTB	2015	Rear-mid ICE		5	AlSi1MgMn 6082-T6	Forged + Flow-forming	**9J x 20"**	**1.00**	**1.00**	**1.00**	11J x 20"	1.02	1.28	1.26
488 GTB	2015	Rear-mid ICE		5	AlSi7Mg0.3 A356-T6	LPD Casting + Flow-forming	9J x 20"	1.13	1.25	1.01	11J x 20"	1.24	1.83	1.31
F12tdf	2015	Front ICE		10	AlMg1SiCu 6061-T6	Forged + Flow-forming	10J x 20"	0.82	1.03	1.22	11,5J x 20"	0.90	1.46	1.54
812 Superfast	2017	Front ICE		Multi spokes	AlMg1SiCu 6061-T6	Forged + Flow-forming	10J x 20"	0.95	1.11	1.25	11,5J x 20"	1.04	1.45	1.58
812 Superfast	2017	Front ICE		5	AlSi7Mg0.3 A356-T6	LPD Casting + Flow-forming	10J x 20"	1.22	1.46	1.25	11,5J x 20"	1.38	2.29	1.58
488 Pista	2018	Rear-mid ICE		10	AlMg1SiCu 6061-T6	Forged + Flow-forming	9J x 20"	0.83	1.07	1.04	11J x 20"	0.93	1.58	1.34
488 Pista	2018	Rear-mid ICE		10	CFRP	Preformed hand layup + RTM	9J x 20"	0.72	0.95	1.10	11J x 20"	0.76	1.08	1.46
488 Pista Spider	2019	Rear-mid ICE		Multi spokes	AlSi1MgMn 6082-T6	Forged + Flow-forming	9J x 20"	0.98	1.24	1.03	11J x 20"	1.07	1.83	1.38
F8 Tributo	2019	Rear-mid ICE		Multi spokes	AlSi1MgMn 6082-T6	Forged + Flow-forming	9J x 20"	1.04	1.09	1.04	11J x 20"	1.12	1.32	1.34

812 GTS	2020	Front ICE		10	AlMg1SiCu 6061-T6	Forged + Flow-forming	10J x 20"	1.02	1.39	1.30	11,5J x 20"	1.09	1.67	1.62
SF90 Stradale	2020	PHEV*		5	AlSi1MgMn 6082-T6	Forged + Flow-forming	9,5J x 20"	1.14	1.34	1.25	11,5J x 20"	1.24	1.97	1.55
SF90 Stradale	2020	PHEV*		5	AlSi7Mg0.3 A356-T6	LPD Casting + Flow-forming	9,5J x 20"	1.31	1.79	1.25	11,5J x 20"	1.45	2.26	1.55
SF90 Stradale	2020	PHEV*		10	CFRP	Preformed hand layup + RTM	9,5J x 20"	0.79	1.34	1.33	11,5J x 20"	0.85	1.64	1.56
812 Competizione	2021	Front ICE		10	AlSi1MgMn 6082-T6	Rotary forging + Flow-forming	10J x 20"	1.00	1.10	1.29	11,5J x 20"	1.13	1.60	1.76
812 Competizione	2021	Front ICE		10	CFRP	Preformed hand layup + RTM	10J x 20"	0.79	1.40	1.29	11,5J x 20"	0.82	1.49	1.76

Table 1: rundown of Ferrari sports car wheel rims

Chapter 2
THE WHEEL AND ITS VALIDATION PROCESS

2.1 The anatomy of a wheel

Although *wheel* and *rim* are frequently used as interchangeably, they have distinct technical meanings. The term *rim* specifically denotes the outer shell or *barrel* onto which the tyre is mounted, while the *wheel* encompasses both the rim and its connection to the hub. Additionally, the term *wheel* can also denote the complete assembly of the tyre mounted the rim.

The tyre is mounted radially on the rim using two *beads* and it contacts the rim's edges by applying an axial force on two *flanges*. The shape of the rim's flanges is classified based on their shape, with the J-horn being the prevailing shape for passenger cars.

Wheels can be categorized as either disk-type wheels or spoke-type wheels, depending on whether the rim is connected to the hub housing via a thin shell or a series of spokes, respectively.

Figure 2 provides a close-up of a spoke-type wheel rim, showcasing the geometry of the hub housing and the inflation valve seat. The distance between the inner flanges is known as the *rim width* (*w*), while the *nominal diameter* (*D*) refers to the diameter of the beads. Additionally, the *offset* (*ET*) measures the distance between the centreline of the rim and the hub mounting surface.

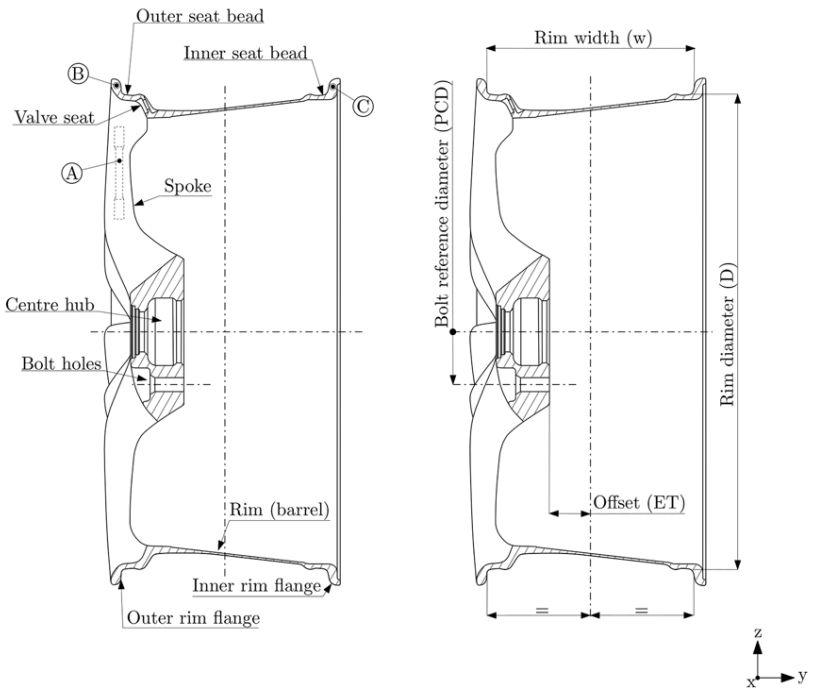

Figure 2: wheel rim nomenclature

Figure 2 illustrates the potential regions for sample extraction to evaluate the material's fatigue life, including the spoke region (marked as A), the rim flange areas (labelled as B and C) and the centre hub zone [13,28,30].

2.2 Wheel development process

The wheel development process has become standardized in recent years and is a *co-design* development between the vehicle manufacturer and the supplier of the component. Co-design means collaborative design. In the wheel development, unlikely any other co-design development, the mutual sharing of information can be difficult due to the reluctance of one of the two partners to exchange information for fear of leakage to competitors [64], even if, as reported by Red *et al.* [65], collaborative design aims to speed up product development, lower costs and meet high quality standards set by the OEM while reducing environmental impact.

From the OEM point of view, the wheel development can be summarized in four macro-phases:

1. Development project specifications: in this phase, the vehicle manufacturer plays the lead role by setting the specifications of the component (technical, aesthetic, quality, etc.). The supplier is responsible for reviewing these specifications, determining the technical and economic feasibility, and creating a development plan. The phase ends with the selection of the chosen supplier,
2. Component design: once the supplier is selected, he begins designing the wheel considering the specifications defined by the OEM. During this phase, both parties work closely to overcome any technical, stylistic, or technological challenges. The second phase ends with the virtual approval of the components and the tooling kick-off,
3. Component industrialization: in this phase the supplier builds the equipment and moulds suitable for the final production of the component. These tools are initially defined as "*prototype*", but they are already the definitive tools for mass production. They are thus defined until they are approved. This process is unique to wheels in the automotive industry, as it is difficult to produce wheels using temporary tools that are only suitable for a limited number of prototypes,
4. Component validation: after having built the necessary tooling and the first prototypes aimed at fine-tuning the production process parameters, the supplier starts producing prototypes for the wheel validation. This can be divided into two sub-phases:
    a. Wheel validation and homologation: this is the part of the experimental tests carried out by the supplier independently, under vehicle manufacturer's requests,
    b. In-vehicle testing: this is the part of the tests aimed at homologating the wheel for road use in complete safety, under manufacturer's responsibility with possible support from the supplier.

The development project ends when the validation and testing plan are completed and the wheel is qualified for road use. When this "gate" is passed, the moulds change their definition from "*prototype moulds*" to "*final mould*" for production.

So far this is what happens when a new aluminum, forged or casted, wheel is developed, because the material is already well known.

In the development of a new material or technology wheel, as for a carbon fiber reinforced polymer wheel, the process becomes more complex and onerous: to the above, a preliminary phase must be added. During this additional *preliminary and preparatory* phase, in parallel with activities such as the benchmark of the market and the research for the best supplier, a *Design Failure Mode and Effect Analysis* (D-FMEA) of the component needs to be done. The result of the D-FMEA has been integrated inside the technical datasheet containing all the specifications.

Some of the specifications needed to develop a wheel are:

- Wheel geometry and dimensions: diameter and width, offset,
- Tyre fitted,
- Design loads,
- Style requirements,
- Vehicle constrains: brake caliper envelope, suspensions envelope, vehicle body homologation surfaces,
- Fastening method and characteristics,
- Critical and security geometrical characteristics and control plan
- Limit temperatures: for road and track use and storage,
- Limit environmental conditions,
- Type and list of standards and homologation requirements,
- Stiffness target,
- Vehicle milestone for component development.

The resulting developed component must comply with all these specifications.

2.3 Standard tests for wheel approval and requirements

Today's road vehicles are requested to keep a high comfort and safe handling over an increasing mileage. Moreover, high performance vehicles require an accurate dynamic performance with increasing speed. Therefore, the wheel's fatigue endurance must be handled with caution to avoid endangering the vehicle occupants during use. The subsequent sections will outline the five required standard tests for wheel approval. The first two tests pertain to the impact resistance of a wheel rim, while the third to fifth tests pertain to the wheel's fatigue resistance.

2.3.1 Impact tests

There are two standard tests that assess the wheel's ability to withstand lateral and radial impacts, which may occur when the wheel strikes an obstacle like a bump, pothole, or curb. In both tests, the tyre is mounted onto the rim.

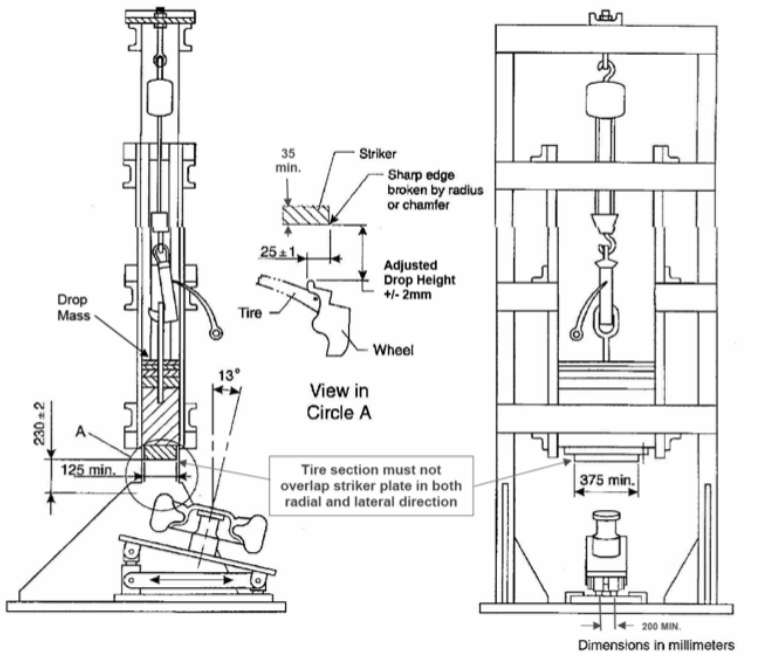

Figure 3: test rig layout for lateral impact. From [66]

In the lateral impact test [66] (see Figure 3) a specially designed impactor, with a unique size and shape, is dropped onto the side of the wheel from a height of 230mm. The impact occurs close to the outer rim flange, at 13° angle from the wheel rotation axis. The mass of the impactor, *M*, is measured in *kilograms* by the formula:

$$M = 0.6 * W + 180 \quad (1)$$

where W is the gross vehicle weight on the front or rear loaded axle. The standard operating pressure is used to inflate both front and rear wheels. The test is considered successful if there are no visible cracks that penetrate the entire section of the wheel, there is no detachment between the wheel centre and spokes or rim, and if the tyre pressure remains unchanged one minute after the test.

In the radial impact test [67], V-shaped striker impacts the wheel radially [68,69]. The impactor dimensions are reported in Figure 4. The tyre is inflated to the minimum pressure recommended by the manufacturer, and the impact energy, *E*, is calculated using the formula:

$$E = Kq \quad (2)$$

where the amplification factor is represented by *K*, and the wheel load is expressed in *kilograms* as *q*. Despite being dimensionally inconsistent, the above equation is adopted to correlate the fall height of the impactor to the impact energy, as well as the impact velocity [68,69]. The wheel undergoes two impacts, with the first impact assigned a *K* value of 1.15, referred to as Level 1, and the second impact assigned a *K* value of 4.3, referred to as Level 2. The test is considered successful at the first stage if wheel deflection at the inner rim horn is below a specific threshold. At the second stage, if cracks in the deep bed area do not exceed 90° (25%) of the periphery [60].

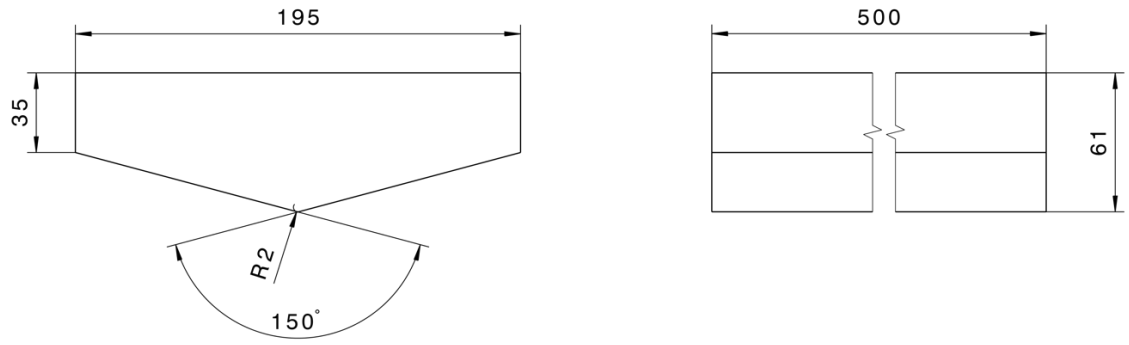

Figure 4: dimensions of the AK-LH08 V-striker impactor

2.3.2 Cornering Fatigue test

Cornering fatigue test is a test that subjects the wheel to cornering forces by inducing a rotating bending moment.

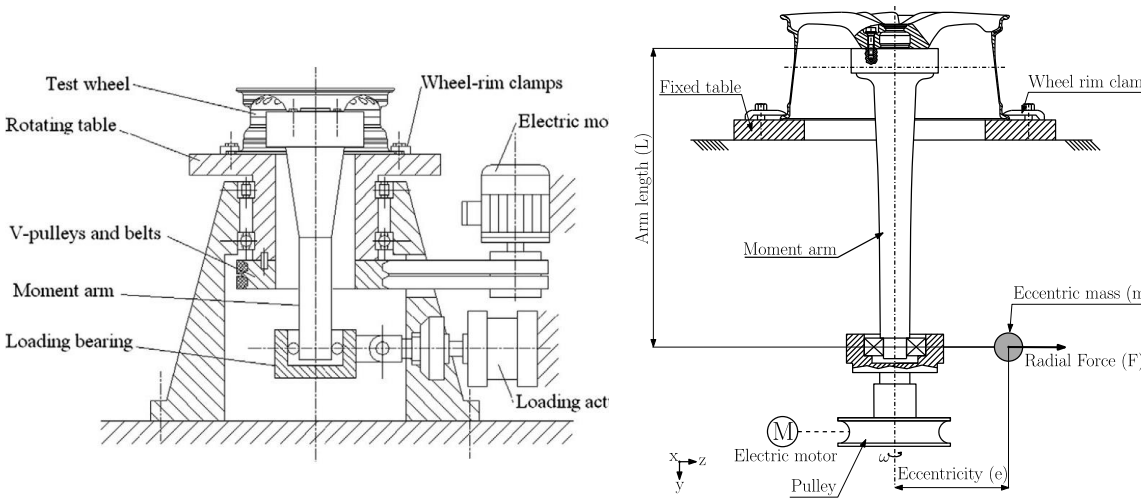

(a) *(b)*

Figure 5: cornering fatigue test rig layouts: a) with rotating table [15,19,47] *and b) with an eccentric mass* [13,18,23]. *From* [60]

The wheel's inner rim flange is clamped to a table while an arm is fastened to the hub, a force F is applied to the arm at a minimum distance of 762mm (30in) from the hub, generating a prescribed bending moment on the hub. Two different layouts are employed to ensure that the bending moment rotates relative to the wheel. In the first layout (shown in Figure 5a), the plate rotates while the force is provided by a fixed actuator. In the second system (shown in Figure 5b), the wheel is fixed, and the force F is the centrifugal force generated by an eccentric mass rotating around the arm's free end.

The maximum bending moment at the wheel hub is calculated using the following formula:

$$M = K\,W g \left(\frac{\mu D}{2} + ET\right) \tag{3}$$

where W is the gross vehicle weight on the loaded axle, μ is the static friction coefficient, D is the wheel diameter and ET is the wheel offset, as shown in Figure 2. The amplification factor K is adopted to accelerate the fatigue test, which would otherwise require more than 10^7 cycles to simulate the expected life of a wheel [18]. The standard procedures specify the values of K, and these values are supported by Kinstler's justification [4]. The applied force (or the eccentrical mass) is tuned to generates the requested bending moment M on the hub. In SAE J328 [5] the test is carried out at this specific reference bending moment M up to 50.000 cycles. Other testing regulations, such as UN/ECE R124 [9], require the test to be conducted with two distinct levels of bending moment. In the first level, the wheel is tested at the 50% of the maximum bending moment M, while in the second one the load is brought up to the 75% of bending moment M. To fully comply with the standard, at least two wheels, one front and one rear, must be tested at each level.

According to SAE J328 [5], the test is passed if no fatigue cracks that penetrate through the section are observed before the minimum required number of cycles, and if the arm's deflection does not exceed 20% of the initial value. In contrast, more stringent standards such as [6–8] require the absence of cracks detected through non-destructive method like dye penetrants, and reaching a minimum cycle count, which varies with the wheel's material and vehicle category. Additionally, the test is deemed successful if the arm's deflection is below a specific threshold and the tightening torque of the bolts remains above 70% of the initially torque [60]. The OEM regulation demands two load stages at different K values: the first for 250,000 cycles at K value 2 and the second for 1,000,000 rotary bending moment cycles at K value 1.5.

2.3.3 Radial Fatigue test

Radial fatigue test mimics the straight driving conditions of the wheel, with the purpose to assess the structural integrity and the durability under repeated radial loads. In fact, during the test, a force is applied to the wheel in a radial direction, perpendicular to the wheel's axis of rotation.

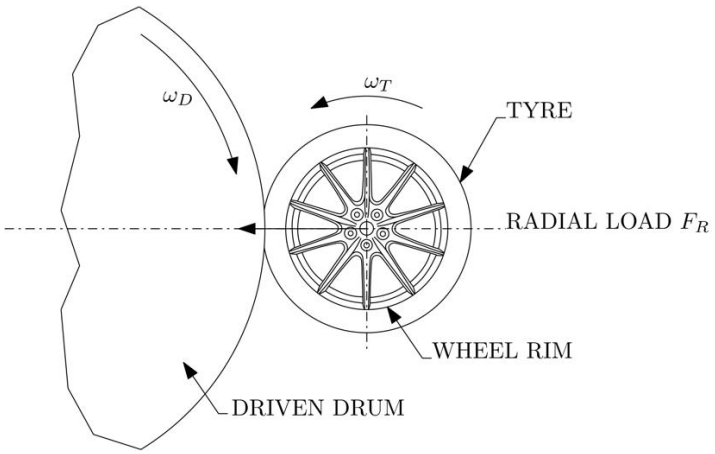

Figure 6: radial fatigue test layout. From [60]. *See also* [4].

The force is applied by a rigid-driven drum, which is kept in contact with the tyre by a hydraulic actuator, as in Figure 6. The test fixture used is designed to replicate the vehicle hub so the wheel is fastened to it using its bolts.

To accelerate the fatigue test and obtain a safe fatigue design of the rim, the tyre pressure is increased to an higher pressure (usually 4.5 bar) than the normal driving conditions. In addition, the hydraulic actuator imposes a radial load (FR) that is multiplied by a factor K higher than 1. The radial load of testing is calculated using the following formula:

$$FR = K W g \tag{4}$$

where K varies for front and rear wheels. According to SAE J328 [5], the test is considered successful if no fatigue cracks that penetrate the section are observed through visual inspection before 600,000 cycles, as in cornering fatigue case. However, other standards require that cracks should not be detected using dye penetrants [9]. The OEM regulation considers the same K values for all wheels, and the test lasts for up to 1,000,000 cycles.

2.3.4 Biaxial Fatigue test

The biaxial fatigue test is performed to simulate the actual driving conditions of the wheel and to determine its fatigue life under such conditions [11,12,17]. The test is conducted by mounting the wheel onto a test rig and is put in rotation against a driven drum, while two hydraulic actuators apply loads in both radial and lateral directions to the wheel [30].

The biaxial loads are obtained from the load patterns experienced by the wheels in different scenarios, including normal driving on public roads or extreme conditions on motorsport tracks like Nürburgring or Hockenheimring [30]. Wan *et al.* [70] and by Santiciolli *et al.* [71] have provided a review of the testing procedures and the numerical method used to correlate the results [60].

2.3.5 New structural wheel testing standards and requirements for Matrix Material and Fiber Reinforcement

The advent on the market of wheels for cars produced in materials other than known alloys has prompted the scientific community and the approval bodies to develop new standards for these wheels. Thus, SAE released the SAE J3204:2020 standard in 2020, to regulate the radial and lateral fatigue test for composite wheel rims for the aftermarket [50]. This standard introduces a parameter called SRFF, which is a fatigue reduction factor imposed by the wheel manufacturer to account for matrix performance degradation during ageing tests.

2.3.6 Other validation requirements

Less important from a structural point of view but equally important from an aesthetic and perceived quality point of view are those tests that evaluate the environmental resistance to ageing, both due to daily use and during long stops in the parking lot. The aim of these tests is to ensure that the component maintains his structural and aesthetical qualities for the entire life of the vehicle.

There are international standards for this type of tests. These can be divided into two main groups: functional paint requirements and ageing requirements. Functional paint tests are: film thickness (ISO 2808 [72]), cross-cut test (ISO 2409 [73]), stone impact (SAE J400 [74] and ISO 20567-1 [75]), resistance to different liquids like gasoline, mineral oils (as brake fluid), humidity, etc… (ISO 6270 [76]) and chemical aggression (SAE J2792 [77]). Ageing paint tests are: corrosion in neutral salt spray (ISO 14993 [78]), filiform corrosion (SAE J2635 [79]), accelerated ageing in atmospheric agents (SAE J2527 [80]) and UV resistance (SAE J2633 [81]).

Generally, each OEM develops its own aesthetic and environmental standards. As for the structural tests, it is based on standards but modified according to the OEM's prior experience and history. In the Ferrari case, these tests are extremely tough because, especially in terms of time, Ferrari vehicles must be tested literally "*for life*".

2.4 Vehicle manufacturer tests and requirements

It is not enough just to validate the wheel as a component alone. The whole car must be safe. The supplier's validation tests ensure the safety of the wheel, but the responsibility for proper wheel attachment and function in the car lies with the vehicle manufacturer. And here is that one of the most important aspects in the design of the wheel is the study of its fastening to the vehicle. Objectives of the fastening system are to ensure the safety of the car and to allow easy assistance during tyre changes and maintenance (Figure 7). To guarantee this, Ferrari uses two validation standards: a laboratory one and a vehicle one. The goal of the laboratory test is to tighten multiple times the same wheel bolt and check the obtained preload in order to guarantee its repeatability over the years. The test is like the SAE J2316 standard, with the major difference being the lower number of times that the single wheel bolt is tightened [82]. Thanks to this test, the repeatability of the wheel bolt preload, which must always be greater than a minimum value, the stability of frictions and the clamping of the components are checked in laboratory. Obviously, the test in laboratory is performed without generating external loads on wheel bolts. Therefore, it is necessary to rely on a specific OEM standard for wheel bolts loosening test. This consists in checking the preload on each single wheel bolt installed in the vehicle before, during and after the mission of the vehicle. The mission consists of two distinct activities: first a 200km of mountain route around Maranello are covered, then a series of laps of the Fiorano track are carried out up to a level of tyre wear that would force the customer to change it. Bolt tension is checked before beginning, between the two mission and at the end. The test is passed if, at the end of the vehicle mission, the average tightening preload of all wheel bolts is above the minimum value required.

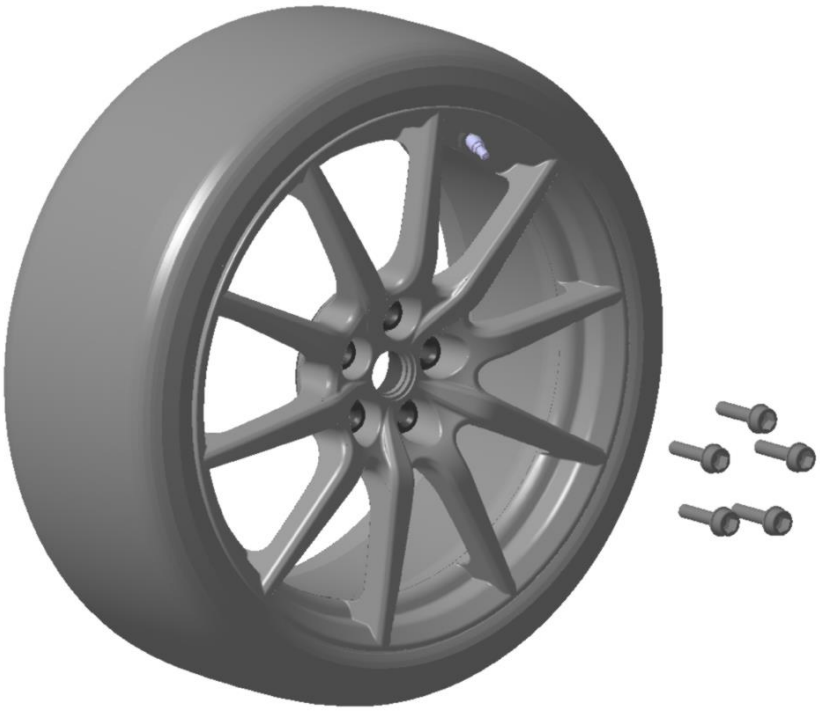

Figure 7: wheel assembly

2.5 Carbon fibre technology for wheels

The composite materials, intended as Fibre Reinforced Polymer (*FRP*), made their entrance in 1940s. The first production technology was wet Hand Lay-Up (*HLU*) of fibre glass (*E glass*) with polyester as matrix, used to make boats, pipes and other products.

In 1960s, composite materials made by carbon fibre and epoxy resin as matrix have made their appearance. This binomial with better performance is called advance composites. Firstly, advanced composites were applied only by hand lay-up [83]. About ten years later, Citroen developed and tried to produce the first carbon fibre reinforced polymer wheel, but to no avail as production was shortly halted due to technical problems [3].

Today, there are multiple ways to produce advance composites (see Figure 8), but a wheel is feasible only by two processes with lots of hand lay-up procedures: vacuum bagging cured in autoclave or Resin Transfer Moulding (RTM).

The vacuum bagging cured in autoclave process involves the use of a pressurized oven to cure the resin and consolidate the composite structure. This process is known for producing high-quality, consistent, and high-performance composites. However, it is also a more expensive and time-consuming process, due to the need for specialized equipment and trained personnel.

The RTM process, on the other hand, involves the injection of resin into a mould, typically under pressure. The RTM process is a more flexible and cost-effective method, allowing for more complex geometries and quicker production times compared to the autoclave process. However, the quality and performance of the composite produced by RTM can

be more variable and dependent on the quality of the mould and the consistency of the resin injection process [85].

In conclusion, the main difference between the vacuum bagging cured in autoclave and RTM processes for CFRP production lies in the trade-off between quality, cost, and production time. Precisely these advantages are what have allowed the RTM process to emerge in recent years, and as highlighted by Rondina *et al.*[52], a potential production process for high geometrical complexity components as wheel rims.

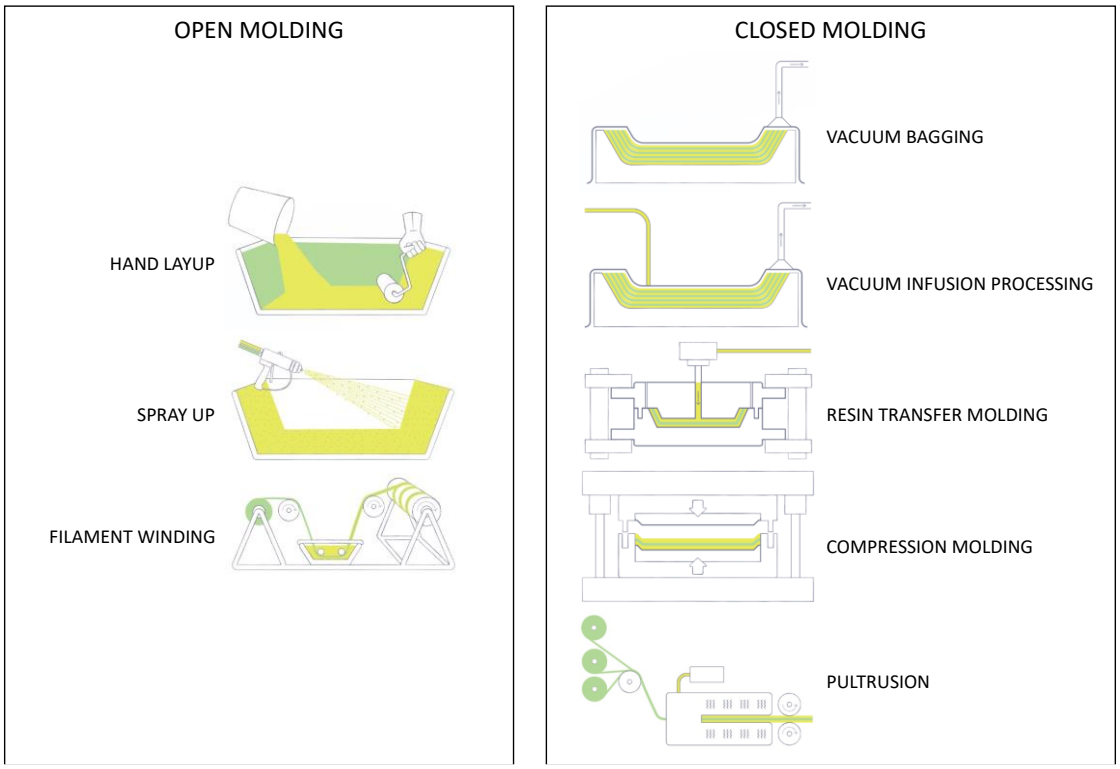

Figure 8: list of composite materials production processes. Images from [84]

2.6 Carbon wheel concept

Ferrari presented its first composite wheel rim at the Geneve Motorshow in 2018, for the 488 Pista as an optional product.

The wheel comprises stacked unidirectional and fabric composite plies, along with a polymeric foam and an inner preform of randomly distributed milled fibres. The dry assembly is subsequently placed in a mould, and Resin Transfer Moulding is employed, with the resin injected at a prescribed pressure, and a specific temperature cycle ensuring the matrix polymerization occurs correctly.

Figure 9a and Figure 9b provide an overall views of the composite wheel, while Figure 9c and Figure 9d offer a more detailed view of the hub and the bolted zones.

(a) *(b)*

(c) *(d)*

Figure 9: composite wheel concept of 488 Pista: overall and detailed views from the front view (a, c) and back view (b, d). From [60]

In accordance with SAE J3204 [50], the wheel presented in this work is considered as a *composite wheel*; however, metal alloys are employed up to 6% of the wheel's mass to connect the wheel to the vehicle. To prevent excessive wear of the composite, an aluminium backplate is positioned at the contact interface between the wheel and the hub [23,44]. The backplate also aids the centering of the wheel, avoiding any potential imbalance. To maintain the initial tightening of the bolts, additional metal inserts are positioned on the internal surface of the bolted holes [86], as shown in Figure 9c-d. Finally, circlips are utilized to keep inserts in position when the wheel is not mounted on the vehicle, as shown in Figure 10.

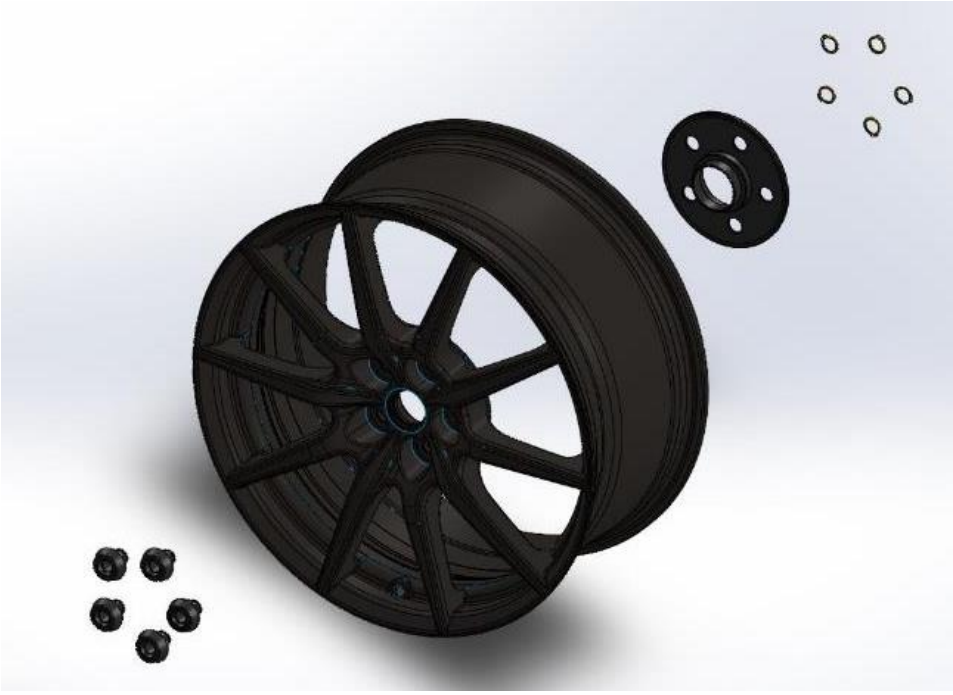

Figure 10: composite wheel assembly with inserts, backplate and circlips

The mass distribution of the materials used in the wheel is reported in Figure 11. UniDirectional (UD) carbon fibres and epoxy resin account for 54% and 25% of the total wheel mass, respectively. The volume fraction of the UD fibres varies from 55% to 60%. PolyAcryloNitrile (PAN) fibres are used to produce a plain weave carbon fibre fabric, which is applied to the outer surface of the wheel for aesthetic reasons. This fabric accounts for 4% of the overall wheel mass.

The polymeric foam and milled carbon fibres incorporated with epoxy resin serve as the internal preform in sandwich panel construction and facilitate the manufacturing process. Its primary function is to maintain the structural UD laminates at a distance from each other, thereby increasing the overall stiffness and inertia section of the spokes.

Lastly, the Non-Structural Mass (NSM) includes all the materials used in the wheel rim that do not affect its structural performance considerably, including the inner ceramic thermal coating and the glossy paint.

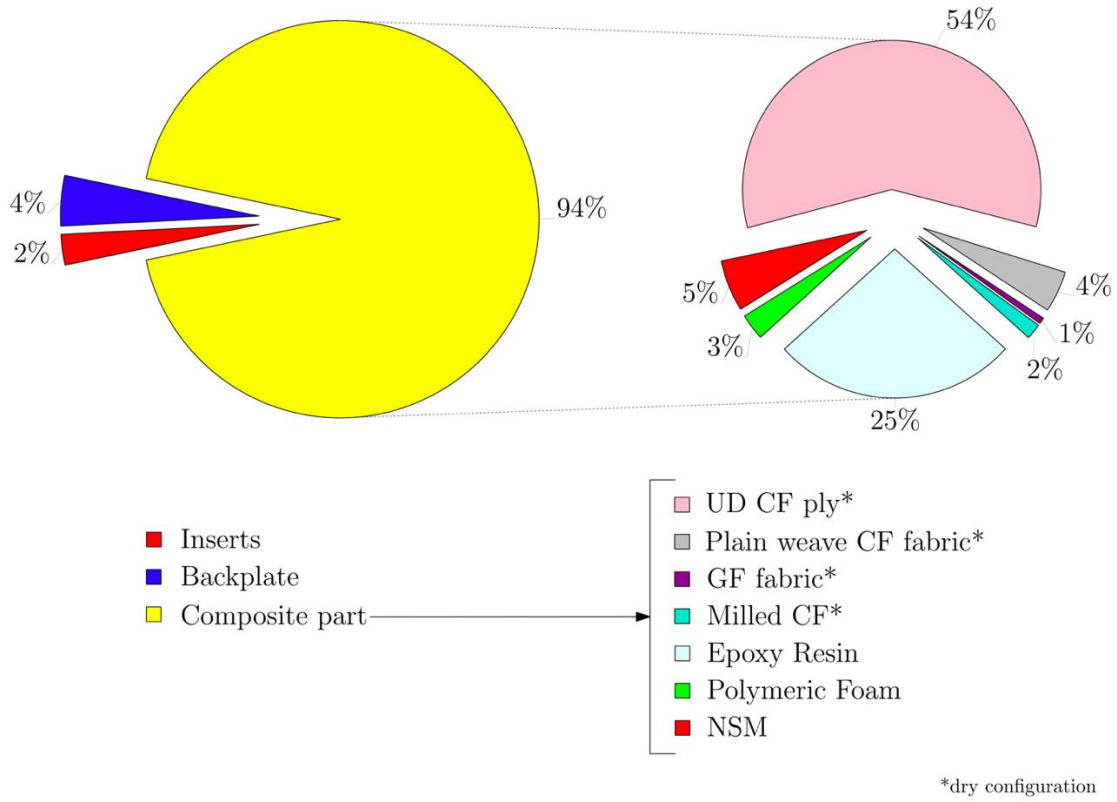

Figure 11: mass distribution of the composite front wheel on the 488 Pista. From [60]

However, the first wheel proposed by the supplier was not as described above. Table 2 presents the initial proposal and the final solution implemented in production. Subsequent sections will discuss and provide rationale for the modifications listed below.

	Proposal from supplier	**Homologated for road/track use**
Rim technology	RTM	RTM
	epoxy resin with Tg > 200°C	epoxy resin with Tg > 200°C
Final paint	Transparent glossy	Transparent glossy
	thickness 40-100 μm	thickness 80-120 μm
Thermal protection	Multi-coating plasma spray Al_2O_3-YSZ-Al_2O_3	Multi-coating plasma spray Al_2O_3-YSZ-Al_2O_3
	thickness 300-500 μm	thickness 300-500 μm
		Double layer of GFRP below TBC
Inserts	Al7075-T7351	Al7075-T7351
	black hard anodization thickness 30-50 μm	black hard anodization std. thickness min 70 μm

Anti-rotation pin	Steel AISI 316	GFRP
Circlip for inserts	Steel AISI 1095 zinc-plated thickness 30 μm	Steel AISI 1095 zinc-plated thickness 30 μm
Backplate	Al6061-T6 hard anodization - thickness 30-50micron	Al6061-T6 hard anodization - thickness 30-50micron

Table 2: comparison between first proposal from the supplier and homologated wheel for 488 Pista

After the 488 Pista composite wheel, two additional composite wheels were developed, as shown in Table 1. These wheels have slightly different spoke shapes and preform compositions, resulting in increased stiffness. Additionally, the newer composite wheels have wider dimensions that the previous ones, with the front rim increasing from 9J to 10J and the rear one increasing from 11J to 11.5J.

2.7 Failure Mode and Effect Analysis application

The Failure Mode and Effect Analysis (FMEA) is a qualitative method that allows to analyze potential critical issues and potential risks starting from a failure mode and studying the causes and its effects perceivable from the customer [87]. The aim of the FMEA is to mitigate them through the introduction of precautionary measures and counteractions in design (D-FMEA) and process (P-FEMA). The FMEA method was introduced in the automotive industry based on the results of the Apollo airspace program in 1970s [88] from SAE with standard ARP926, that then becomes known as SAE J1739 [89]. It is not surprising that, after automotive application, the methodology was taken as reference methodology for risk management in international standards as ISO 9001:2015 *Quality management systems — Requirements* [90] for a wider spectrum of commercial sector and as IATF 16949:2016 *Quality management system requirements for automotive production and relevant service parts organizations* [91] specifically for automotive sector [87].

The FMEA scope is to assist the user to recognize and identify the potential failures of the product, understand causes and effect of those failures, build a ranking chart of the potential failures thanks to the *Risk Priority Number (RPN)* and then to mitigate it imposing new or additional requirements and tests that will affect the final product changing it and, consequently, improving it.

The Risk Priority Number (RPN) is defined as:

$$RPN = (S) * (O) * (D) \tag{5}$$

where the parameter S is the severity and O is the occurrence of the failure, while D is detection.

In other words, RPN is the product of "*how serious can be the failure*" per "*how many times could it happen*" per "*how easy is to detect it*".

This methodology has been applied to this new development in a very early development phase.

Thanks to the brainstorming activity, numerous potential critical issues emerged due to the differences between a component made with an isotropic material which does not considerably suffer elevated temperature such as aluminum and one made with orthotropic material such as composite materials with epoxy resin system. Specifically, the strengths and weaknesses of the presence of the fiber, on the one hand, and of the resin, on the other, represented a further source of challenge.

In Table 3 the result of the FMEA can be found, with the RPN being drastically lowered after the validation tests. The color of the cells is linked to the RPN value and is arbitrary.

The five bigger challenges of this development were:

1) Structural integrity of the wheel in fatigue validation tests,
2) Structural integrity and safety in detecting impact damages,
3) Thermal behavior when driving in tracks or public roads,
4) Fastening of the wheel to the vehicle hub,
5) Corrosion and environmental effects.

These five topics will be covered in the following chapters.

	POTENTIAL FAILURE MODE AND EFFECTS ANALYSIS - RISK MATRIX												Result			
	Item (Component / Interface)	Elementary Function	Potential Failure Mode	Potential Effect(s) of Failure	SEV	Potential Cause(s) of Failure	OCC	Current Design Controls Prevention	Current Design Controls Detection	DET	RPN	Recommended Action / Action Taken	SEV	OCC	DET	RPN
1	Carbon fibre wheel	Thermal resistance	Resin performance degradation	Rim breakage / Loss of vehicle grip	8	Thermal damage to the wheel	10	1) Analyze DFMEA and product sheet with the supplier	1) Production: 100% check of resin Tg 2) Test bench: Fatigue validation tests (radial bending moment, biaxial, radial fatigue) 3) Vehicle: wheel bolts tightening test	9	720	Introduce specific functional vehicle test to check wheel rim temperature	7	1	6	42
2	Carbon fibre wheel	Structural resistance	Wheel crack / delamination	Rim breakage / Loss of vehicle grip	8	Structural damage to the wheel	10	1) Analyze DFMEA and product sheet with the supplier 2) FEA simulations	1) Production: 100% CT-scan of the wheel 2) Test bench: Fatigue validation tests (radial bending moment, biaxial, radial fatigue) 3) Vehicle: wheel bolts tightening test	5	400	Introduce vehicle durability with mountain roads, tracks and special pavements	7	2	2	28
3	Wheel / Inserts / Backplate	Ensure correct fastening of the wheel	Fastening of the wheel not guarantee	Rim breakage / Loss of vehicle grip	8	Wheel bolts preload not sufficient	10	1) Design: Analyze system dimensions and tolerances 2) Design: Wheel bolts preload calculation	1) Test bench: wheel bolts tightening test on bench 2) Vehicle: wheel bolts tightening test	3	240	1) Experimental activity to setup the carbon fibre volume fraction 2) Introduce a wheel bolts tightening test with thermal cycles in laboratory	8	2	3	48
4	Carbon fibre wheel	Resistance to abrasion and impact generated by the sidewalk and road surface disconnections	Wheel crack / delamination	Rim breakage / Loss of vehicle grip Tire deflates	8	Brittle characteristics of carbon fibre structure	8	Design: Analyze DFMEA and product sheet with the supplier	Test bench: impact validation tests (radial and lateral impacts)	3	192	1) Experimental vehicle test with specific "crossbars" 2) in case of huge impact damage, tire will defleat and TPMS warning lamp will turn on 3) maintenance booklet: include clear indications on the replacement of the wheel rim in the event of damage to the fiber during the vehicle use	7	1	2	14
5	Carbon fibre wheel	Resistance to corrosion / aging	Wheel crack / delamination	Rim breakage / Loss of vehicle grip	8	Corrosion of the metal parts and aging of the matrix	7	1) Design: Analyze DFMEA and product sheet with the supplier 2) Check galvanic corrosion from periodic table	1) Production: 100% check of resin Tg 2) Laboratory: NSS test	3	168	1) In the laboratory test, add also hub, upright, wheel bolts to build relative galvanic corrosion chain 2) Cornering fatigue test on a wheel tested in NSS	8	2	3	48

Table 3: major D-FMEA topics

Chapter 3
FATIGUE TESTS

The aspect of wheel fatigue resistance is unquestionably the most critical one. While an impact is usually noticeable by the driver in the passenger compartment, failure due to fatigue can occur without any warning signs. This can result in the loss of the vehicle.

The significance of this aspect was highlighted in the preventive FMEA activity, which assigned it an initial RPN of 400, second only to the thermal resistance aspect of the CFRP epoxy matrix.

Section *2.3 Standard tests for wheel approval and requirements* discusses the two fatigue standard tests: cornering fatigue and radial fatigue. Subsequently, this chapter presents the computational and experimental activities performed during the development, along with the results and commentary.

As previously mentioned, the bench tests aim to replicate the road loads experienced by the rim through the tyre.

Radial fatigue test does a good job in this regard, but it has two limitations. Firstly, it does not consider any camber angle that may occur during normal driving conditions, as the wheel and drum rotate along parallel axes. Secondly, the smooth surface of the drum used in this test does not replicate the natural asperities of the road.

On the other hand, the cornering fatigue test rig applies the load on the rim differently than the lateral load from the tyre because the test rig does not have a tyre. The wheel is clamped onto the test bench by the inner bead, but as noted by Grubisic *et al.* [12], this method of clamping may not accurately replicate load transfer during cornering manoeuvres on a vehicle. In 2021, Anandraj *et al.* [44] developed an innovative setup which also includes part of the suspension system to simulate dynamic loading condition.

3.1 FEA simulations

FE methods were utilized to investigate the stress field and the durability of the wheel rim. The resulting models were used to develop practical design guidelines, and their accuracy was compared against experimental data. The subsequent sections detail the model setup and the expected numerical outcomes for cornering and radial fatigue test simulations. The study employed the ABAQUS commercial software.

(a) *(b)*

Figure 12: front wheel-tyre assembly of: (a) reference forged aluminium wheel; (b) composite wheel. From [60]

To analyse the reference aluminium wheel rim (Figure 12a), a second-order tetrahedral elements (C3D10) were used for discretization, with the mesh size varying gradually from 5 mm to 1 mm. The smallest element size is located at the fillet radius between the spokes and the central hub housing, where previous studies have shown a high failure probability [13–16]. Additionally, a thin layer of quadratic, 6-noded shell elements (STRI65, thickness = 0.01 mm) was applied over the solid mesh to measure stresses and strains for fatigue evaluation purpose.

The preform of the composite wheel rim (Figure 12b) was discretized using first-order tetrahedral elements (C3D4), with the same mesh size and refinement as the aluminium wheel rim. The CFRP laminates were modelled with 8-noded hexahedral continuum shell elements (SC8R), featuring reduced integration, hourglass control, and finite membrane strain. The nodes of the shell elements coincide with the preform nodes. Meanwhile, 8-noded hexahedral elements (C3D8R) were utilized to model the backplate and the metal inserts at the bolted areas, assuming a perfect adherence to the composite layers.

The aluminium and the composite wheel rim used approximately 700.000 and 500.000 elements, respectively. Both materials were considered to be linearly elastic, with the aluminium alloy being isotropic and the composite plies following an orthotropic law. To determine the equivalent properties of the laminates, classical lamination theory was applied.

Table 4 compiles the mechanical characteristics utilized for both the aluminium alloy and the components of the composite wheel. The mechanical properties of the plain weave fabric and unidirectional ply were obtained through specialized experimental testing [92]. Meanwhile, the properties of the other materials were obtained from literature sources.

Material	*E [MPa]*	*ρ [kg/m^3]*	*References*
CF - Plain weave Fabric Standard Modulus for aesthetic properties fabric	223000	1760	[93]
CF - Plain weave Fabric and UniDirectional ply Standard Modulus for structural performance fabric and UD	240000	1800	[92]
GF - Plain weave Fabric	72000	2540	[94]
Milled CF for inner preform	10000 – 25000	800 – 1200	[95]
Epoxy resin for RTM process	2700	1170	Gurit Prime 180 [96]
Polymeric foam	36	32	Rohacell 31 IG-F [97]
Aluminium alloy	70000	2700	Inserts of composite wheel and casting and forged [98,99]

Table 4: mechanical properties of the fibre, epoxy matrix and foam. From [60]

The finite element models of both wheel types were subjected to a simulation of one cycle of each fatigue test. The multiaxial stress and strain state was gathered and analysed to determine an estimate of the wheel's lifespan for a complete load-revolution time history. The findings will be discussed in Section *3.3 Results and discussion*.

For the calculation of the fatigue safety factor of the aluminium wheel, the Dang Van criterion [100,101] for multiaxial high-cycle fatigue was used.

On the other hand, evaluating the fatigue life of the composite wheel is on a higher level of complexity. In this study, the Tsai-Wu criterion [102] was employed to assess the safety margin of the wheel. To determine stress limits for the composite, the static stress was considered as per the methodology proposed by Fuji and Lin [58]. Nevertheless, the outcomes of the fatigue evaluations conducted on the composite wheels should be considered as qualitative and can assist in identifying areas of the wheel that are most prone to failure. However, to obtain an accurate estimation of the wheel's lifespan, additional further investigations are requires.

3.1.1 Cornering Fatigue

As for the physical test of cornering fatigue, also in the FE simulation the tyre is neglected, see Figure 13. The inner flange is fixed along its perimeter, and the centre hub is connected to the loading point, which is 750 mm away [16,31], using a multi-point constraint (RBE2).

A concentrated force is then applied to the loading point to produce the same bending moment as in the experimental fatigue test, based on Equation (3) and Section *2.3.2 Cornering Fatigue test*.

The complete fatigue cycle involves 20 sequential linear static simulations, each with a load applied at 18° intervals. The resultant stress fields have been then combined and processed to estimate the fatigue lifespan of the two types of wheels.

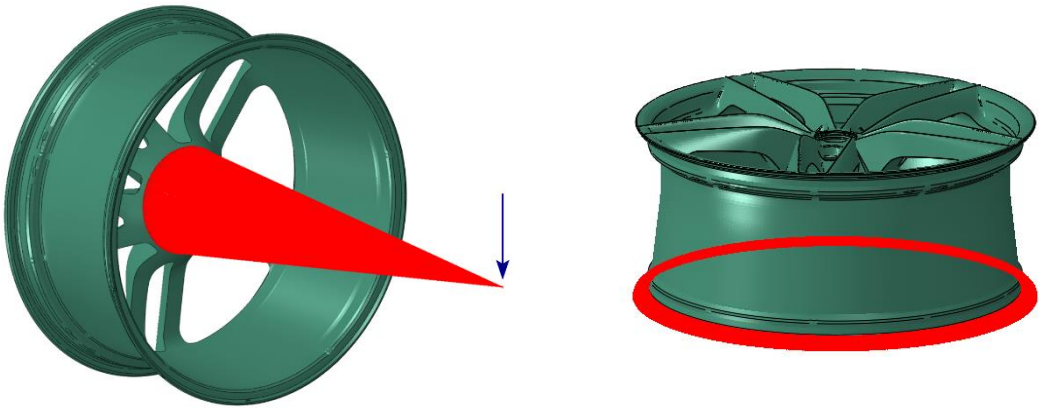

(a) (b)

Figure 13: FE model for cornering fatigue: (a) RBE2 with load, and (b) the fixed constraints at the inner flange. From [60]

3.1.2 Radial Fatigue

The virtual radial fatigue test involves the complete wheel-tyre assembly, and is carried out through a series of three nonlinear simulations:

1. The tyre is mounted on the rim beads as for specification, and the interference fit is simulated,
2. The tyre is inflated up to the operating pressure of 4.5 bar,
3. The driven drum comes into contact with the tyre under the influence of the radial force, and this contact is simulated in a progressive manner.

In the third simulation, the driven drum is modelled by a rigid plane in contact with the tyre in a specific position. Like the previous simulation, the complete rolling process of the wheel on the driven drum is simulated using 20 simulations, where the drum is kept in contact with the tyre on a limited area. The contact points are spaced 18° apart to cover the whole 360° uniformly. The rigid plane is kept in contact with a force that corresponds to the physical test and is calculated by Equation (4).

For the contact between the tyre and the rigid plane, a friction coefficient of 1.3 is employed, whereas the friction coefficient between the tyre and the rim flanges is set to 0.5 [103,104]. These analyses neglect the rolling resistance of the tyre and the camber

angle. The composite and the aluminium alloys are modelled as linearly elastic. The material properties of the tyre and the numerical procedure, which are used to represent its nonlinear behaviour, are taken from the literature [105]. The same mesh employed in the cornering fatigue simulations is adopted also in these simulations.

3.2 Experimental testing

Fatigue tests for both cornering and radial stresses were carried out on the forged aluminium front wheel of Ferrari 488 GTB and on the composite wheel of Ferrari 488 Pista.

The method described in Section *3.1.1 Cornering Fatigue* was employed to perform cornering fatigue test. The turning table test rig (Figure 5a) was utilized to test the composite wheel, while the rotating eccentric mass (Figure 5b) was employed to test the aluminium wheel. The test rig is designed to collect the overall bending stiffness of the wheels throughout the tests. It has been assumed that if the same bending moment is applied, the layout of the test rig does not have any effect on the fatigue life estimation of the component.

In the composite wheels, the structural integrity of the preform and laminates was examined using a non-destructive Computed Tomography X-ray (*CT*) analysis. Four inspections were conducted at different stages:

1) as the End of Line (*EOL*) control – which involves a 100% inspection of all CFRP wheels – before the application of thermal barrier coating,
2) as the Ferrari norms after 250,000 cycles,
3) when the cornering fatigue test machine detects the reaching of the 80% of the wheel initial deflection and,
4) at 1,000,000 cycles.

Before each inspection, the fatigue test was halted and the wheel were removed from the test rig. Subsequently, the wheel underwent the CT scan and when completed, the wheel was remounted onto the test rig, and the bolts were fastened with the initial tightening torque.

The internal damage occurrence and evolution of the wheels were investigated using a X5000 CT scanner by North Star Imaging, with a voltage setting of 250 kV. The wheel was divided into three significant sections, named as A-A, B-B and C-C, which are illustrated in Figure 14, and the results of the investigation will be discussed in the following. These sections, named as A-A, B-B and C-C, are shown in Figure 14. The subsequent failure modes present a summary of the common damages and their progression observed in composite wheels.

The radial fatigue tests were conducted following the standard procedure described in Section *3.1.2 Radial Fatigue* [5,50]. The loads and test duration were chosen according to Ferrari regulations. After the test, the aluminium wheel was visually inspected to detect any damage, while the composite wheel underwent a dye penetrant test to identify any possible cracks of defects.

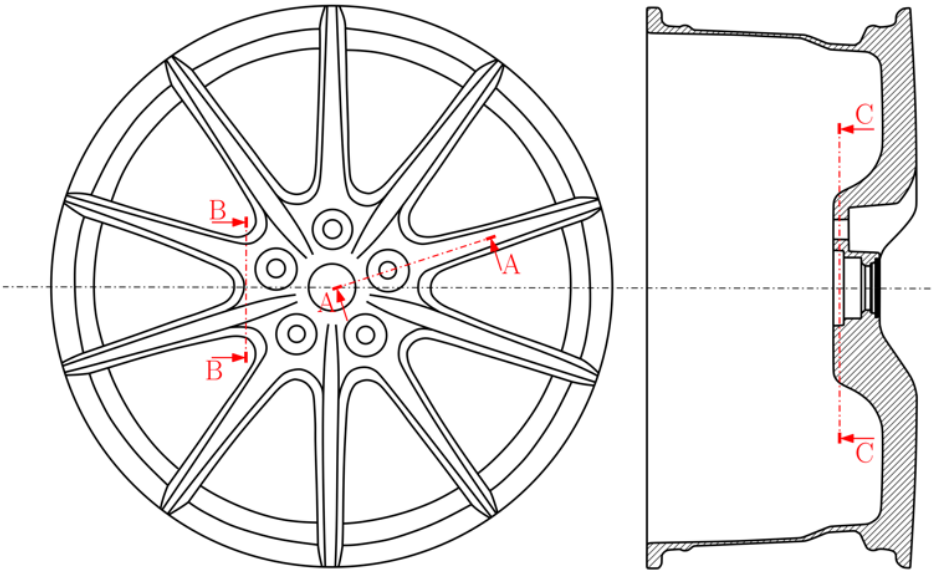

Figure 14: wheel cross-sections analyzed by Computed Tomography. From [60]

3.3 Results and discussion

Figure 15 presents the result of dye penetrant test done after the radial fatigue test on the composite wheel. The test revealed that the wheel did not show any signs of damage after 10^6 cycles. This confirms that the wheel design is overconservative and exceeds the requirements for this particular fatigue test.

(a) *(b)*

Figure 15: dye penetrant test done on the composite wheel rim after the radial fatigue test: (a) front and (b) back views from the vehicle viewpoint. From [60]

The aluminium wheel did not exhibit any signs of damage, indicating that the Ferrari wheels are designed with an excessive margin of safety for the specific test conducted.

Cornering fatigue tests are more critical for sports car wheel designs. This section provides a more detailed analysis of the experimental results of these tests.

After approximately $7x10^6$ cycles, the reference aluminium wheels failed, with only a negligible decrease in bending stiffness, around 3%. Figure 16 presents two distinct failures that occurred in the two aluminium wheels at maximum load ($K = 2.0$) during the cornering fatigue tests. The failures are compared with their numerical counterparts. The first failure (Figure 16a) was a crack initiated at the front edge of a spoke, whereas in the second failure (Figure 16c), the crack began at one of the back edges of a spoke, close to the fillet. In both cases, the crack propagates through the spoke until it fractured the whole cross-section.

The two cracks initiate at the spoke's section where the maximum bending moment is present. The triangular cross-section of the spoke is the primary cause of fatigue cracking at the outer edge, which amplified the stresses in that area. The curvature of the spoke causes the second failure, as reported by Ballo *et al.* [13] and Shang *et al.* [14]. The spoke's curvature acts as a stress concentrator, leading to fatigue cracks that are likely caused by internal material defects. In the forged wheels, the number of punches, as well as their speed and stroke, can be adjusted to reduce these defects, possibly with the help of simulations.

The style of a wheel is an essential design input that is required by the style department and has a significant influence on the subsequent section of the spoke cross-section. Therefore, the initiation of the crack at the outer edge of the spoke becomes inevitable. Finite element simulations are employed to enhance the cross-sectional design of the wheel, thereby extending its lifespan for a justifiable number of cycles, while having minimal impact on the wheel's aesthetic properties. Figure 16b and Figure 16d depict the life expectancy of the aluminium wheel, which is obtained from FE analyses. The contour plot presents the scalar factor, called *Life*, which provides the number of cycles at which failure occurs when multiplied by 250,000. The fundamental unit of 250,000 cycles is selected from the Ferrari requirements for cornering fatigue tests to emphasize the conservative nature of the wheel design. This approach differs from that proposed by [13,25], which directly reports the expected number of cycles.

The minimum expected life of the aluminium wheels is above 19, indicating that the FE simulation predicts failure after approximately $4.9x10^6$ cycles. However, both experimental wheels failed after approximately $7x10^6$ cycles. This implies that the FE simulations are 40% more conservative than the experimental results. The numerical predictions appear to be overconservative, particularly when compared to those present in [15]. This discrepancy is primarily due to the initial fatigue characterization of the aluminium alloy. Thus, the life prediction methodology can be refined by extracting additional samples from the wheel and obtaining a more accurate S-N curve. Nonetheless, the numerically estimated wheel life satisfies the Ferrari requirements and is sufficient to initiate fatigue testing of the wheel.

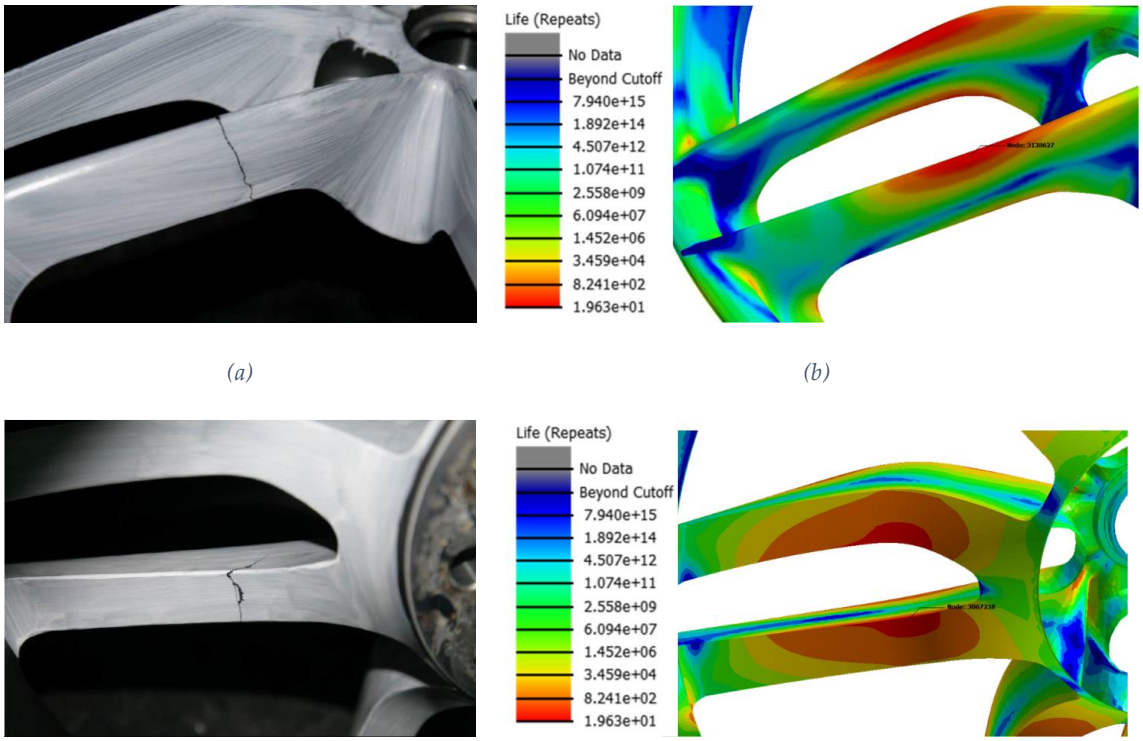

(a) *(b)*

(c) *(d)*

Figure 16: detailed views of 488 GTB aluminium front wheels from the inner vehicle perspective (a, c), fatigue life expectation via FEA (b, d). From [60]

The results of visual inspection of the composite wheel after the maximum level of loading at 250,000 cycles are presented in Figure 17. A superficial damage, like a crazing, is observed at the intersection between two adjacent spokes of the wheel (Figure 17a). Dye penetrant inspections reveal additional cracks at the junction between the spoke and the rim (Figure 17b-c). These cracks are located at areas where the small fillet radius causes a considerable stress concentration. It is noteworthy that these damages are located in resin-rich regions and do not compromise the wheel's structural integrity even after 250,000 cycles.

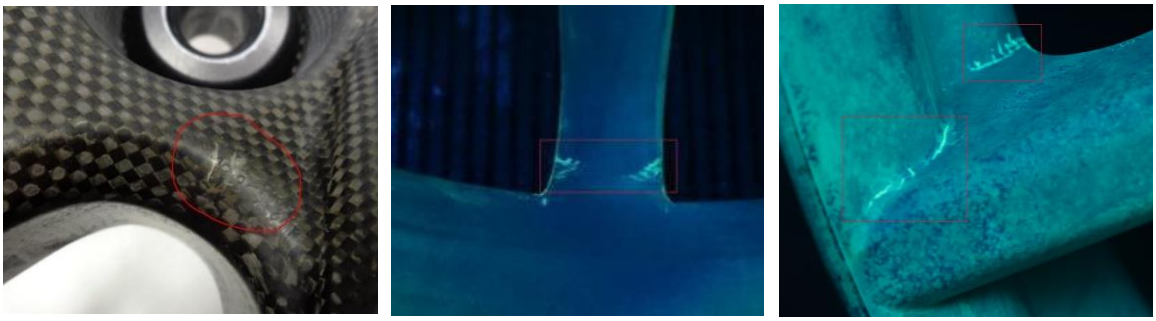

(a) *(b)* *(c)*

Figure 17: failure investigation after 250,000 cycles under cornering loads: (a) at the radiused area between adjacent spokes, (b) and (c) dye penetrants results at the transition between a spoke and the rim. From [60]

As predicted in Section *3.1 FEA simulations*, the Tsai-Wu failure index was utilized to identify the most critical regions of the wheel. The index value ranges from a minimum of 0 to a maximum of 1, identifying the breakage of the matrix. Figure 18 confirms that the critical areas are in agreement with the experimental findings depicted in Figure 17. However, the Tsai-Wu failure index is a static load-based measure of potential composite failure. To extend the wheel's life expectancy for a reasonable number of cycles, the wheel design is tailored to keep the failure index under a reasonable threshold. The effective fatigue life of the wheel will then be verified during the experimental test.

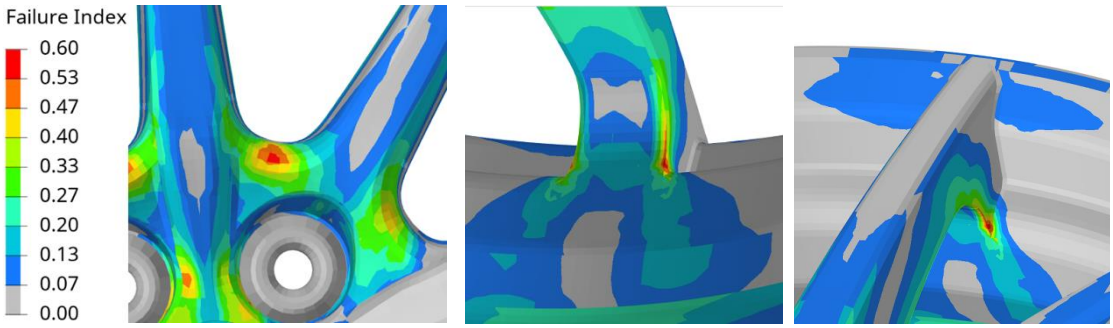

Figure 18: failure index of the composite wheel evaluated at two different locations: (a) between two spokes, (b) and (c) at the same radius between one spoke and the rim, as viewed from the inside (b) and outside (c) of the wheel. From [60]

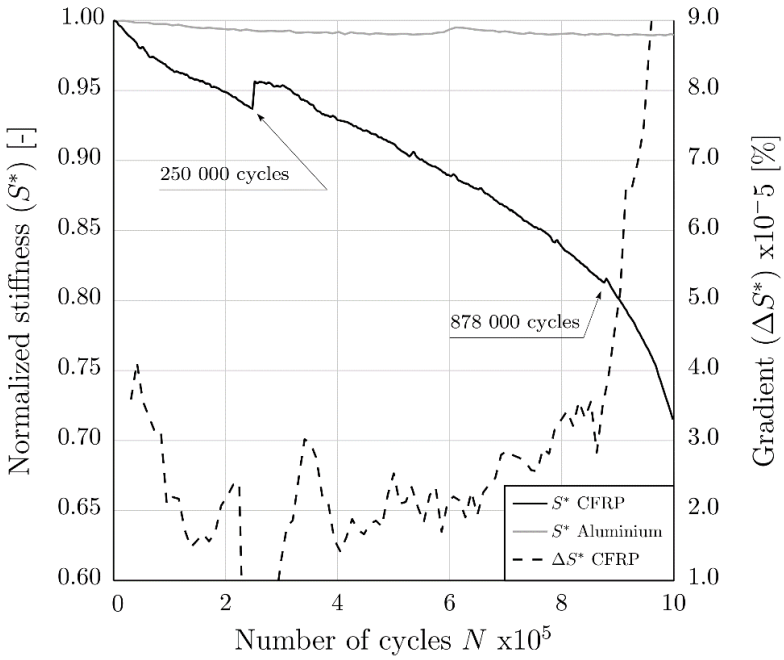

Figure 19: normalized stiffness (S) reduction during the cornering fatigue of the wheels. From* [60]

Despite the fact that only minor superficial and cosmetic damages were observed experimentally, a noticeable stiffness reduction was encountered throughout the cornering fatigue test. Figure 19 depicts the normalized bending stiffness (S^*) of the

composite wheel, with the dashed line indicating the gradient at which the stiffness begins to decrease. To mitigate the effects of measurement noise, a moving average filter over 30 data points was used to smooth the data.

The stiffness reduction encountered throughout the cornering fatigue test is attributed to several factors:

1. inherent *stiffness degradation* of the materials, such as composites and foam, which have been extensively studied in the literature [55,56]. The effect of this degradation can be evaluated by examining the gradient of the stiffness reduction (ΔS^*) curve plot. Specifically, the stiffness gradient curve displays higher values at the start and end of the test, while lower values are seen in the middle,
2. cracks in the internal preform;
3. loss of tightening torque of the bolts.

It is noteworthy that the normalized bending stiffness S^* of the CFRP wheel shows a constant and significant decrease throughout the cornering fatigue test, unlike the reference aluminium wheel which exhibits a different behaviour. Specifically, the S^* of the aluminium wheel remains above 0.9 until a crack initiates on one spoke, resulting in a sudden failure of the wheel.

The gradual failure of the composite wheel may be monitored through the use of a dedicated sensor, which could notify the driver of an impending wheel failure in advance. However, this feature cannot be monitored in any aluminium wheel due to the fast and abrupt nature of the failure mechanism.

In addition, the stiffness reduction of the composite wheel may be mitigated by optimizing the preform manufacturing process, as well as modifying the wheel design and stacking sequence, and enhancing the adhesion between plies and the preform.

Following the CT scans, the initial torque of the bolts was restored, which led to a partial recovery of stiffness observed as a discontinuity of the stiffness curve, as illustrated in Figure 19. This effect was particularly noticeable at 250,000 and 878,000 cycles when the wheel deflection was below 20% of the initial deflection.

The first inspection was carried out prior to thermal spraying of the ceramic coating and machining of the bolted joints (see Figure 20). During this inspection, a 4 mm porosity was detected in the preform at the B-B cross-section, but no additional defects were observed.

The second inspection was conducted according to the OEM standard after 250,000 cycles, and tomography analysis revealed a 7 mm crack in the preform. This was detected at the A-A section's interface between the laminate and preform. In the B-B section, a 15 mm crack was observed originating from the back of the spoke, and the preform appeared to be debonding from the outer laminate. Two cracks were identified in the preform connecting the composite laminate to bolt housing in the C-C section, labelled *a* and *b* in Figure 20, measuring approximately 9 mm and 15 mm, respectively. Crack *b* propagated with a “C-shaped path” and was stopped by the CF laminate around the metal insert at the bolted area.

The third inspection was conducted at 878,000 cycles, corresponding to a 20% decrease in bending stiffness (S^*) of the wheel, a commonly used threshold in many standards. The CT scan revealed that the crack previously observed in section A-A had propagated to 22 mm, spanning the whole width of the spoke. Additionally, a new crack was found at the outer surface of the wheel. In section B-B, the original crack had bifurcated within the preform, reaching a maximum extent of 42 mm. In section C-C, further cracks were observed in the preform, including one near crack *a*, labelled *c*, and another, named *d*, with two inclined branches forming a symmetric bifurcation. The Y-shaped branches extended approximately 41 mm, while its root was 14 mm in length.

The fatigue test was halted after 1 million cycles, during which the S^* decreased by approximately 30%. The tomography revealed the emergence of a new 19 mm crack in section A-A, starting at the radiused root of the spoke. In section B-B, a third 51 mm crack originated from the interface between the preform and the laminate, right at the onset of the pre-existing crack. Red circles in Figure 20 highlight additional damages within the laminate at the outer skin of the spokes, occurring at the overlap between stacked plies covering the preform. Lastly, in section C-C, a new 30 mm crack designated as *e* appeared between two bolted housings laminates.

The cracks in the inner preform were mainly due to manufacturing defects in the preform and incorrect adhesion between the preform and the plies. Improvements in the preform manufacturing process and optimization of Resin Transfer Moulding parameters can potentially decrease the likelihood of these failure events, mitigating the reduction of S^* observed during the test [60].

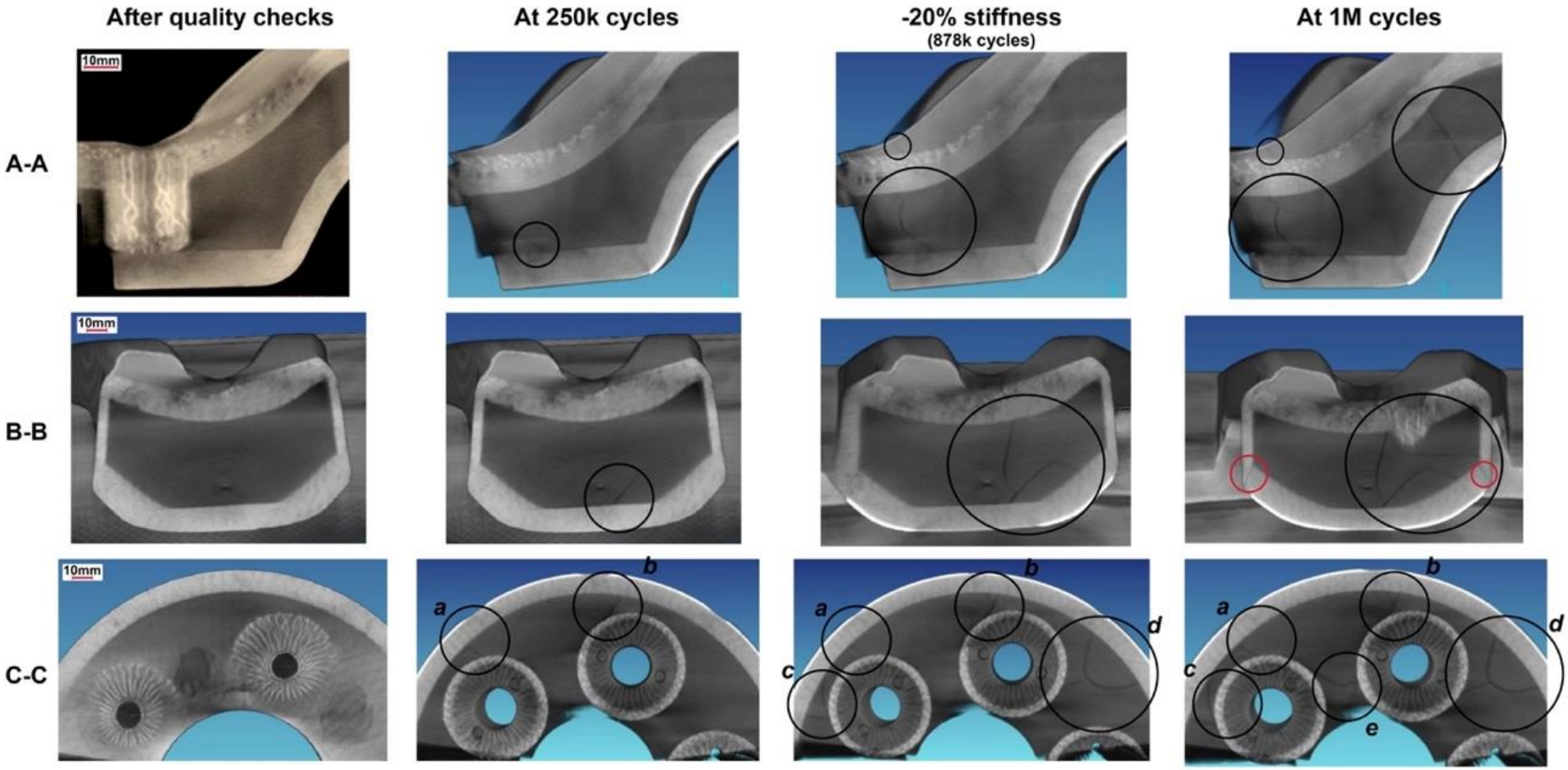

Figure 20: Computed Tomography scans of the composite wheel under cornering fatigue test at various intervals. From [60]

Chapter 4
IMPACT TESTS

Impact tests are usually conducted towards the end of the wheel design process. As a result, any test failures necessitate a time-consuming and unprofitable wheel redesign. To mitigate this risk, the literature has introduced several impact test simulations that inform the wheel design process [69,105–107]. To enhance the predictability of these simulations, dedicated analyses on the striker shape, wheel support structure, and non-linear mechanical properties of the tyre, which majorly affect the simulation outcome, are investigated [108]. However, for composite materials, the reliability of these simulations is in question and is the fourth point of concern in the FMEA. Currently, the impact simulation capabilities using FEA for composite materials remain limited. Therefore, experimental impact tests are still necessary to validate the simulation results and to assess the real impact resistance of composite wheels.

Unlike the preceding and following chapters, for the impact test, the aluminium wheel developed as the standard wheel for the Ferrari 488 Pista is taken as the reference. The reason for this choice lies in the desire to present a true comparison between the two materials for the same vehicle from a customer perspective (see Section *1.2 Ferrari sports car wheel collection*).

As presented in Chapter *1* (refer to Table 1), this wheel has a 10-spoke design different from the 488 GTB forged wheel, optimized in terms of mass with a "*strongly technical*" style not so different from the style of the concept in composite materials.

4.1 Experimental testing in laboratory

Lateral and radial impact tests have been conducted on the forged aluminium and on the composite front wheels of Ferrari 488 Pista. These tests have been carried out in accordance with the standard procedure shown in Section 2.3.1 Impact tests respectively according to SAE J175 [66] and AK-LH08 [67] on homologated test equipment. The loads, those have been chosen according to Ferrari norms, are identical, as for the tyre pressure. After the test, the detection of damages has been revealed by dye penetrant test for both the aluminium wheel and the composite wheel for lateral impact; whereas the radial impact damages have been revealed by visual inspection. Furthermore, the front CFRP wheel for radial impact has been painted white before the test to visually catch immediately all the superficial cracks.

The criteria for declaring the lateral impact test passed are: if no visible cracks that penetrate the entire section of the wheel are revealed, no detachment between the wheel centre and spokes or rim is found, and if the tyre pressure remains unchanged one minute after the test.

The criteria for declaring the radial impact test passed are different depending on the level of the test: at the lowest load, if wheel deflection at the inner rim horn is below a specific threshold; at the second stage if cracks in the deep bed area do not exceed 90° (25%) of the periphery. Additionally, Ferrari also considers it a failure when the tyre de-bead from its position.

4.2 Laboratory test results and discussion

Figure 21 shows the dye penetrant inspection results of the front aluminium wheel for the lateral impact, showcasing both the front (Figure 21a) and the back view (Figure 21b). The aluminium wheel exhibited no issues during this test, as evidenced by the lack of visible dye residue.

(a) *(b)*

Figure 21: dye penetrant for lateral impact on front aluminium wheel: (a) front view; (b) back view

Figure 22 shows the dye penetrant inspection results conducted on the front composite wheel, which sustained lateral impacts on a spoke (Figure 22a) and on a window between two spokes (Figure 22b). These two impact points were located approximately 180° apart. Each point of impact is marked with a "*yellow X*".

Conversely, this composite wheel exhibits damage compared to the aluminium wheel. Red numbers and letters indicate the points of failure. Figure 22a and Figure 22c show the impact on the spoke, revealing two types of damage: three superficial cracks visible from the front view (Figure 22a) and cracks on the spoke-to-rim connection visible from the rear view (Figure 22c). These areas are more susceptible to stress. Note that the damage (point 1) is only present on the left side of the spoke, while points 2 and 3 are opposite the nearest spokes. Similarly, when the impact hit the window, only one spoke on the left (points 4 and 5) was damaged, with point 5 being the most severe. From the rear view (Figure 22c), there are a total of 8 points, labelled D1 to D8 in clockwise order starting from the nearest spoke to the impact. It is more difficult to determine which damages

occurred during which impact, but it is hypothesized that damages D1, D2, D7, and D8 were caused by the impact against the spoke, while damages D3 to D6 were caused by the impact against the window. It is also noteworthy that no damage occurred on the spoke that was impacted. This can be explained by observing the dimensions of the standard SAE J175 [66], which requires an impactor plate with minimum dimensions of 375 x 125 mm. The closest spokes are more involved in the impact resistance, but not the one that was directly impacted.

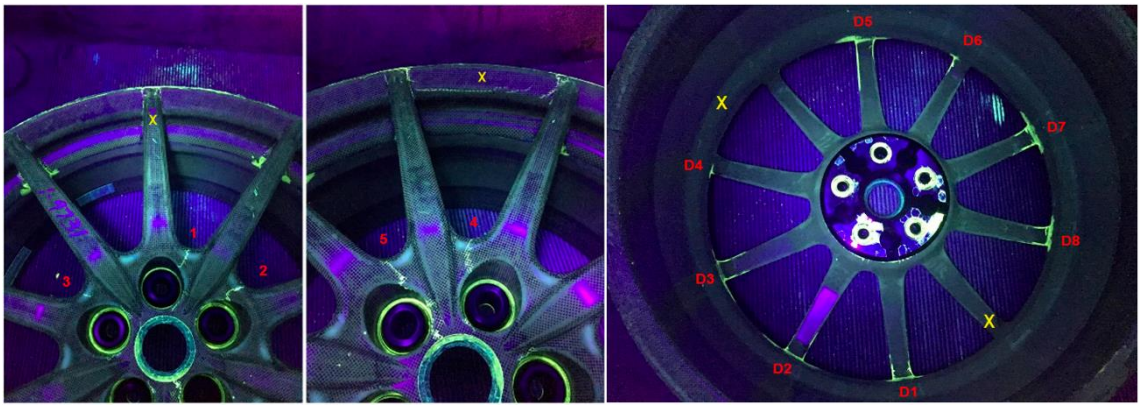

(a) *(b)* *(c)*

Figure 22: dye penetrant for lateral impact on front CFRP wheel: (a) test done on the spoke; (b) test done on the window; (c) back view of the wheel. The yellow "X" identifies where the impacts occurred.

All criteria were met: the cracks were superficial, so these were not penetrating through the complete section, there was no separation between the wheel centre and spokes and the tyre had not lost pressure after one minute.

(a) *(b)*

Figure 23: dye penetrant result of front aluminium wheel tested in radial impact test: (a) front view; (b) back view

Figure 23 presents the results of the radial impact test on the front aluminium wheel. The low load level (K=1.15, referred to as "level 2" in the standard) impact was made on a spoke, while the high load level (K=4.3, referred to as "level 3") impact was made on the weakest point of the rim, corresponding to the window with the tyre valve hole (indicated by the black arrow on the Figure 23a).

As with the lateral impact test, there is hardly any visible damage or even a deformation on the front aluminium wheel after the radial impact test. However, a permanent deformation of 0.08mm had been measured on the inner bead of the rim.

Figure 24 shows the front composite wheel tested under AK-LH08 radial impact standard. Again, this wheel was subjected to two impacts – low and high load – located approximately at 180° apart. Level 3 had been performed on the tyre valve seat.

Figure 24: front composite wheel tested in radial impact

Differently from the aluminium wheel, the composite wheel showed a permanent deformation of 0.1mm under low load (level 2, see Figure 25), despite the absence of any cracks on the beads.

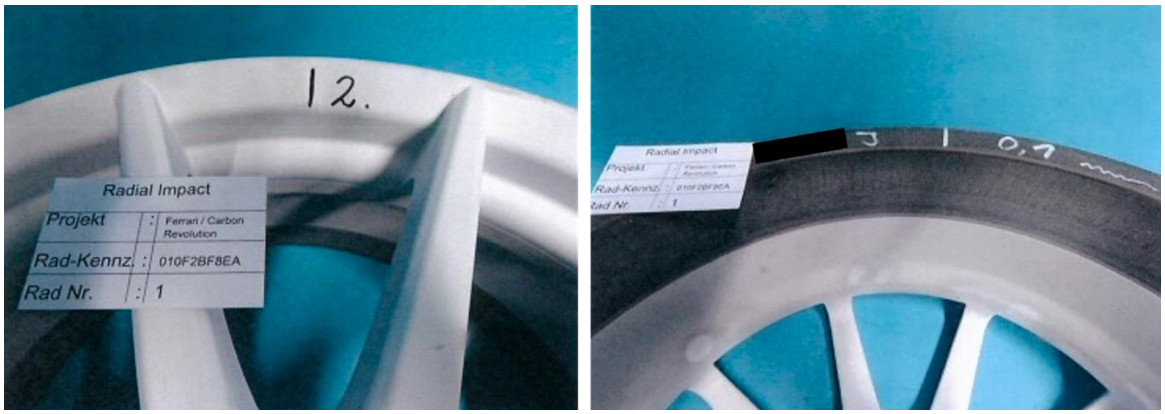

(a) *(b)*

Figure 25: detail of the level 2 impact for the front composite wheel: (a) front view; (b) back view

Different matter comes from the result of high load (level 3): as expected, in this case the amount of damage and the permanent deformation was higher: 2.1mm (Figure 26)

(a) *(b)*

Figure 26: detail of the level 3 impact for the front composite wheel: (a) front view; (b) back view

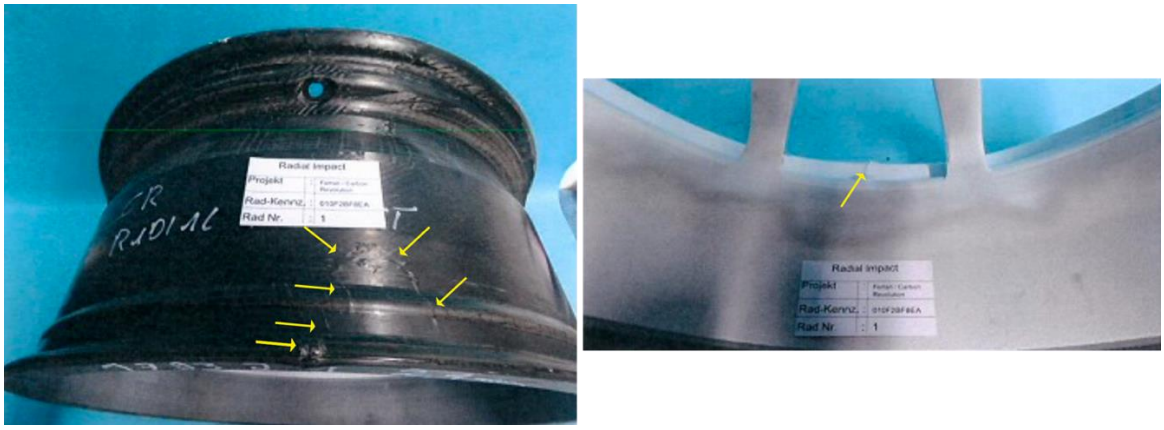

(a) *(b)*

Figure 27: detail of damages on rim barrel for level 3 impact on the front composite wheel: (a) tyre side, (b) brake disk side

The impact resulted in the breakage of both the inner (Figure 26b) and the outer (Figure 26a) beads. Upon closer observation, the outer bead exhibited more cracks, including one that crossed the entire section of the bead (shown in Figure 26a and indicated by yellow arrow in Figure 27b), although this crack only affected the bead itself. On the other hand, the inner bead showed a crack (indicated by the yellows arrows in Figure 27a) that originated in the bead and propagated onto the barrel, along with a circumferential delamination at the end of the bead.

Despite this, all standard criteria were met: at the lowest load, the wheel deflection at the inner rim horn was low; at the second stage the occurred cracks were only localized in a small part of the rim and affect less than 30° of the periphery and the tyre had not de-bead. This corresponds to less than 10% of the rim circumference.

4.3 Experimental test on vehicle

The test benches highlighted a weakness of the CFRP wheels compared to aluminium wheels. Indeed, when visually comparing the two types of wheels, it is clear that aluminium has an advantage over composites. This is because the primary behaviour of the two materials is different, aluminium is ductile while composites are orthotropic and fragile. This difference raises doubt about the safety of composite wheels. To address these concerns and ensure the safety of the component from a customer's perspective, a specific comparison vehicle test had been organized.

Thus, we went to a proving ground, with a Ferrari 488 Pista, with the aims to conduct a comparative test between the structural resistance performance of aluminium and carbon rims, and evaluated the driver experience when impacting a pothole or sidewall at high speed. For this purpose, we chose a proving ground with a straight road, allowing driving at speed exceeding 200km/h, and used a crossbar as the impact. This crossbar was a steel profile measuring 60 mm in height, 100 mm in length and with a radius of 23 mm, oriented at an angle of 115° with respect to the forward direction of the vehicle. This angle was chosen to provide more stress on the inner bead, as the impactor occurred first on the inner bead and then on the outer bead (see Figure 28).

(a) *(b)*

Figure 28: (a) vehicle impacting against crossbar (b) proving ground configuration

The worst-case vehicle configuration was chosen for the test, which involved a 488 Pista spider version in gross vehicle weight configuration, with the steering wheel map set to "*race*" mode. In this mode, the engine torque, power, and turbo output are increased, and the gearbox speed is elevated, while the Electronic Stability Program (ESP), traction control, and side sleep control are reduced to their minimum level of interaction. Additionally, the magnetorheological dampers were set to a higher level of damping curve.

The test was set up to seek for two limit speeds beyond which, during the impact:

- *v1*: speed in which the first plastic deformation or the first damage occurs, without this being perceptible by the driver,
- *v2*: speed for which the damage to the rim can be detected by the customer as an imbalance or as tyre deflation (with TPMS warning lamp turning on).

The test sequence was as follows:

1. accelerate the car up to the preset speed,
2. drive over the obstacle with the right front and rear wheels, keeping the speed constant and the steering wheel straight,
3. slow down with slight deceleration and do a "*U turn*" at the end of the track,
4. accelerate up to $v>200km/h$ then decelerate steadily up to $v=30km/h$ for subjective evaluation,
5. return to the pits, check the wheel integrity,
6. if the wheel is OK, continue the test proceeding to the next speed.

The starting speed was 50km/h, then it must be increased by 10km/h for each test iteration.

Before starting the test, the driver had done some acceleration up to the speed of 200km/h to perceive the vehicle with the new wheels and build his reference. For obvious reasons, the impacts occurred on the same wheel but in different circumferential positions at each speed step.

The subjective measurements were performed by a professional driver and based on the SAE J1441 [109] rating. All the wheels, before the test, were rated 10.

The objective measures were taken during the test in the workshop available at the proving ground, the extent of the out-of-roundness was not measured as geometric but as mass imbalance with the balancer and quantified in terms of mass to be added to re-balance the wheel. Instead, the height of the crack on the inner bead of the CFRP rim was geometrically evaluated as shown in Figure 29. As for the radial impact test, the composite wheel has been painted white to have an immediate visual confirmation about the entity of the damage.

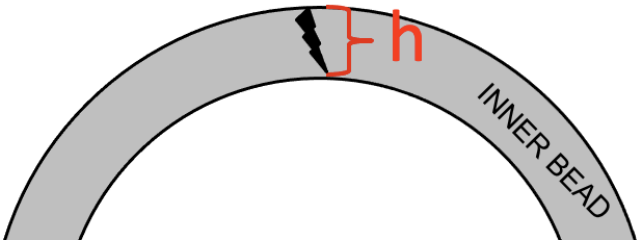

Figure 29: scheme for inner bead cracks detection and height measurement

4.4 Vehicle tests results and discussion

Being aware of the results obtained on the laboratory bench in the lateral and radial impact tests, the following results are not as expected.

On the aluminium wheel, the driver had felt something starting from the first impact at 50km/h. He had not claimed it as a customer complain, thus this was a demerit of 7.

The first critical speed, at which damage occurs without the customer driver noticing, was the same for both wheels: 80km/h. The damage to the aluminium wheel was a slight

ovalization and to the composite wheel a first circumferential crack (see Figure 30). The rating SAE for aluminium wheel dropped from 7 to 5, that means *"borderline"*.

(a) *(b)*

Figure 30: Impact result at speed v1 for (a) aluminium wheel; (b) composite wheel

The aluminium wheel presented an imbalance which requested 15 g on the inner bead to be re-balanced. After that, rating came back to 7.

Conversely, the composite wheel presented a similar behaviour to what had been found in AK-LH08 impact (Figure 27) but the amount of damage turns out to be much lower. It presented a circumferential crack. The driver had felt nothing, thus there was no demerit (rating 10).

The test continued, and at each step, the aluminium wheel showed increasing complaint but still remained within acceptable imbalance on the wheel balancer, while the composite wheel remained complaint-free.

The test ended at 110 km/h. At this speed "*v2*," the complaint became excessive for both wheels and the wheels must be replaced.

In Figure 31, the comparison between aluminium and composites is shown.

The imbalance shown from the aluminium wheel was excessive that the car was not drivable, with a demerit 3.

An attempt was made to re-balance the wheel, but it was not successful due to the amount of mass required exceeding the maximum value allowed by the OEM's standards.

The CFRP wheel, instead, did not cause the driver to complain about imbalance, but after 30 minutes the warning lamp from the Tyre Pressure Monitor System (TPMS sensor) turned on indicating an air leak from the rim barrel at a rate of about 0.7 bar/h. Indeed, the amount of damage on the inner bead (Figure 32a-b) and on the rim (Figure 32c) can be seen in Figure 32.

(a)

(b)

(c)

(d)

Figure 31: impact results at speed v2: (a) – (c) aluminium wheel; (b) – (d) composite wheel

(a) *(b)* *(c)*

Figure 32: details about front composite wheel impacted: (a) global view, (b) what is visible when the tyre is fitted, (c) rim barrel

The cracks on the composite wheel were mainly circumferential, on both the outer and the inner bead. The crack on the inner bead had a radial depth of only 0.2mm, which could be the reason why the driver perceived nothing. The demerit was always 10. In Table 5 the demerit for both wheels are presented.

Speed [km/h]	*Post-impact demerit*	*After re-balancing demerit*
50	7	
60	7	
70	6	
80	5	7
90	6	
100	5	
110	3	5

(a)

Speed [km/h]	*Post-impact demerit*
50	10
60	10
70	10
80	10
90	10
100	10
110	10

(b)

Table 5: professional driver demerit after impact test at increasing speed accordingly to SAE J1441 (a) for aluminium wheel and (b) for composite wheel

The interesting discovery is that the behaviour of the two types of wheels is completely different, and that CFRP wheels are judged even less of a safety concern. This is because any anomalies can be detected early on through the TPMS sensor, prompting the customer to check and inflate the rim even if the damage is small.

Chapter 5
WHEEL ATTACHMENT

5.1 Wheel assembly overview

The wheel rim is connected to the vehicle through five conical screws, named wheel bolts. These wheel bolts secure the wheel rim to the hub bearing by passing through the brake disk, as shown in Figure 33; in this way the wheel is free to move and rotate independently from the suspension unit. The only way for the wheel to transmit motion generated by both the brake disk during braking and the hub bearing during accelerating is through friction between the wheel rim and the brake disk. This requires a proper preloading of the bolts to generate a distribution of tangential friction forces sufficient to transmit the braking and accelerating torques without inducing shear or bending stresses on the bolts, as presented by Parisen [110]. This preloading must have values within a certain range, the lower limit of which is established by the minimum preload necessary to achieve correct fastening without sliding. This lower limit can be calculated by knowing with sufficient approximation the friction coefficient of first sliding between the surfaces in contact, along with the properties of the threaded connection, with sufficient accuracy.

Varin reports that in early 1970s, prior to the advent of cast and forged aluminium wheels, the frequency of accidents attributable to wheel attachment failures was extremely low [111]. According to him, the main reason behind the increase in frequency of failures was in the stiffness of the joint that required more stringent installation and maintenance standards. In details, Bailey et al. [112] presented a report of 1992 from National Transportation Safety Board where it is reported that 82% of accidents due to the loss of a wheel were caused by incorrect tightening, of which 59% due to excessive degradation of the tightened surfaces, 10% due to incorrect torque below the requirements and 3% due to obvious human errors. Only the remaining 18% is due to excessive loads or their increase due to acceleration, braking, vibration or wheel imbalance.

Confirmation that surfaces degradation can be one of the main causes of tightening failure is provided by Croccolo *et al*. [113]. Thanks to a DOE performed between zinc plated steel screws and aluminium bolted joints with different roughness, process (aluminium cast or forged) and surface finishing (spray-painted or anodized), they verified the influence of these parameters on the friction coefficient between components, demonstrating experimentally that the influence of surface finishing and lubrication can lead to a variation of the preloading force up to 320%.

As regards the maximum acceptable limit before damaging the screw, VDI2230 [114] suggests setting the proof stress S_p at 90% of the yield value. Through the simple relationship it is possible to trace the maximum preload [115]:

$$P_{max} = \frac{A_{th} * S_p}{SR} \tag{6}$$

where A_{th} corresponds to the area of the thread core diameter and SR corresponds to the stress factor, intended as the ratio $SR = \frac{\sigma_{EQ}}{\sigma_{ax}}$ between the equivalent stress value calculated with the Von Mises criterion and the stress generated by pure axial tension on the screw.

The maintenance of the preloading force over time must be guaranteed not only for a single tightening, but also for the subsequent ones. To ensure a useful life of the rim of at least ten years, it is necessary to maintain the preloading force for multiple screwing operations, such as two annual tyre changes that would require at least 20 screwing operations. This can be achieved by determining the correct value of tightening torque and monitoring the friction coefficients involved tightening after tightening.

Furthermore, from the FMEA activity, it is known that not only is the fastening crucial, but also the thermal effects on the tightening cannot be ignored. Although the tightening always takes place at room temperature, the wheel assembled on the vehicle can experience high temperatures generated by the braking system, even if only for a few instants. It is important to consider this effect since it can increase the "*creep effect*" of the joint, as presented by Varin [111].

In the first part of this chapter, the differences between the connection of the forged aluminium wheel and the composite wheel are analysed through the analytical analysis of the coupling. The aim of this study is to determine the minimum preload required to ensure adherence of the rim to the brake disk and to verify the maximum dynamic loads on the wheel bolts for both aluminium and composites wheel. In the second part, laboratory and vehicle experimental tests are presented, which were conducted to evaluate the bolts preload and creep effect.

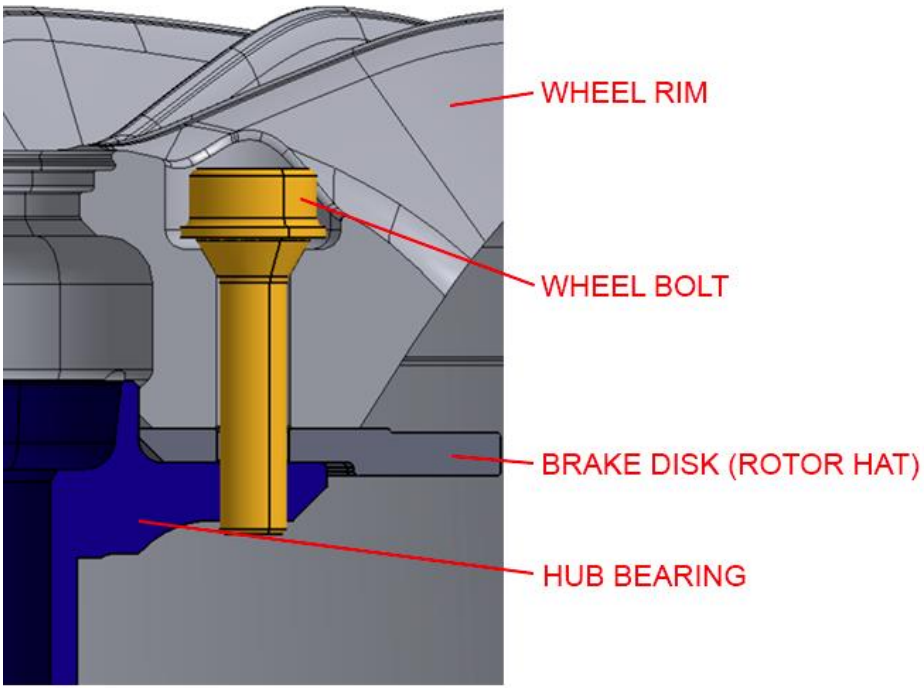

Figure 33: section of the wheel bolt installation with components named

In the Ferrari's vehicle considered, the wheel bolt is tightened on the rim and the hub, with the interposition of the rotor hat. The wheel rim, the brake disk and the bearing form the bolt tightening clamped members (Figure 33). In particular, the wheel attachment components are made of the following materials:

- Screw: titanium Ti6Al4V, tapered underhead and rolled thread, cone seat roughness Ra<0.8,
- Hub: steel 100Cr6 [116], zinc plated,
- Aluminium wheel: Al6082-T6, cone seat roughness Rz<16, not anodized, not painted, manual application of Molykote D321R,
- CFRP wheel – insert: Al7075-T7351 [117], cone seat roughness Rz<16, hard anodized, manual application of Molykote D321R.

5.2 Wheel attachment analytical model

As mentioned earlier, the aim is to determine the preload acting on the wheel bolts that ensure the transmission of loads solely by friction. To achieve this goal, an algorithm was integrated based on a pre-existing spreadsheet used to calculate loads on the suspension components.

To calculate the forces exchanged at the ground between the wheel and the vehicle during motion, the following vehicle data are required:

- Geometric, inertial and aerodynamic characteristics of the vehicle,
- Static and kinematic characteristics of the suspensions,
- Tyre characteristics.

Once these data are collected, the forces can be reported to the wheel centre and the load distribution between the five bolts that connect the rim to the suspension unit can be studied.

To determine the status of the wheel connection during multiple operating conditions, the following tightening and wheel assembly data are required:

- Construction material details for wheel rim, bolts and other clamped members,
- Geometric data for wheel rim,
- Static friction coefficient between wheel rim and rotor hat,
- Loaded radius of the wheel,
- Numbers of wheel bolts.

By knowing the acting loads, which are distributed between the bolts and clamped members, the connection status can be determined. Combined manoeuvres are used to simulate tyre capability by varying acceleration in both directions. Although ground load conditions are assumed to be stationary, individual bolts change position and load due to the rotation at vehicle speed.

Summarizing the hypotheses adopted in the calculation of the combined maneuvers are:

- rear drive,

- optimal exploitation of the grip available on the drive wheels during acceleration,
- optimal exploitation of the grip available on the individual wheels when braking, including aerodynamic effects,
- exploitation of the maximum lateral grip available on the less adherent axle (stable vehicle condition),
- linearity of the tyres: constancy of the coefficient of adhesion as the load varies,
- fixed roll axis,
- elliptic approximation of the relation μ_x-μ_y (also known as *g-g* diagram).

The *g-g* diagram for the Ferrari 488 Pista is calculated considering the maximum aerodynamic downforce during braking, Figure 34.

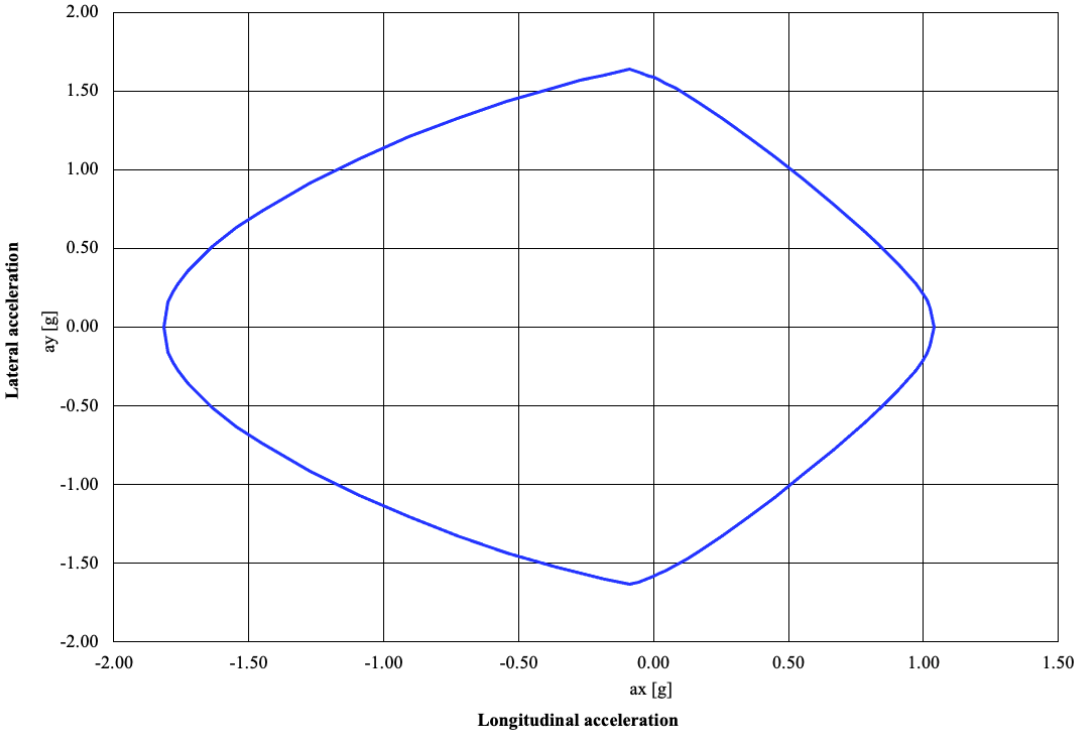

Figure 34: Ferrari 488 Pista elliptic g-g diagram: longitudinal vs lateral acceleration

The determination of the bolt sliding conditions is also based on the following additional assumptions:

- the screws are considered as point elements concentrated at the intersection of the axis lines of the screws with the rim/rotor hat contact plane,
- forces and moments are transported from the point on the ground to the wheel center and finally to the geometric center of gravity of the screws, which are considered to be point-like (see Figure 35),
- tangential forces, which tend to slide the coupling, are uniformly distributed on the screws,

- normal forces, which compress the surfaces in correspondence with the screws, are linearly distributed, equivalent to a linear distribution of the pressures between the coupled surfaces,
- the bending neutral axis on the wheel center is fixed for bending calculation of the flanges. However, the geometry is not symmetrical with the presence of 5 bolts, so the position of the bending axis would be variable,
- the effective normal force acting on the surfaces is calculated using the screw and nut screw stiffness diagrams,
- taking into account the presence of all 5 bolts, the analysis is performed on a single bolt in the different positions described in a circular reference system originating in the center of the wheel (see Figure 36).

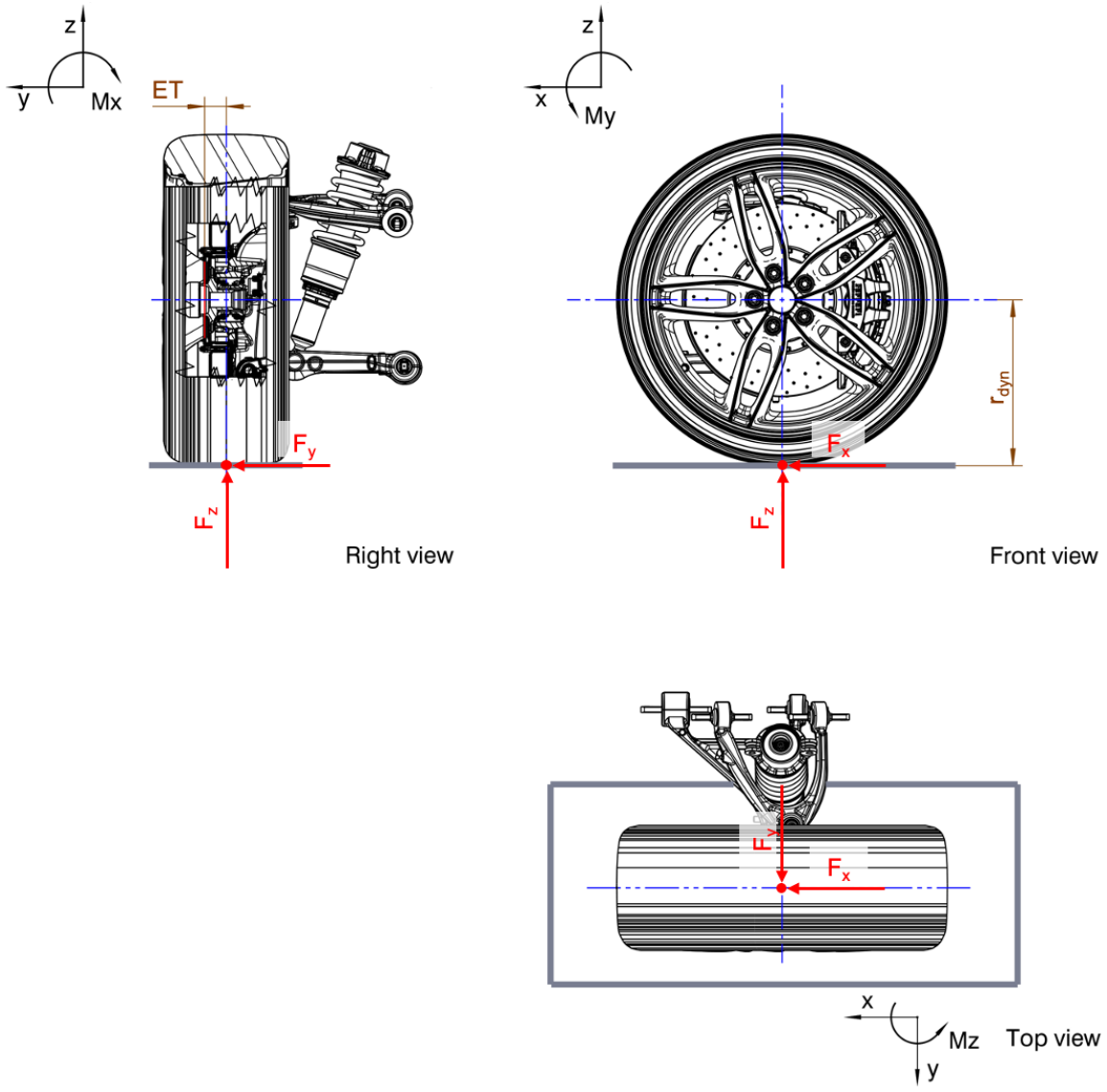

Figure 35: forces applied to contact patch

The loads on the ground coming from the combined maneuvers, called F_x, F_y and F_z, are brought back to the hub in the form of loads and torques. The torque that tends to slide

the hub and rim components relatively is the one around the Y axis, while the one that tends to detach these components is the one around the X axis of the vehicle reference system. The torque around the Z axis, on the other hand, depends on the wheel offset *ET* of the rim, see Figure 2.

The formulas for the transport of the moments in the center of gravity of the bolts are the following:

$$\begin{cases} M_x = -ET * F_z + r_{dyn} * F_y \\ M_y = -r_{dyn} * F_x \\ M_z = ET * F_x \end{cases} \tag{7}$$

where r_{dyn} is the rolling radius of the wheel (see Figure 35).

The forces and moments are considered at the center of the wheel and are redistributed on the individual bolts in the various angular positions θ in proportion to the distances of their axis from the wheel center by bringing the forces back from cartesian to polar coordinates, we obtain the following distribution of normal forces on the single bolt:

$$F_{yi} = \frac{M_z}{r_{wb}} \sin(\theta_i) * \frac{2}{n} - \frac{M_x}{r_{wb}} \cos(\theta_i) * \frac{2}{n} + \frac{F_y}{n} \tag{8}$$

calculated for bolts placed at rotation intervals θ equal to 36° (Figure 36); r_{wb} is the radius on which the bolts are arranged while n is the number of bolts, equal to 5.

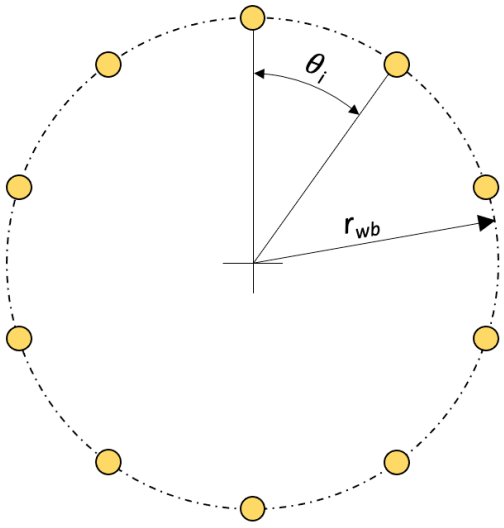

Figure 36: wheel bolts position

In the same way F_{ti} corresponds to the distribution of tangential forces on the single bolt starting from the loads and torques at the wheel center:

$$F_{ti} = \sqrt{F_{xi}^2 + F_{zi}^2} \tag{9}$$

from which it is obtained:

$$F_{ti} = \frac{1}{n}\sqrt{[F_x + \frac{M_y}{r_{wb}}\cos(\theta_i)]^2 + [F_z - \frac{M_y}{r_{wb}}\text{sen}(\theta_i)]^2} \tag{10}$$

The normal forces F_{yi} on the bolts come from external loads acting on the wheel, which are distributed between bolts and clamped members in proportion to their stiffness: the greater the stiffness of the component, the greater its share of external load absorbed.

Based on the known stiffnesses of bolt and clamped members, K_{wb} and K_m respectively, the calculation of the distribution of the effective residual forces on contact under the action of an external force takes place:

$$F_{ni} = P - F_{yi} * \frac{K_m}{K_{wb}+K_m} \tag{11}$$

where P is the nominal preload of the screw.

Subsequently, for each angular position θ of the bolts, the ratio $\frac{F_{ti}}{F_{ni}}$ is calculated, which defines the minimum static friction coefficient required to maintain the tightening on the *i-th* bolt. In fact, this coefficient is defined precisely as the ratio between the tangential forces and the effective normal forces acting between the rim and the brake disc hub.

If the static friction coefficient actually available on the vehicle is higher than the minimum value provided by the previous ratio, then the wheel is in a safe condition, otherwise there will be sliding between the clamped surfaces. This check must be carried out for all combined maneuvers. However, when sliding occurs, it is present in only one *i-th* bolt, while the contact must be ensured by the set of all the tightening bolts; for this reason, a minimum value higher than the available one is an alarm which does not affect the coupling, but at the most it can give rise to local sliding or localized deformations on the single area of competence of the bolt.

Therefore, it is essential to check the minimum preload to be guaranteed on all 5 bolts at the same time and to ensure that the following ratio is < *1* for each combined maneuver:

$$I_{ad} = \frac{\frac{\sum F_{ti}}{\sum F_{ni}}}{\mu_{fr}} \tag{12}$$

with μ_{fr} static friction coefficient of wheel rim on rotor hat. In fact, if $I_{ad} > 1$, the slip of the rim from the brake disk would occur with the conditions for the spontaneous unscrewing of the tightening.

Finally, remember that the calculation is performed for both the front and rear wheels separately, but only one minimum preload value is given, as a lower limit for all the vehicle axles. In Figure 37, the workflow for this calculation is presented.

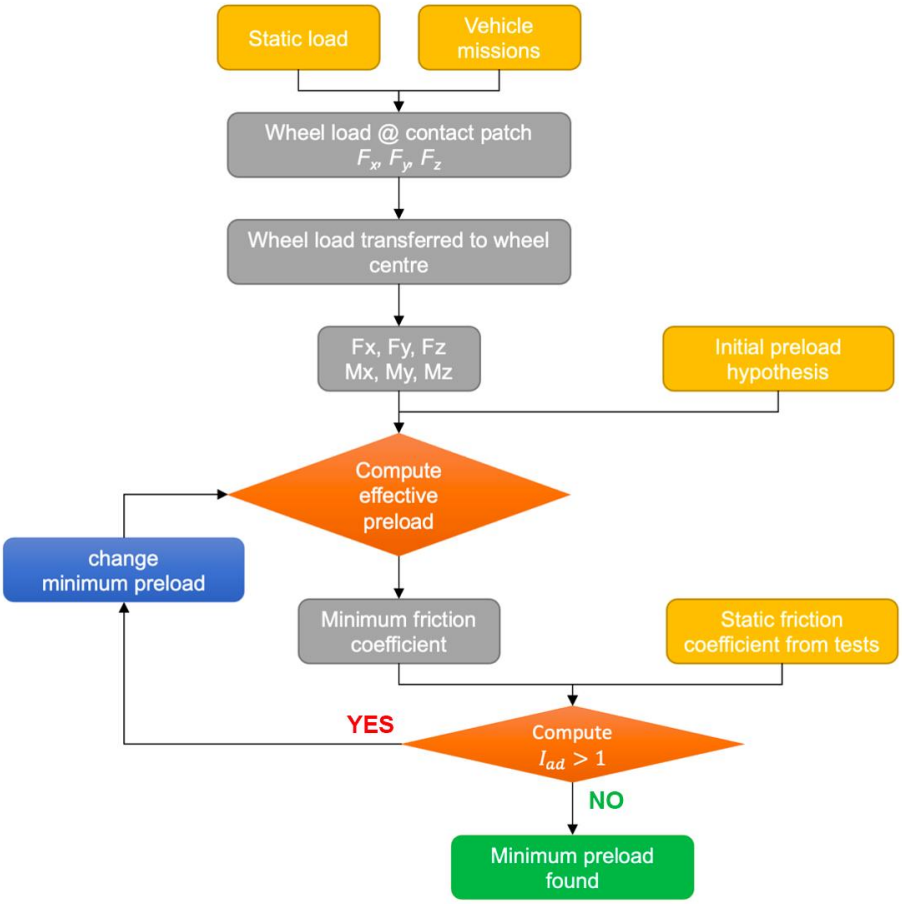

Figure 37: algorithm to calculate minimum preload for wheel bolts

5.3 Bolt and clamped member stiffness calculation

Important features of the tightening and foundations of the analytical analysis are the stiffnesses of the aluminium or composite wheel rim and wheel bolt, respectively. During tightening, the preload generated by tightening the screw brings the bolt itself into tension and the clamped members in compression.

Much has been written and debated about how to analytically calculate the stiffness of the materials involved. While the calculation for the bolt is simple and confirmed by scientific community, it is not that for the clamped members.

5.3.1 Analytical calculation of the bolt stiffness

For the analytical calculation of the stiffness of the bolt, reference is made to Shigley's *"Mechanical Engineering Design"*, which indicates the following calculation approach [118] considered also in [114,119].

From the theory of elastic elements, stiffness is calculated with the equation:

$$k = \frac{EA}{L} \tag{13}$$

In general, the bolt is divided into a certain number of prismatic elements, considered as elastic elements in series; with an overall length L and section A, these sections are all characterized by the same material as the bolt, titanium, with a Young's modulus E equal to 114,000 [120].

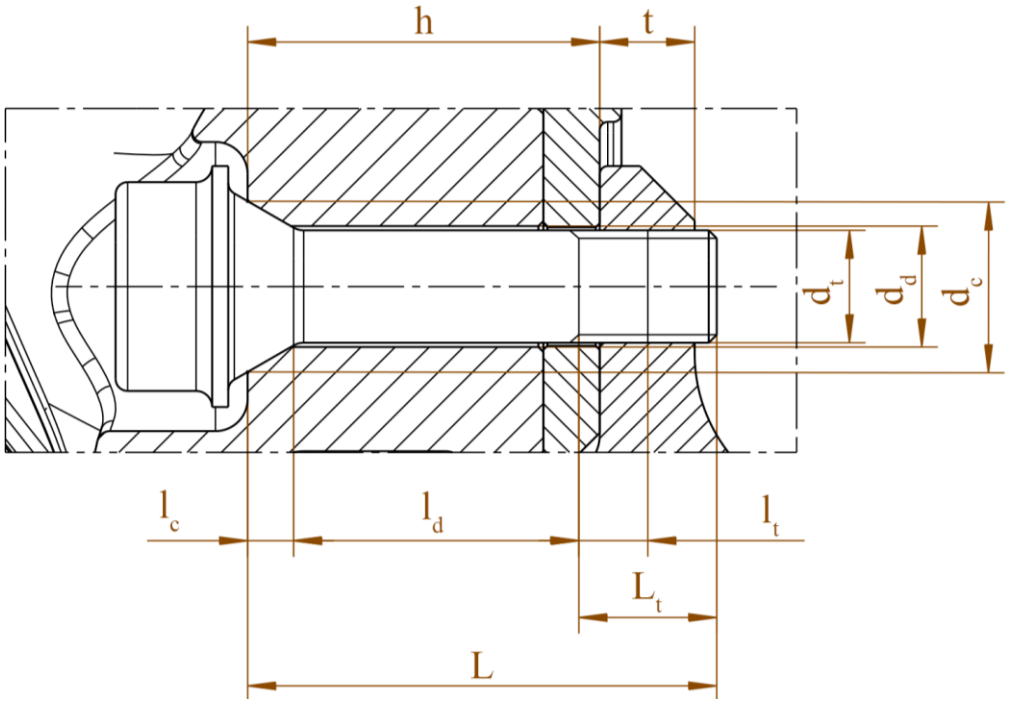

Figure 38: characteristic dimensions for Ferrari vehicle titanium bolt

As it can be seen in Figure 38, the bolt is divided into three sections which contribute to the total stiffness. Once the individual contributions of each section have been estimated, they must be summed up according to the formula for the stiffness in series:

$$k_{bolt} = \frac{1}{\frac{1}{k_c}+\frac{1}{k_d}+\frac{1}{k_t}} \tag{14}$$

Especially, it can be distinguished three sections: conical, cylindrical, and threaded.

For the conical section, it is calculated with the average area of the cone:

$$k_c = \frac{E\frac{\pi}{4}\left(\frac{d_c+d_d}{2}\right)^2}{l_c} \tag{15}$$

Even easier is the calculation of the non-threaded cylindrical section:

$$k_d = \frac{E\frac{\pi}{4}{d_d}^2}{l_d} \tag{16}$$

While for the cylindrical threaded section it is necessary to consider the actual length of the thread in the socket, in our case equal to half the thickness t[1]:

$$k_t = \frac{E{A_t}^2}{l_t} \tag{17}$$

with d_t thread diameter obtainable from standard tables [121].

Titanium wheel-bolt material and geometry			
Elastic modulus Ti6Al4V [120]	**114.000**	*MPa*	*E*
Bolt thread	**M14 x 1.5**	-	
Threaded diameter [121]	**13.03**	*mm*	d_t
Nominal threaded area [121]	**125.00**	mm^2	A_t
Threaded length	**16.00**	*mm*	L_t
Pitch [121]	**1.50**	*mm*	*p*
Bolt diameter (unthread)	**14.00**	*mm*	d_d
Length of unthreaded portion	**36.00**	*mm*	l_d
Max cone diameter	**21.20**	*mm*	*dc*
Cone length	**8.70**	*mm*	

[1] Since the hub is a through thread and cannot be considered as a nut, if $t < d$ it is considered a socket thread $t/2$, if instead $t < d$ it is considered a socket thread equal to $d/2$.

Vehicle installation geometry			
Length of bolt installed	**58.50**	*mm*	*h*
Hub thickness (female thread)	**11.80**	*mm*	*t*

Calculations			
Cone length in grip	**6.50**	*mm*	l_c
Length of unthreaded portion in grip	**43.40**	*mm*	l_d+l_c
Length of threaded portion in grip	**7.40**	*mm*	l_t
Stiffness of threaded portion in grip	**1,925,676**	*N/mm*	k_t
Stiffness of cylindrical section	**487,470**	*N/mm*	*kd*
Stiffness of conical section	**4,266,843**	*N/mm*	k_c
Titanium wheel-bolt stiffness	**356,497**	***N/mm***	$\boldsymbol{k_{wb}}$

Table 6: wheel-bolt stiffness calculation

5.3.2 Analytical calculation of the clamped members stiffness

On the other hand, for the calculation of the clamped member stiffness there are different theories proposed. Thanks to the literature analysis carried out by Brown *et al.* [122], it is possible to summarize the shape of the elastic deformation volume in essentially two categories: cylindrical and conical.

According to Bickford [123], the volume of material of the clamped members subjected to elastic compression has a cylindrical shape. Same hypothesis is also taken into consideration by Pulling *et al.* [124] with the difference that in this case the compressed material is not considered as compressed but as flexed, imposing a second factor q equivalent to $q = \frac{d}{d_d}$ that correspond to the gap between the diameter of the shaft of the bolt and the diameter of the hole. However, these theories are strongly influenced by the estimation of the Q factor, being this latter squared in Brickford's case and to the fourth in Pulling *et al.*'s case, with a plausible error.

Alternatively, Rötscher theorizes that the shape of the elastic deformation volume is conical with an angle of 45 °. Niemann, in his treatise *"Machinenelemente"* [125], argues that this angle is too large and not representative of the real volume of elastic deformation, also confirmed by Little [126]. In fact, according to Niemann, the stiffness of the clamped members can be calculated only for simple case, or for more complex cases but only approximately. Niemann reports in an interesting figure shown here and taken from his book, Figure 39, several hypotheses of elastic deformation volume:

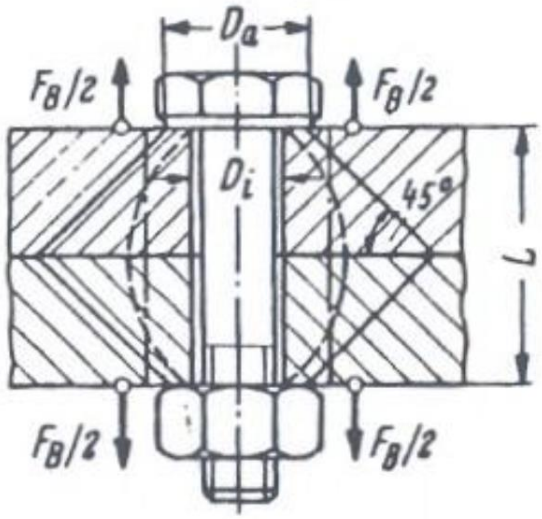

Figure 39: elastic deformation volume for: continuous curve: "Rötscher cone", dashed curve: calculated Fritsche paraboloid, line section - point: theoretical cylinder with equivalent area [125].

- continuous curve: "Rötscher cone",
- dashed curve: calculated Fritsche paraboloid,
- line section – point: theoretical cylinder with equivalent area.

Thus, Niemann chose to evaluate the stiffness in an approximate way, according to the Fritsche paraboloid. Another negative aspect to consider in the "Rötscher cone" theory is that it can only work with material diameters around the screw hole $\geq d_i L$.

The limits of the "Rötscher cone" described above have led to both Juvinall, [127], and Shigley, [118], to theorize a lower conical opening. Shigley, in "Mechanical engineering design" [118], reports that the optimal angle should be contained between 25° and 33° [128].

To get a simplified analytical model of the joint stiffness, Shigley's method has been used.

For the convenience of readers, only the final formulation is proposed here and therefore for an exhaustive understanding, it is suggested that the reader refers to [118].

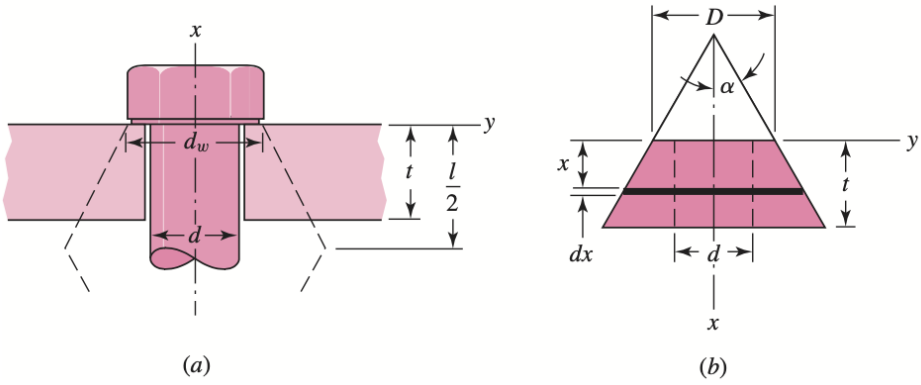

Figure 40: (a) representation of the volume of material elastically deformed by compression during tightening; l is the grip length. (b) diagram of the volume of deformed material. From [118]

With the reference of the scheme *b* in Figure 40, the compression of the infinitesimal element of the frustum under a preload *P* it correspond to:

$$d\delta = \frac{Pdx}{EA} \tag{18}$$

where the area of the frustum *A* is:

$$A = \pi\left(r_{ext}^2 - r_{int}^2\right) = \\ = \pi\left[\left(x\tan\alpha + \frac{D}{2}\right)^2 - \left(\frac{d}{2}\right)^2\right] = \pi\left(x\tan\alpha + \frac{D+d}{2}\right)\left(x\tan\alpha + \frac{D-d}{2}\right) \tag{19}$$

By substituting this into (18) and integrating it over the total grip length *l*, it is obtained:

$$\delta = \frac{P}{\pi E}\int_0^l \frac{dx}{\left(x\tan\alpha + \frac{D+d}{2}\right)\left(x\tan\alpha + \frac{D-d}{2}\right)} \tag{20}$$

Thus, the compression of the infinitesimal element is obtained:

$$\delta = \frac{P}{\pi E d\tan\alpha}\ln\frac{(2t\tan\alpha + D - d)(D+d)}{(2t\tan\alpha + D + d)(D-d)} \tag{21}$$

Now, because we search for the stiffness of the frustum, this is obtained by the stiffness formula:

$$k = \frac{P}{\delta} = \frac{\pi E d\tan\alpha}{\ln\frac{(2t\tan\alpha + D - d)(D+d)}{(2t\tan\alpha + D + d)(D-d)}} \tag{22}$$

As mentioned earlier, the angle α can take on different values, from 25° to 33°, and in this dissertation, it is considered equal to an average value of 30°.

Solving the constants using an α angle of 30°, it is obtained:

$$k = \frac{0{,}5774\pi E d}{\ln\frac{(1{,}155t + D - d)(D+d)}{(1{,}155t + D + d)(D-d)}} \tag{23}$$

The calculation method proposed by Shigley refers to a conventional tightening with flat head bolt and hexagonal nut.

Now the problem is divided into three, determining the stiffness of the frustum cones for rim, rotor hat and hub. Then, the individual stiffnesses obtained are composed for the determination of the overall stiffness as springs in series, thus maintaining valid the elastic theory also used in the analytical calculation of the bolt.

In order to calculate each frustum cone, it is necessary to determine: minimum external diameter *D*, minimum diameter of the internal hole *d* and height of the frustum *t*.

The centre of the overall height is considered to determine the maximum opening diameter of the cone and its position. A strong hypothesis at the basis of this method is precisely that the elastic compression cone of the material remains constant both as an angle, 30°, and as a diameter also between the different materials, therefore the frustum cones will have the top and the bottom diameters in common. This hypothesis may be inaccurate due to the strong dependence of the joint stiffness on its own geometry, especially in the case of different materials but similar thicknesses [129].

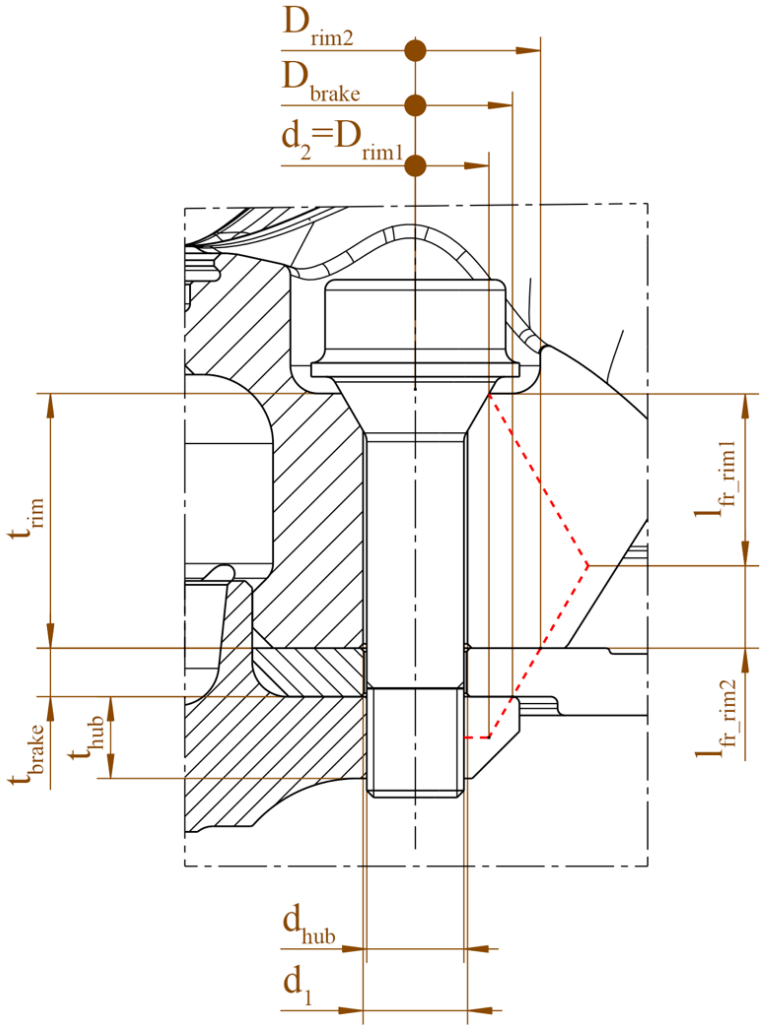

Figure 41: diagram for clamped member stiffness calculation with aluminium wheel

Clamped members material characteristics			
Hub: steel 100Cr6 [116]	**210,000**	MPa	E_{hub}
Brake disk – Rotor hat: Al6082 T6 [130]	**70,000**	MPa	E_{brake}
Wheel rim: Al6082 T6 [130]	**70,000**	MPa	E_{rim}

Geometry of clamped members			
Rim thickness	**37.00**	mm	t_{rim}
Brake hub thickness	**7.00**	mm	t_{brake}
Hub thickness	**11.80**	mm	t_{hub}
Total thickness	**49.90**	mm	t_{tot}
Max wheel bolt diameter contact = diameter frustum rim 1	**21.20**	mm	d_2
Inner diameter	**15.00**	mm	d_1

Frustum: aluminium wheel (top)			
Diameter frustum rim 1	**21.20**	mm	D_{rim1}
Max cone aperture length rim 1	**24.95**	mm	l_{fr_rim1}
Frustum: aluminium wheel (bottom)			
Bottom diameter frustum rim 2 = top diameter frustum brake disk	**36.10**	mm	D_{rim2}
Length frustum rim 2	**12.05**	mm	l_{fr_rim2}
Frustum: hub			
Bottom diameter frustum hub = diameter frustum rim 1	**21.20**	mm	D_{hub}
Inner diameter (thread)	**14.00**	mm	d_{hub}
Frustum: brake disk - rotor hat			
Bottom diameter frustum brake disk = top diameter frustum hub	**28.01**	mm	D_{brake}

Stiffness calculation			
Stiffness frustum rim 1	**1,662,439**	N/mm	k_{rim1}
Stiffness frustum rim 2	**7,167,209**	N/mm	k_{rim2}
Stiffness brake disk – rotor hat	**6,125,041**	N/mm	k_{brake}
Stiffness hub	**10,905,972**	N/mm	k_{hub}
Stiffness of clamped members with Aluminium wheel rim stiffness	***1,004,009***	***N/mm***	$\boldsymbol{k_{rim\_Al}}$

Table 7 - Calculations for joints-member stiffness with Aluminum wheel rim with Shigley's method

Applying the same method to the CFRP wheel, the calculation is more complex, as there are five different frustums: insert frustum, two CFRP frustums, backplate, rotor hat and hub frustums (Figure 42).

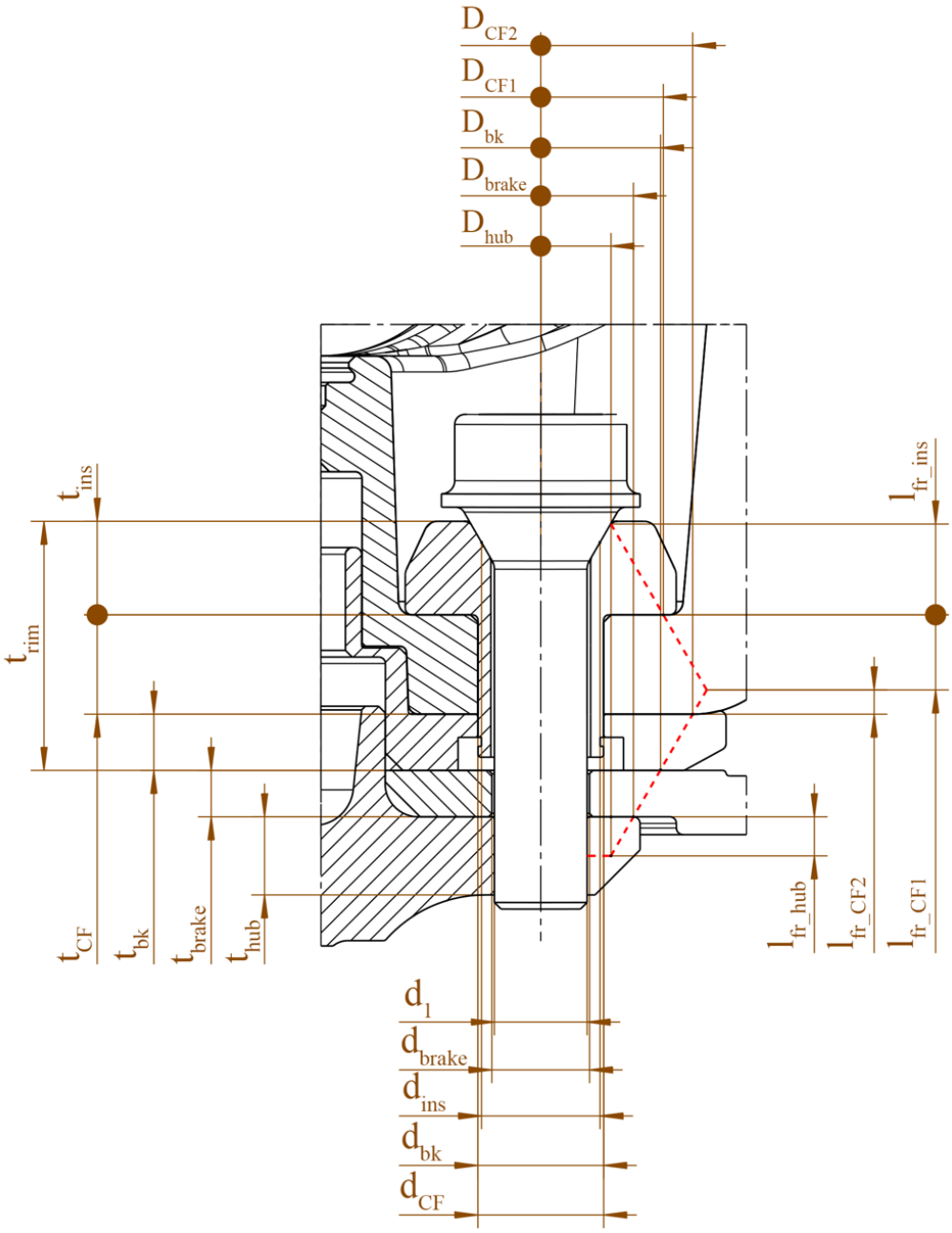

Figure 42: diagram for clamped member stiffness calculation with CFRP wheel

Clamped member material characteristics			
Elastic modulus hub: steel 100Cr6 [116]	**210,000**	MPa	E_{hub}
Elastic modulus brake disk – rotor hat: Al6082 T6	**70,000**	MPa	E_{brake}
Elastic modulus backplate carbon fibre wheel: Al6082 T6 [130]	**70,000**	MPa	E_{bk}
Compressive modulus of carbon fibre[2]	**5,183**	MPa	E_{CF}
Elastic modulus insert carbon fibre wheel: Al7075 T7351 [131]	**72,000**	MPa	E_{ins}

Geometry of clamped members			
Wheel rim thickness	**37.00**	mm	t_{rim}
Brake disk - rotor hat thickness	**7.00**	mm	t_{brake}
Hub thichkess	**11.80**	mm	t_{hub}
Carbon fibre thickness	**15.00**	mm	t_{cfrp}
Backplate carbon fibre wheel thickness	**10.00**	mm	t_{bk}
Insert carbon fibre wheel thickness	**12.65**	mm	t_{ins}
Max wheel bolt diameter contact	**21.20**	mm	d_2
Inner diameter brake disk – rotor hat	**15.00**	mm	d_1
Inner diameter insert (equal to average cone diameter contact)	**18.10**	mm	d_{ins}
Inner diameter CF	**19.15**	mm	d_{CF}
Inner diameter backplate carbon fibre wheel	**19.06**	mm	d_{bk}
Total thickness to be considered in stiffness calcs	**50.40**	mm	g_{tot}

Frustum: insert carbon fibre wheel			
Max wheel bolt diameter contact = diameter frustum insert	**21.20**	mm	d_2
Inner diameter insert (equal to average cone diameter contact)	**18.10**	mm	d_{ins}
Length frustum insert	**12.65**	mm	l_{fr_ins}
Frustum: carbon fibre wheel (top)			

[2] The wheel supplier provides the compressive modulus of carbon fibre with Gurit resin and 70% of volume fraction, at 140°C and 60% moisture.

Top diameter frustum CF1 = bottom diameter frustum insert	**35.81**	mm	D_{CF1}
Inner diameter CF	**19.15**	mm	d_{CF}
Length frustum carbon fibre 1 (top frustum)	**12.30**	mm	l_{fr_CF1}
Frustum: carbon fibre wheel (bottom)			
Top diameter frustum CF2 = bottom diameter frustum CF1	**47.64**	mm	D_{CF2}
Inner diameter CF	**19.15**	mm	d_{CF}
Length frustum carbon fibre 2 (bottom frustum)	**2.70**	mm	l_{fr_CF2}
Frustum: backplate carbon fibre wheel			
Top diameter frustum backplate = bottom diameter frustum CF2	**36.10**	mm	D_{bk}
Inner diameter backplate carbon fibre wheel	**19.06**	mm	d_{bk}
Length frustum backplate	**10.00**	mm	l_{fr_bk}
Frustum: brake disk – rotor hat			
Top diameter frustum brake disk = bottom diameter frustum bk	**28.01**	mm	D_{brake}
Inner diameter brake disk – rotor hat	**15.00**	mm	d_1
Brake disk – rotor hat thickness	**7.00**	mm	l_{fr_brake}
Frustum: hub			
Diameter max frustum hub	**21.20**	mm	D_{hub}
Inner diameter (thread)	**14.00**	mm	d_{hub}
Real length of active thread in frustum hub	**5.90**	mm	l_{fr_hub}
Stiffness calculation			
Stiffness frustum insert	**1,656,999**	N/mm	k_{ins}
Stiffness frustum carbon fibre wheel (top)	**465,579**	N/mm	k_{CF1}
Stiffness frustum carbon fibre wheel (bottom)	**3,092,819**	N/mm	k_{CF2}
Stiffness frustum backplate	**7,390,460**	N/mm	k_{bk}
Stiffness brake disk – rotor hat	**6,125,041**	N/mm	k_{brake}
Stiffness hub	**10,905,972**	N/mm	k_{hub}
Stiffness of clamped members with Carbon Fibre Reinforced Polymers wheel rim stiffness	***288,604***	***N/mm***	$\boldsymbol{K_{rim\_CF}}$

Table 8: calculations for joints-member stiffness with Carbon Fibre Reinforced Polymers wheel rim with Shigley's method

Therefore, the values considered in the calculation of the tightening of the wheels to the vehicle are summarized in Table 9: resuming stiffness values for bolt and different rim materials.

Titanium wheel-bolt stiffness	**356,497**	N/mm	k_{wb}
Stiffness of clamped members with Aluminium wheel rim	**1,004,009**	N/mm	k_{rim_Al}
Stiffness of clamped members with Carbon Fibre Reinforced Polymers wheel rim	**288,604**	N/mm	k_{rim_CF}
Clamped members coefficient with Aluminium wheel rim	**0.74**	$\frac{K_{tot}}{K_{wb} + K_{tot}}$	
Clamped members coefficient with Carbon Fibre Reinforced Polymers wheel rim	**0.45**		

Table 9: resuming stiffness values for bolt and different rim materials

From a first sight, the stiffness of the CFRP rim clamped members is less than 30% of that obtained thanks to the aluminium rim and 80% of the bolt. Furthermore, the constant characteristic of the clamped members with the aluminium rim is equal to 0.74, while that for the composite rim is equal to 0.45, just over half. Remembering the study from Varin [111], minor stiffness could be better and required less stringent criterion for tightening. This result, when an external axial force is applied, is favourable in terms of the loss of compression between the clamped members. However, it induces higher than the normal stress acting on the bolt. In the following Section *5.5 Analytical results and discussion*, the duty cycle of the bolt is presented.

5.4 Experimental determination of the friction coefficient between rim and rotor hat

The static sliding friction coefficient between the rim and the rotor hat μ_{fr}, both aluminium materials, is a fundamental parameter on which the calculation of the minimum preload of the bolt depends in order to guarantee the correct tightening of the wheel.

To avoid inaccurate predictions and given its strategic importance, it is decided to start an experimental activity with the aim of its determination. The measurements of the static and dynamic friction coefficients are performed with a tribometer (model: CETR UMT-3) in a *"pin-on-disk"* configuration, according to [132]. In general, in this geometry, the circular base of a small cylinder, called *"pin"*, is placed in contact on the surface of a *"disk"*, by applying a known and controlled vertical force F (through a feedback system); the disk is then put into rotation with a constant tangential speed (see Figure 43).

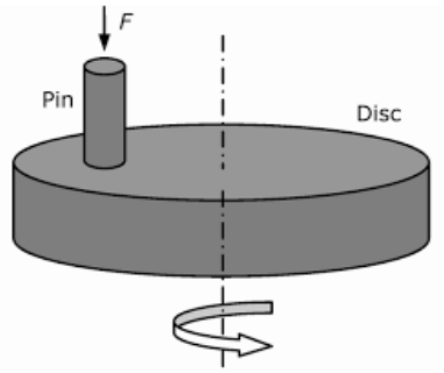

Figure 43: operation diagram of the tribometer in pin on disc configuration [133]

From the measurement of the lateral force that the pin undergoes, it is possible to obtain the coefficient of friction, by calculating the ratio between this and the vertical force applied. From the definition, therefore, the *D-COF* always has a value between 0 (null) and 1 (maximum).

Although we are more interested in the value of the static sliding friction coefficient *(S-COF)*, both measurements were carried out: static and dynamic friction.

Table 10 shows the test parameters used for the two different tests.

Parameter	***Static friction (S-COF)***	***Dynamic friction (D-COF)***
Nominal pressure [*MPa*]	50.95	50.95
Scrolling speed [*mm/s*]	0.1	100
Test duration [*s*]	50	90
Total distance travelled [*mm*]	5	9000
Lubrication	Not present	Not present

Table 10: summary of the working parameters for the two different types of tests

Test samples were realized directly from aluminium wheel rim and rotor hat. Rotor hat is the disk (called *"DISCO D4"*) and wheel rim is the pin (called *"PIN Al"*). Three tests were performed for each coupling, at room temperature.

As mentioned above, wheel rim is made from Al6082-T6, the surface in contact with rotor hat is not painted and roughness specification is Rz > 25μm; while rotor hat is made from same aluminium and heat treatment but with different surface treatment. In fact, rotor hat is hard anodized to be protected from corrosion, but this anodization is not sealed to guarantee the best friction coefficient.

Table 11 shows the results obtained.

Dynamic friction coefficient shows a behaviour with an instant increase of the coefficient to a value of 0.57, after that stabilized. This is mainly because the speed of the disk is

capable of increase the temperature between pin and disk with the consequent strong adhesion between the two components even if hard anodize plays a role in avoiding the sticking of the parts with an even higher increase of the coefficient.

Relatively to static friction coefficient, the first movement of the pin on the disk happened with a friction coefficient of 0.14 but what is interesting is the behaviour: after breaking the adhesion, friction coefficient rapidly increases to an average value of 0.47 after less than 7 seconds of test, corresponding to a 0.7 mm of relative movement.

This last value is the one we are looking for, because in the case of a wheel movement on the rotor hat, the tangential clearance and the stiffness can let the rim move more than 0.7 mm (approximately 40' of rotation).

This result is also valid for the composite wheel because the aluminium of the backplate is the same.

Figure 44: on the left, photo of one disk made from brake hub disk; on the right, photo of one pin made from aluminium wheel rim.

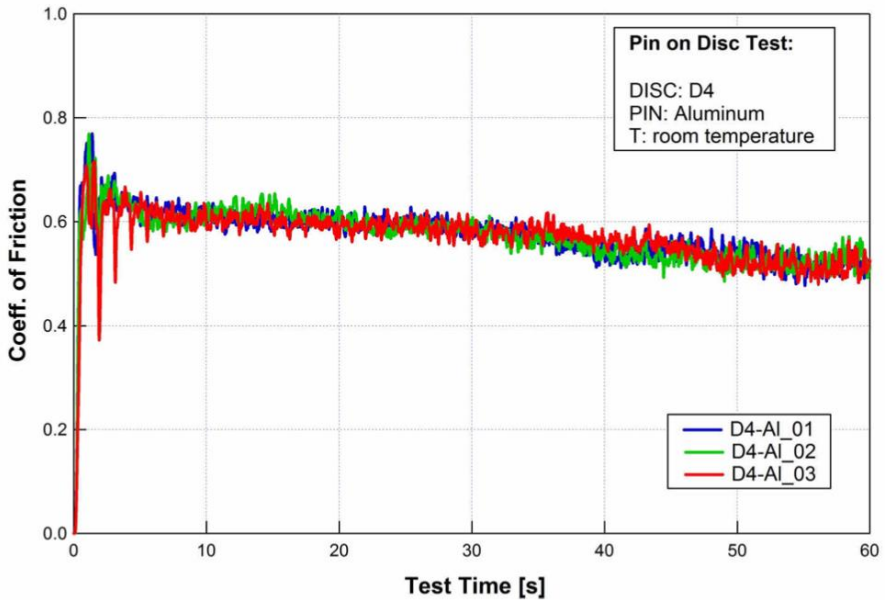

Figure 45: measurement chart of three repetition tests of D-COF

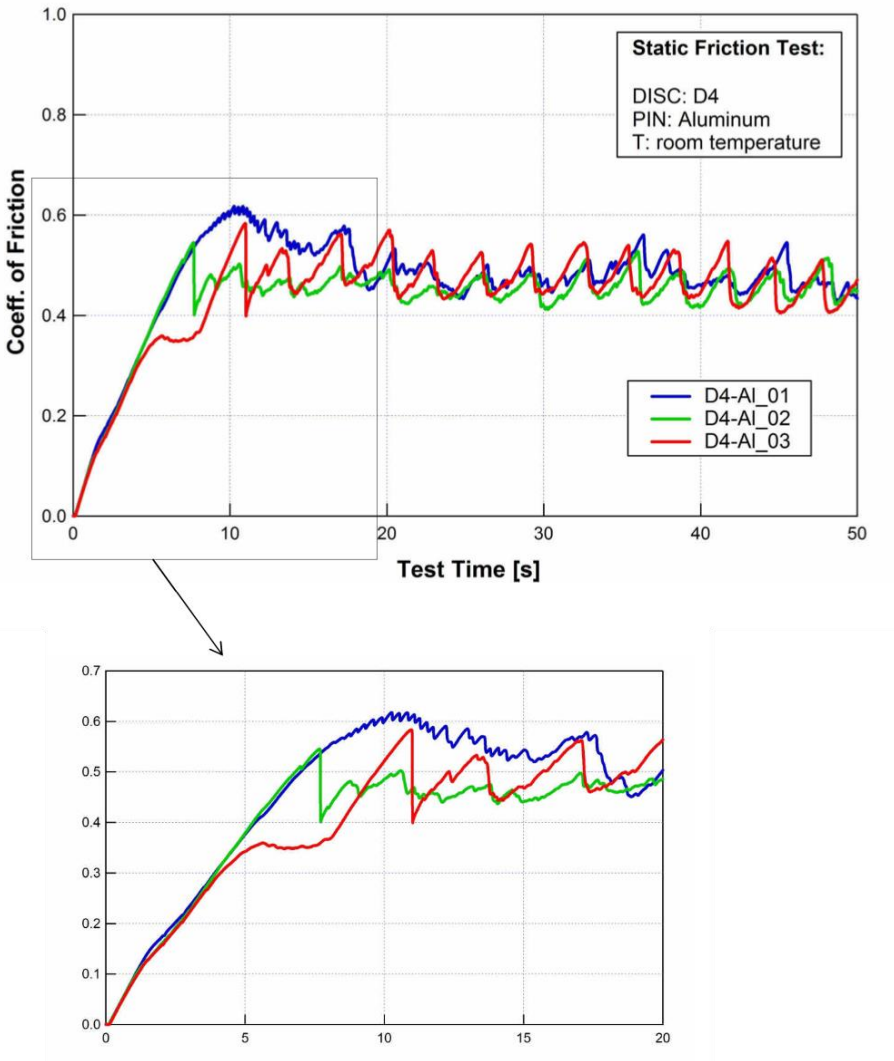

Figure 46: measurement chart of three repetition tests of S-COF with zoom-in for first seconds of test

Coupling	**Temperature**	***S-COF***	***S-COF*** **"breaking adhesion"**	***D-COF***
Pin: Al6061-T6 Disk: Al6082-T6 hard anodized	Room	0.14	0.47	0.57

Table 11: results from the six runs

5.5 Analytical results and discussion

Now that we have determined all the coefficient needed, it is possible to calculate the wheel bolts minimum preload to guarantee the adhesion of the wheel to the vehicle under the Ferrari 488 Pista loads.

Majority of the results presented are dimensionless, all referred to titanium wheel bolt and aluminium rim data.

Summarizing the results obtained in the past sub-chapters into Table 12:

			Ratio referred to Titanium wheel bolts
Titanium wheel-bolt stiffness	**356,497**	*N/mm*	***1.00***
Stiffness of clamped members with Aluminium wheel rim	**999,408**	*N/mm*	***2.80***
Stiffness of clamped members with Carbon Fibre Reinforced Polymers wheel rim	**288,222**	*N/mm*	***0.81***
Clamped members coefficient with Aluminium wheel rim	**0.74**		$\frac{K_{tot}}{K_{wb}+K_{tot}}$
Clamped members coefficient with Carbon Fibre Reinforced Polymers wheel rim	**0.45**		
Wheel bolts coefficient with Aluminium wheel rim	**0.26**		$\frac{K_{wb}}{K_{wb}+K_{tot}}$
Wheel bolts coefficient with Carbon Fibre Reinforced Polymers wheel rim	**0.55**		

Table 12: stiffness for wheel bolt, clamped members with Al rim and CFRP rim and clamped member and wheel bolt coefficients

To get the minimum preload P, it is needed to impose $I_{ad} < 1$ and solve the equation from (8) to (13). The dimensionless results are shown in Table 13:

	Minimum preload P [-]
Aluminium wheel – Titanium bolts	**1.000**
Composite wheel – Titanium bolts	**1.001**

Table 13: minimum wheel bolt preload P to guarantee adhesion between wheel and vehicle hub

This result shows that even if the stiffness of the composite wheel is three times less than the aluminium wheel, the increase in preload is only 0.1%. To understand this, we need to consider the vehicle manoeuvres and imagine which ones are the most aggressive in

causing the wheel to slip on the brake disk: acceleration and braking. In fact, only the longitudinal manoeuvres can generate high tangential forces F_{ti} between the rim and the rotor hat, which can act as shear on the wheel bolts.

Although the minimum preload has been calculated as one value for the front and rear, different preload is required for each. The reader may be surprised to discover that Ferrari 488 Pista brakes even worse than it accelerates. Figure 47 and Figure 48 show the engagement of adherence between wheel rim and rotor hat in bolt tightening for front and rear versus the longitudinal acceleration. The front wheel fills the adherence during braking manoeuvres, while the rear wheel has a good compromise between braking and acceleration with a higher filling of adherence during acceleration, as can be imagined.

Furthermore, with this value of preload $P = 1$, it can be drawn also the classical bolt diagram (Figure 49, Figure 50 and Figure 53, Figure 54). Green line is the bolt stiffness line, while blue and orange are respectively the aluminium wheel and CFRP wheel. As in Table 9, the slope coefficient for composite wheel is less than half of the aluminium wheel.

Figure 50 shows the detail about the 0.1% difference in preload between the aluminium and composite wheels. Even if this result is negligible, the difference in stiffness between the two is not.

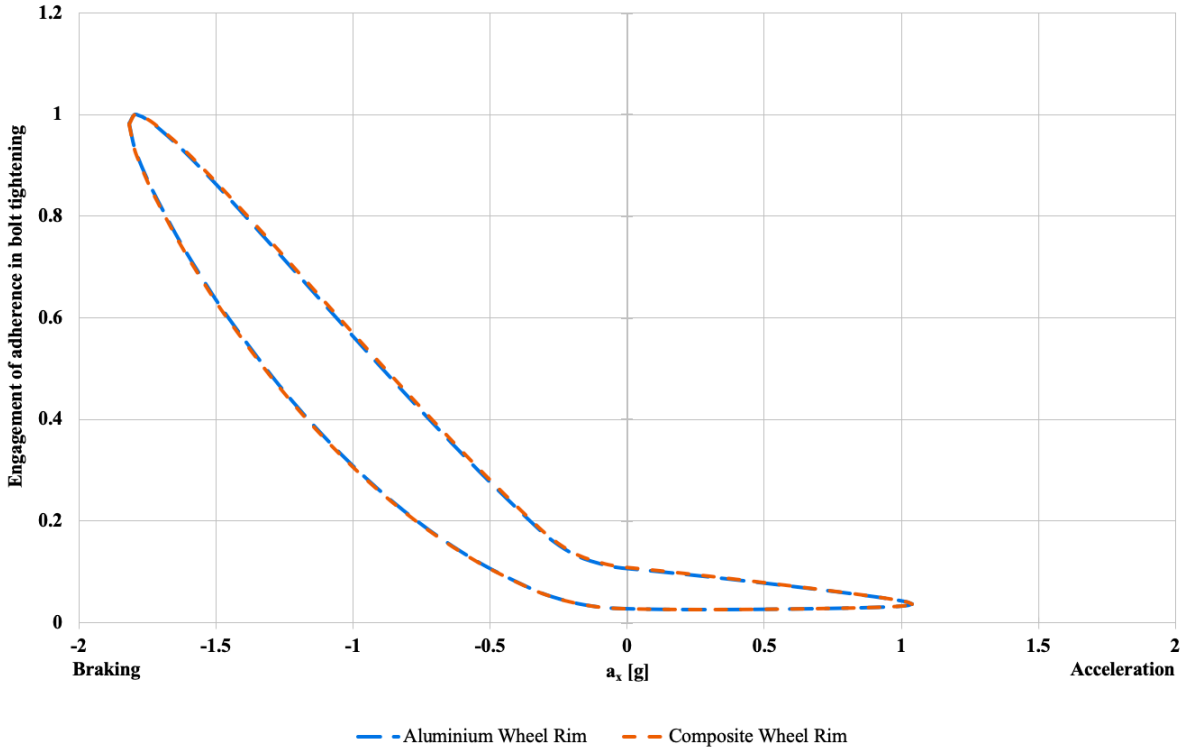

Figure 47: front wheel: comparison of engagement of adherence in bolt tightening for Aluminium wheel versus Composite wheel

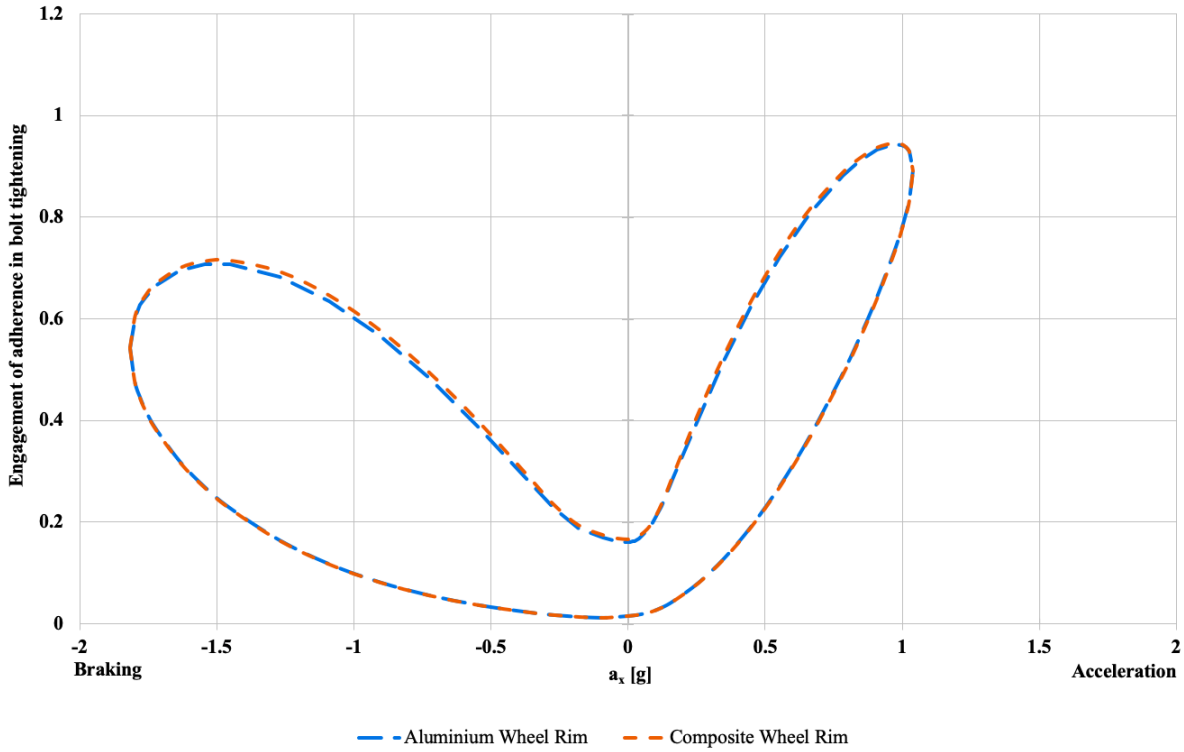

Figure 48: rear wheel: comparison of Engagement of adherence in bolt tightening for Aluminium wheel versus Composite wheel

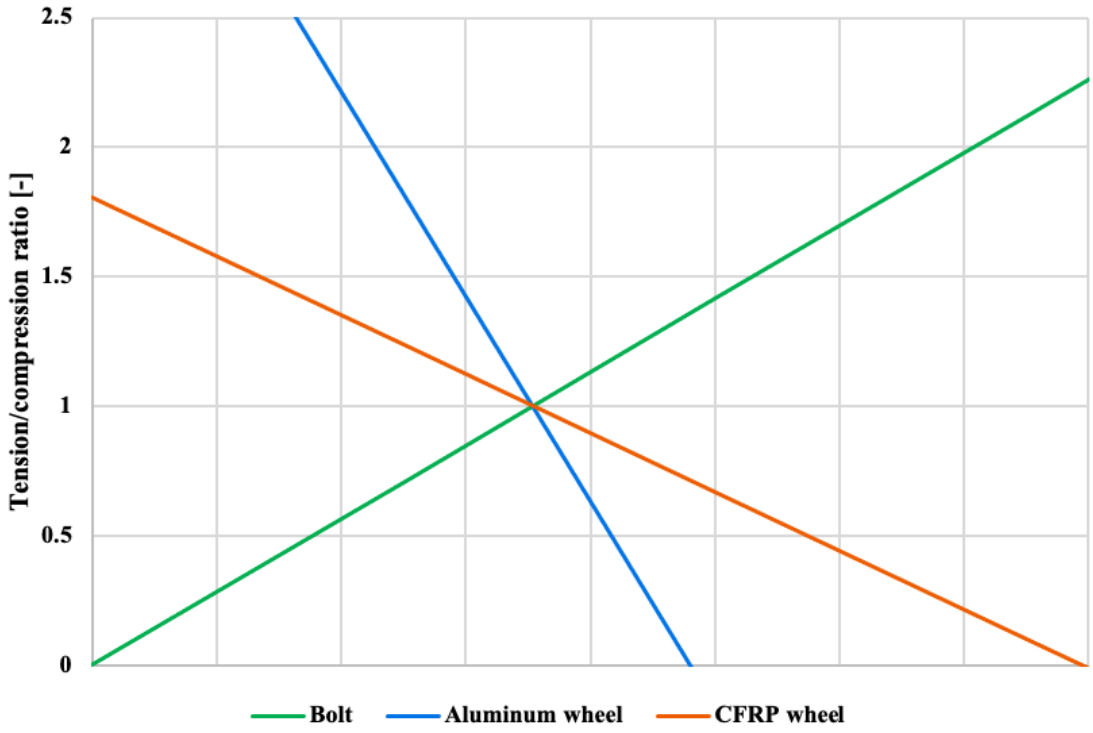

Figure 49: bolt graph: comparison between Aluminium wheel and Composite wheel

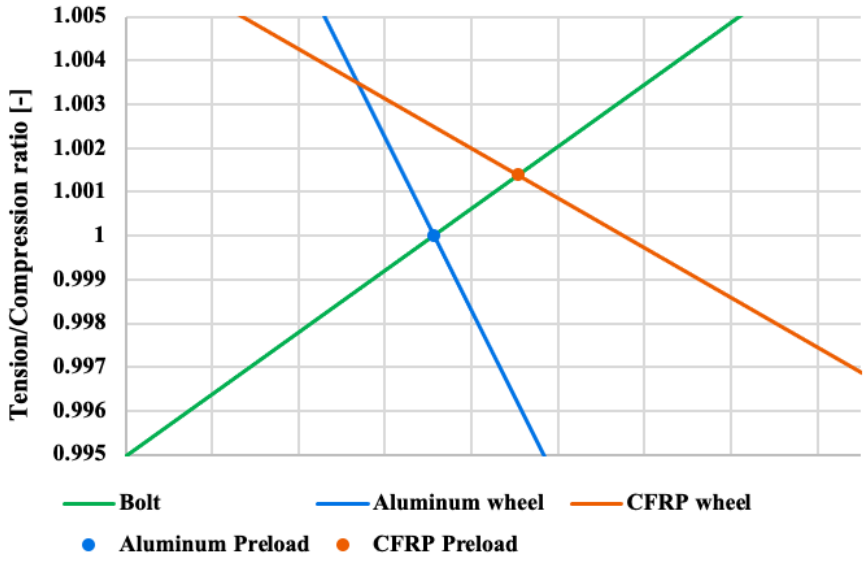

Figure 50: detail about preload for clamped members with Aluminium wheel and Composite wheel

Up to now, it has been spoken only about longitudinal loads. It is interesting to look at cornering manoeuvres, where external loads will increase or decrease the forces acting on the bolt static preload *P*.

During a wheel rotation, depending mainly on lateral load, wheel bolt goes from a minimum to a maximum of tension and the clamped members from a maximum to a minimum of compression. Figure 51 and Figure 52 show a comparison of tension variation versus lateral acceleration at different installation angles (0° is the continuous line and 180° is the dashed line, see Figure 36 for angles reference) between the two different wheels.

Two observations can be made from the graphs: firstly, the outboard wheel experiences more load than the inboard wheel, and secondly, the rear wheel bolt experiences greater load and load variation than the front wheel bolt. In the case of the rear wheel, the amplitude of tension variation for the aluminium wheel is less than the preload *P* value, while for the composite wheel, it is closer to 2 times *P*. This means that the composite wheel is worse from a bolt fatigue point of view. If a high preload is applied to the bolt, fatigue checks should be carried out to avoid any fatigue-related issues.

Proceeding to analyse the bolt graphs in Figure 53 and Figure 54, two observations can be made. There are vertical lines, two blue dashed line referred to front wheel and two bordeaux dash-point line referred to rear bolt. The points at which these lines intersect the stiffness lines of the bolt or clamped members indicate the level of tension for the bolt or the level of compression for the clamped members. In this case, a stiffer clamped member is less desirable, because the high slope of the stiffness quickly causes the compression force to relax or compress more. And the ratio with reference to load variation on the wheel bolt is opposite: on the aluminium wheel it has a little less than 2 times the load variation on composite wheel.

Furthermore, on the aluminium wheel bolt graph, it can also be observed that at maximum loads on the rear bolt, the level of compression of the bolt is almost negative (point “A”). This means that at that rotational instant, the wheel is no longer in contact with the rotor hat. Although this occurs at the external wheel angle of rotation 0°, it is balanced by the other four wheel bolts, for which the compression load applied is higher and up to the maximum (point “B”) at the angle of rotation 180°.

Conversely, a softer clamped member generates more stress variation inside the wheel bolts. The worst-case duty cycle for the 488 Pista titanium wheel bolts is on the rear CFRP wheel, where the load amplitude is twice that of the rear aluminium wheel, as shown in Figure 54 (see point “C” and “D”). This level of load on the wheel bolt is lower than other Ferrari production applications. These vehicles not only generate higher load amplitude values, but also require higher minimum preloads, which need a detailed analysis of the fatigue life of the wheel bolt. The application dealt with here results in coverage of these studies and due to the complexity and length of the discussion they are not specifically reported in this thesis.

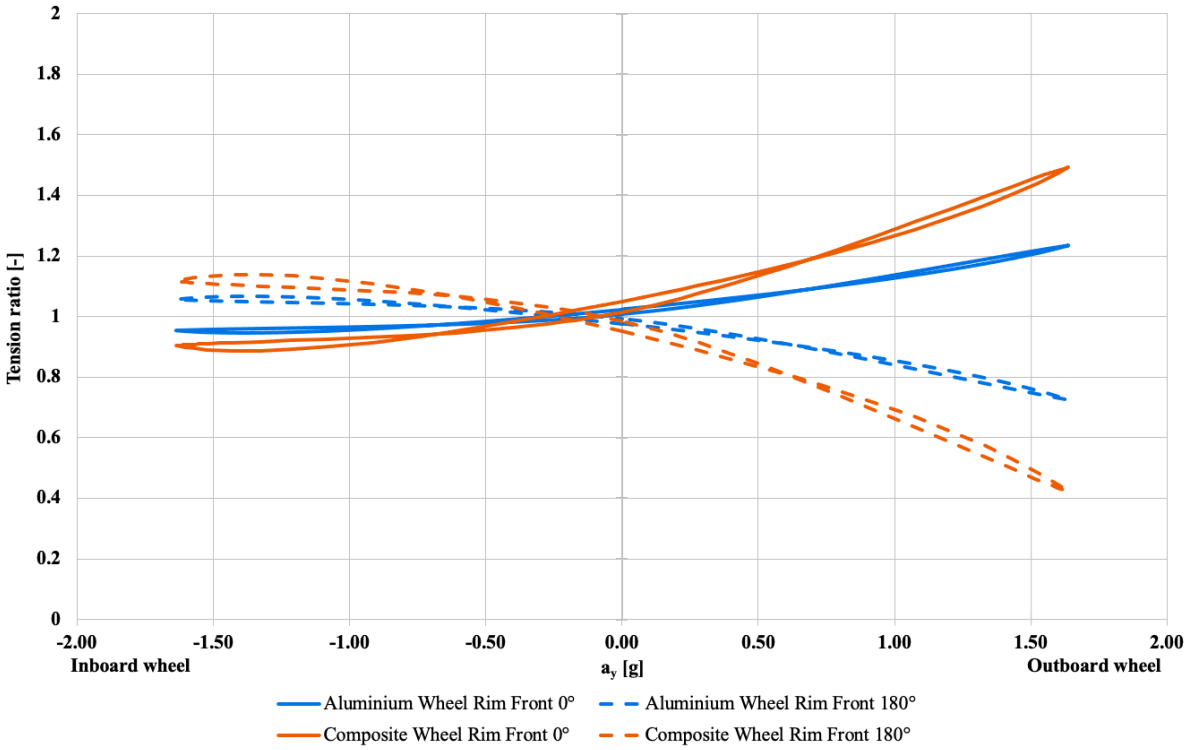

Figure 51: comparison of wheel bolt tension variation between aluminium and composite front wheels as a function of the angle of installation and lateral acceleration

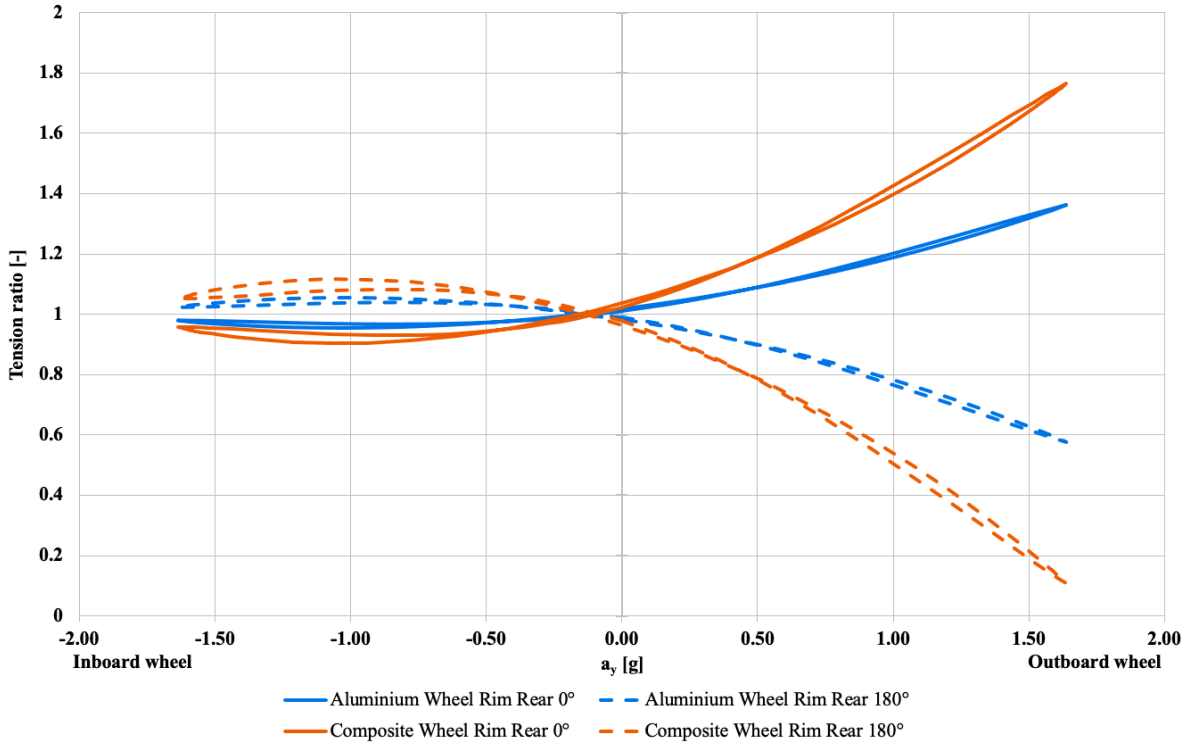

Figure 52: comparison of wheel bolt tension variation between aluminium and composite rear wheels as a function of the angle of installation and lateral acceleration

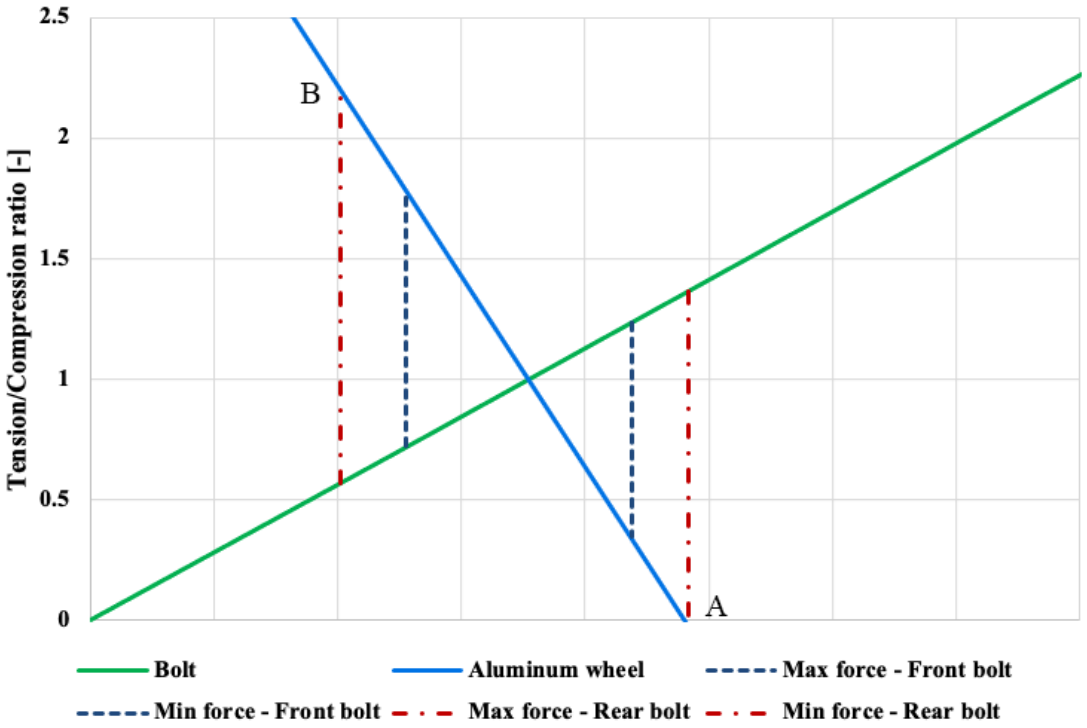

Figure 53: bolt graph for clamped member with aluminium wheel, showing tension and compression forces acting on bolt and clamped members for front and rear wheel

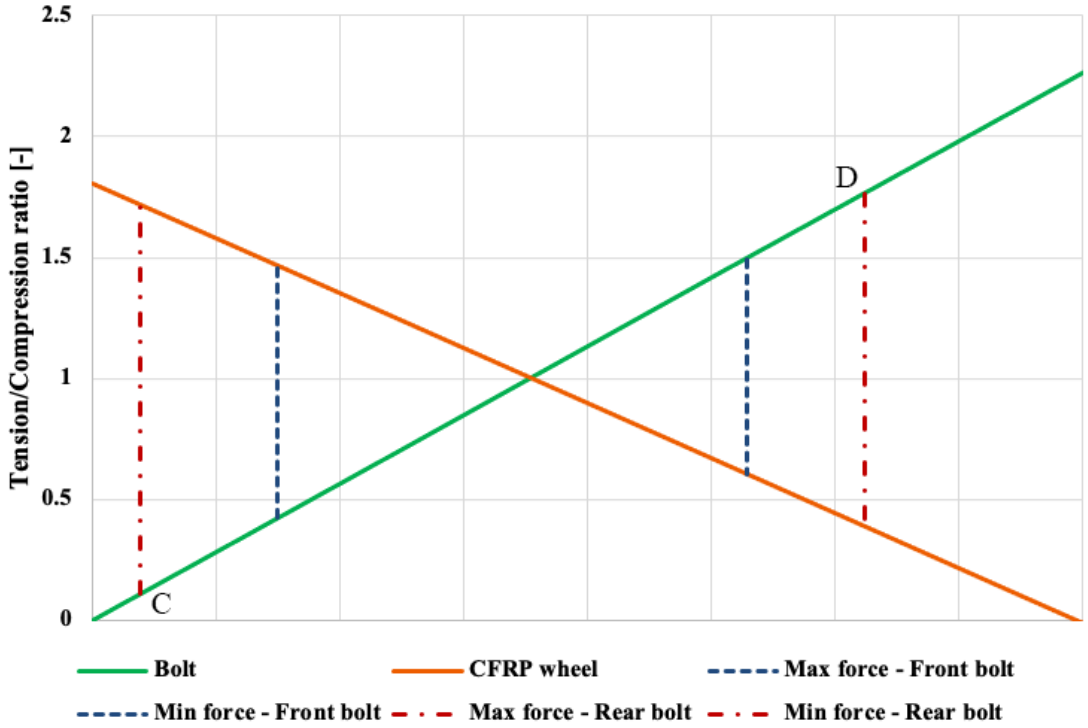

Figure 54: bolt graph for clamped member with composite wheel, showing tension and compression forces acting on bolt and clamped members for front and rear wheel

5.6 From theory to practice

After having determined the minimum preload necessary for the fastening to guarantee the safety of the vehicle, it has been verified experimentally.

The objective of the experimental tests is to verify the appropriate tightening torque chosen to guarantee the minimum tension for the entire life of the car, estimated at least in ten years.

However, to comprehend the effects of thermal creep in the polymeric matrix, a test was conducted to mimic the vehicle's thermal cycle. The rim was heated in an oven to a temperature similar to the hottest encountered in vehicle tests during intensive manoeuvres, and then cooled in air.

Refer to Section *5.1 Wheel assembly overview* for materials and their characteristics involved in the assembly.

To improve the friction coefficient, a dry solid lubricant (Molykote D321R) based on molybdenum disulphide (MoS_2) is interposed between the cones of the screw and the rim, applied directly on the cone seat of the rim, while the hub has a zinc plated thread. Indeed, it is known in the literature that dry tightening with titanium screws present increasingly higher friction coefficient increases tightening after tightening, as can be seen from the tests by Croccolo *et al.* [115] and Kopfer *et al.* [134].

Titanium is therefore famous for having poor tribo-characteristics; however, if it is used in combination with solid lubricants it can work with good results. To limit wear on the surface of the aluminium, Budiski [135] suggests using the solid lubricant MoS_2.

In the following paragraphs, the performances of the bolt tension will be analysed in order: the influence of thermal creep effect on the samples of CFRP wheel, aluminium and composite wheels for 20 tightenings and composite wheel for 10 tightenings with thermal cycles.

5.7 Preliminary thermal test

At the beginning of the project and after the FMEA activity, some features of the wheel were not frozen. This test made it possible to choose the best configuration to limit the creep effect. Thus, it was decided to simulate the tightening of the bolts with small samples.

5.7.1 Samples and procedures

The samples are RTM composite panels fully equivalent to the wheel laminate in the bolt area: same thickness and same fabrics. They are then assembled with the inserts and a support that simulate the backplate but which can accommodate two RTM composite panels with different volume fractions. The evaluated inserts are three, composed of aluminium alloys and different heat treatments: Al6061-T6 (AlMg1SiCu), Al7075-T7351 (AlZn5.5MgCu) and Al7075-T6511 (AlZn5.5MgCu). There are six total configurations in three different holders:

	Backplate 1	*Backplate 2*	*Backplate 3*
	Position 1	**Position 1**	**Position 1**
CF Panel	#743-1 STD VF	#743-2 STD VF	#743-3 STD VF
Inserts	Al6061-T6	Al7075-T7351	Al7075-T6511
	Position 2	**Position 2**	**Position 2**
CF Panel	#745-1 HIGH VF	#745-2 HIGH VF	#745-3 HIGH VF
Inserts	Al6061-T6	Al7075-T7351	Al7075-T6511

Table 14: holder configuration for tightening test

To identify the creep effect, prior to testing, the original thickness of the RTM composite panel was measured at each of the bolt seat mounting locations as follows (see Figure 55):

1. The RTM composite panel was placed on the measurement surface with the backing plate mounting surface in contact with the measurement surface. The measurement surface was defined as *Datum A*,
2. The centre-bore was probed in order to create *Datum B*,
3. The hole of bolt seat position #1 was probed in order to create *Datum C*,
4. For each bolt seat position, a series of measurements were taken at 5 mm intervals between each of the dowel pin holes at a specific PCD using *Datum B* and *Datum C* to locate each of the bolt seat positions. In total there were approximately taken 12 measurement points for each bolt seat position,
5. The Z distance of each measurement point from *Datum A* for each Nut Seat position was calculated and recorded.

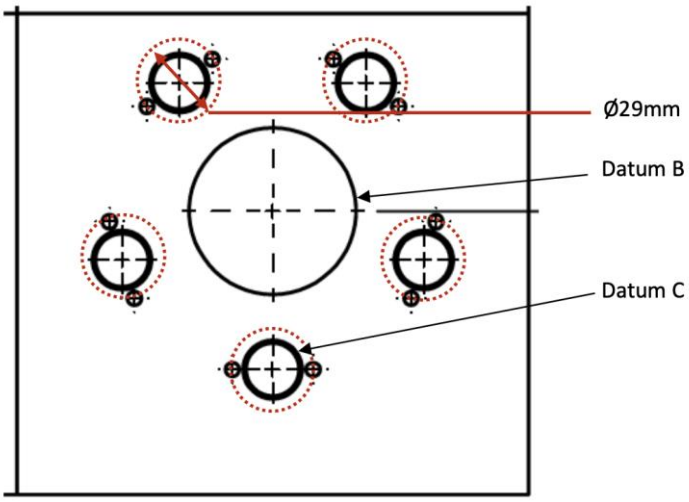

Figure 55: position of the measurements for RTM composite panel thickness around each nut seat position. Datum A is in the direction of the sheet

For each of the set of mounting features, the following procedure was used:

1. The backing plate was assembled within the RTM composite panel by hand,

2. The bolt seat was assembled into the RTM composite panel by hand using a rubber mallet,
3. Hand tightened the titanium bolt,
4. Using the digital torque wrench, the titanium bolt was tightened with a nominal torque of 150 Nm,
5. The length of the titanium bolt was measured using the Olympus Panametrics 25DL ultrasonic thickness gage, recorded and converted to an axial load within the titanium bolt using the force/extension curve previously to the test defined,
6. One thermocouple was placed on upper surface of the RTM composite panel between two of the assembled bolt seats, and the second thermocouple was placed on the rear surface of the RTM composite panel just outside the contact area of the backing plate,
7. The RTM composite panel was placed in the oven and heated and cooled as for Figure 56 below,
8. Once the RTM composite panel had returned to room temperature, the length of each of the titanium bolts was measured using the ultrasonic thickness gage and recorded,
9. The change in length of the titanium bolts was calculated and converted to an axial load,
10. The titanium bolts, PCD plate, bolt seats and backing plate were removed from the RTM composite panel ensuring that the positions of the bolt seats were marked so that they could be reassembled in the same positions,
11. The thickness of the RTM composite panel at the bolt seat locations was re-measured using the same methodology used to generate the original thickness. The change in thickness for each measurement point at each bolt seat position was calculated and the maximum value recorded as the creep effect,
12. The length of each of the titanium bolts was measured using the ultrasonic thickness tester to determine any plastic deformation of the bolts.

Steps 1 – 12 were repeated until a total of four test cycles at elevated temperature had been completed. The process was repeated for each of the six test samples and the results tabulated.

5.7.2 Test results

The thermal test consists in placing the RTM composite panels, at room temperature, in the oven and heat it up to 4.0 °C*[3] over 90 minutes. Then hold samples at target temperature of 4.0 °C* for at least 10 minutes. Reached 10 minutes, cool test samples down to room temperature without aid (e.g. fans, water, etc…) as shown in Figure 56.

[3] for more details on temperature conversion, refer to Section *6.1 Thermal behaviour of composite materials.*

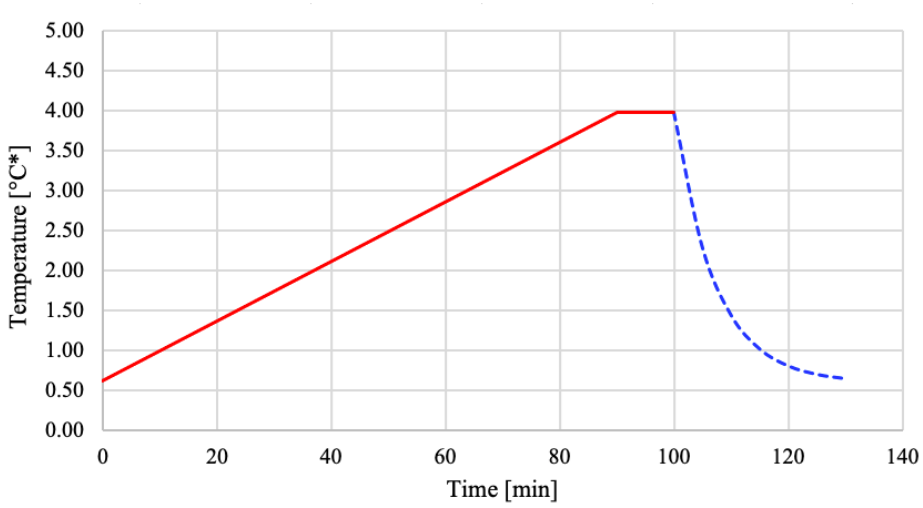

Figure 56: details about thermal cycle

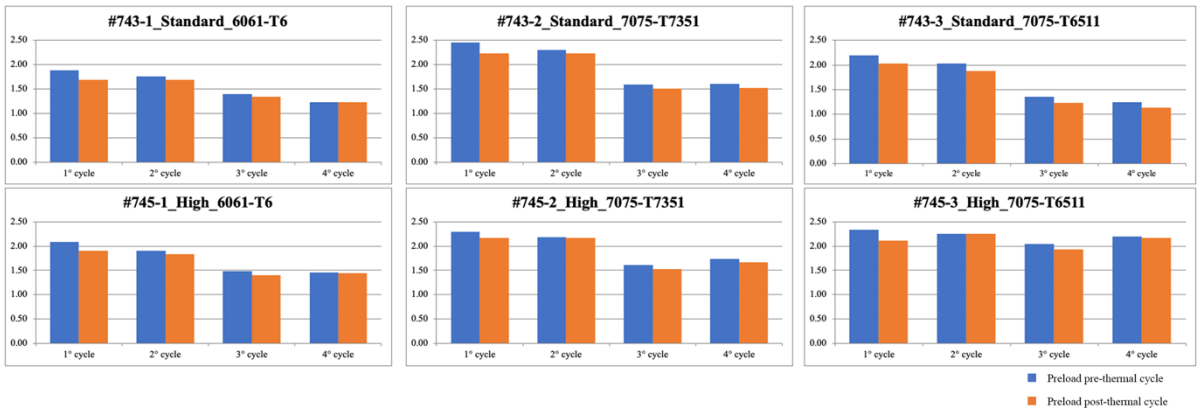

Figure 57: dimensionless pre – post thermal cycle average preloads

By comparing the pre and post thermal cycle readings, the graphs in Figure 57 show the average preload value for each of the thermal cycle compared to the minimum preload required by tightening the aluminium wheel rim. The row containing the three upper graphs refers to the RTM Composite panels with standard volume fraction, on the contrary the lower row refers to the samples with higher volume fraction. In each column instead there is a different type of insert: Al6061-T6 in the first, Al7075-T7351 in the second and Al7075-T6511 in the third.

Upon first tightening, all configurations obtained an average tightening value on the five bolts greater than 2 times the preload required by the aluminium rim, except for the configuration with standard volume fraction and Al6061-T6 insert. The preload value after the first thermal cycle is significantly lower in all cases. If the same comparison is now made by observing the fourth cycle, it can be seen that the preload has effectively stabilized in all cases except for the standard 7075 configuration. Cycle after cycle, the initial tightening value drops for all configurations. This is justified by a reduction in the friction coefficients between the cone of the screw and the insert and the threads of the screw–nut [115]; in any case, it remains higher than the minimum limit required by the vehicle (Table 13).

The breakaway torque during unscrewing was also measured along the test and reported in the table. Using a hand torque wrench, this method measures the torque required to overcome the resistance to anti-unscrewing of the bolt. However, in this test, the absolute percentage value is higher than what the OEM can accept in the final component. After each thermal cycle, no noticeable patterns in the changes of the breakaway torque can be observed, except for the fourth cycle where it decreases for all configurations (Table 15). In the automotive sector, the estimated loosening torque is mainly an indicator of friction in tightening, but the residual tension on the joint also plays a significant role and cannot be disregarded.

In this case, the tightening and untightening formulas specify that:

$$T_R = T_{R_{thread}} + T_{R_{cone}} \tag{24}$$

$$T_L = T_{L_{thread}} + T_{L_{cone}} \tag{25}$$

$$T_{R_{thread}} = \frac{P}{2}\left[d_m \tan\left(\frac{l}{\pi d_m} + \frac{\mu_{thread}}{\cos\alpha}\right)\right] \tag{26}$$

$$T_{R_{cone}} = \frac{P}{\sin\gamma} r_{eff} \mu_{cone} \tag{27}$$

where:

P = preload [N]

d_m = average diameter [m]

l = thread pitch [m]

μ_{thread} = friction coefficient between bolt thread and hub mother-thread

μ_{cone} = friction coefficient between insert and bolt

Tightening torque $T_{R_{thread}}$ is different from loosening torque $T_{L_{thread}}$ as thread during tightening works as "slope" in favour:

$$T_{L_{thread}} = \frac{P}{2}\left[d_m \tan\left(\frac{l}{\pi d_m} - \frac{\mu_{thread}}{\cos\alpha}\right)\right] \tag{28}$$

And this is the only difference between the two formulas as the torque in the conical contact between bolt cone and insert is constant, so:

$$T_{R_{cone}} = T_{L_{cone}} \tag{29}$$

Therefore, based on the available data, it is challenging to determine the impact of each factor on the preload and unscrewing torque, including the friction coefficient of the cone, which can decrease the preload and increase the untightening torque, the friction coefficient of the thread, which can decrease the preload and the unscrewing torque, and the thermal effects.

The objective of the test is to assess the joint embedding, and as such, the main focus is on the preload values obtained before and after the test. Figure 58 presents the percentage of average preload lost for each thermal cycle. The expected behaviour was a significant loss of tension on the screws during the initial cycles, followed by a decrease until stabilization in subsequent cycles. For samples with a high-volume fraction, the first line in the graph shows this trend, which is reasonable since a lower amount of resin in the matrix increases the possibility of its failure under compressive load. The fourth cycle resulted in a loss of less than 4%, while for the other samples, we obtained discordant values ranging from 2% to more than 8%.

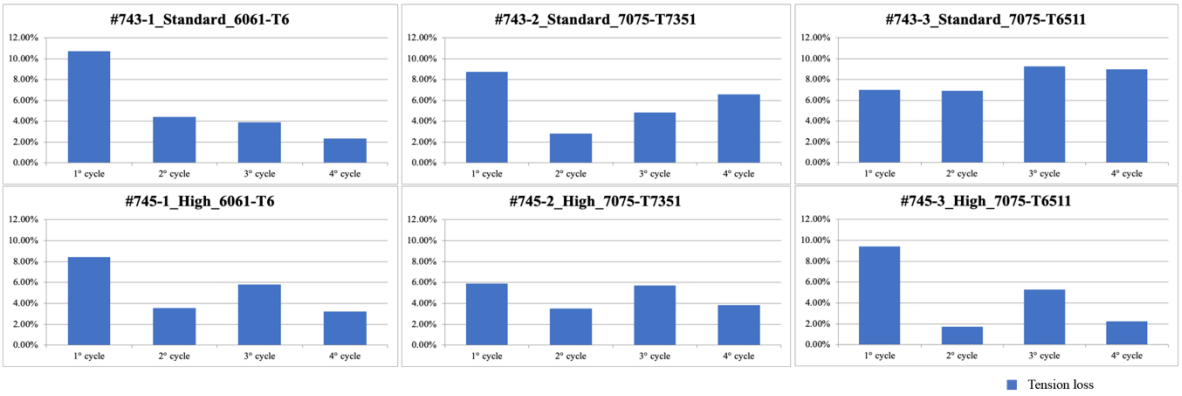

Figure 58: graphs with percentage of clamping force lost every cycle

			#743-1 Standard 6061-T6	#743-2 Standard 7075-T7351	#743-3 Standard 7075-T6511	#745-1 High 6061-T6	#745-2 High 7075-T7351	#745-3 High 7075-T6511
1° cycle	Preload	*Pre-TC [-]*	1.89	2.45	2.19	2.08	2.30	2.34
		Post-TC [-]	1.68	2.23	2.03	1.91	2.16	2.11
		Tension loss [%]	11%	9%	7%	8%	6%	9%
	Unfastening torque	*Post-TC [Nm]*	100.08	107.10	118.72	109.22	96.62	97.24
		Torque loss [%]	33%	29%	21%	27%	36%	35%
2° cycle	Preload	*Pre-TC [-]*	1.75	2.30	2.02	1.90	2.18	2.26
		Post-TC [-]	1.69	2.23	1.88	1.83	2.16	2.26
		Tension loss [%]	4%	3%	7%	4%	4%	2%
	Unfastening torque	*Post-TC [Nm]*	103.66	106.06	126.78	104.98	107.62	108.86
		Torque loss [%]	31%	29%	15%	30%	28%	27%
3° cycle	Preload	*Pre-TC [-]*	1.40	1.59	1.35	1.49	1.62	2.04
		Post-TC [-]	1.34	1.51	1.23	1.40	1.53	1.94
		Tension loss [%]	4%	5%	9%	6%	6%	5%
	Unfastening torque	*Post-TC [Nm]*	88.36	103.20	120.52	91.60	104.04	106.90
		Torque loss [%]	41%	31%	20%	39%	31%	29%
4° cycle	Preload	*Pre-TC [-]*	1.23	1.61	1.25	1.46	1.73	2.19
		Post-TC [-]	1.24	1.52	1.13	1.45	1.66	2.16
		Tension loss [%]	2%	7%	9%	3%	4%	2%
	Unfastening torque	*Post-TC [Nm]*	106.94	107.78	119.92	127.90	128.36	119.34
		Torque loss [%]	29%	28%	20%	15%	14%	20%

Table 15: tightening preload and unfastening torque for each configuration tested

Figure 59 and Figure 60 show similar trends in the thickness reduction of the composite panel with respect to thermal cycles. The panel with standard volume fraction exhibited a higher thickness reduction, with the ones with Al7075 inserts having a variation up to 0.09 mm after the first thermal cycle, and an average of just under 0.02 mm after the fourth cycle. The only exception was the panel with Al6061 inserts, which showed a maximum embedding of 0.04 mm on the first cycle and an average of 0.015 mm on the last cycle.

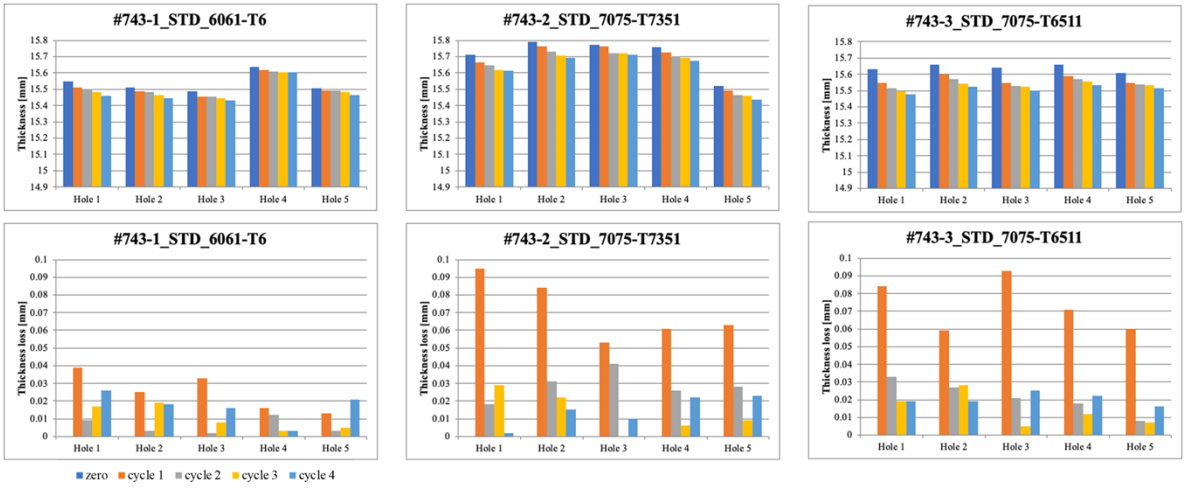

Figure 59: diagrams showing RTM composite panel with Standard Volume Fraction thickness and thickness variation after each thermal cycle for each hole

By contrast, in Figure 60 it can be seen the result of the test for composite panels with high-volume fraction: one sample hole with Al7075 T7351 inserts had a maximum embedment of 0.04 mm; while all the others lost no more than 0.03 mm of thickness, mainly in the first cycle. The average thickness reduction in the fourth cycle is less than 0.015 mm.

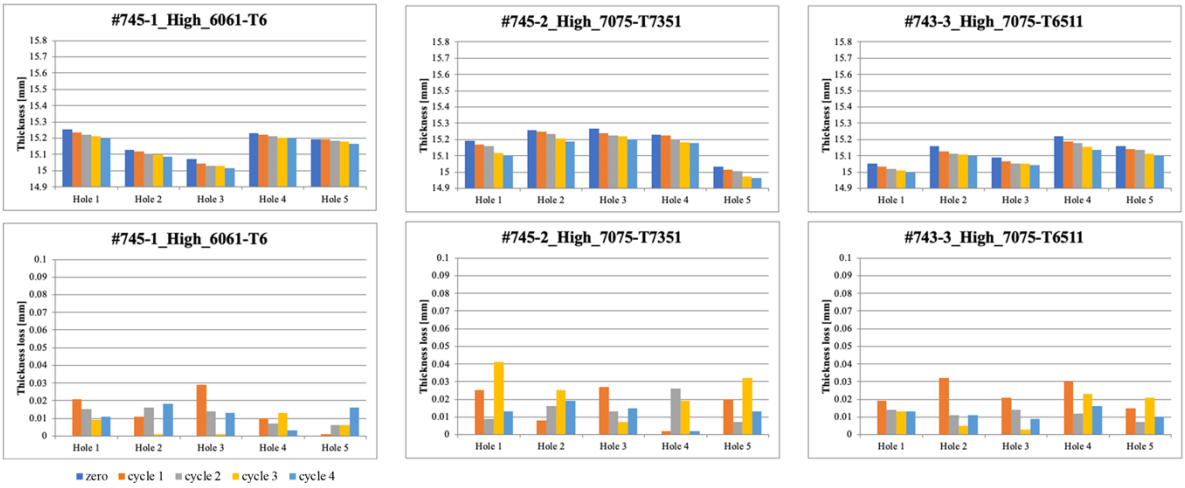

Figure 60: diagrams showing RTM composite panel with High Volume Fraction thickness and thickness variation after each thermal cycle for each hole

However, both samples show evidence of the settling trend in tightening, as predicted by the decrease in tension after the thermal cycle.

Given these results from a creep perspective, the solution that turned out to be superior is the higher volume fraction.

5.8 Bolt tightening validation for CFRP rim and comparison versus aluminium rim

Bench bolt tightening is a static process which tests the continuity of the bolt preload obtained in 20 consecutive tightenings, approximately equivalent to ten years of car usage. The screwing of the components is performed according to OEM standards with final tightening at 120 Nm using a Stanley tightening automatic torque wrench. Then, the tension of the individual bolts is measured with the Olympus Panametrics 25DL ultrasonic thickness gage (Figure 61).

The test bench consists of a structure that horizontally supports an upright complete with wheel hub, brake disc, and brake caliper. The brake disc is hydraulically locked via a pump that applies pressure to the brake caliper to provide anti-rotation torque during tightening.

The following procedure is used:

1. Assemble the wheel rim on the brake disk,
2. Hand-tighten the titanium bolts,
3. On each bolt, write number from "1" to "5" and report the same number on the rim,
4. Starting from the bolt labelled "1", use the digital torque wrench to tighten the bolts in the following steps:
    a) Tighten the bolts in a star order to a pre-torque of 30Nm,
    b) Tighten the bolts in a star order to the nominal torque,
5. Measure the length of the titanium bolt using the Olympus Panametrics 25DL ultrasonic thickness gauge, record it and convert it to an axial load within the titanium bolt using the force/extension curve defined prior to the test,
6. Using the digital torque, untighten the wheel bolts in the same order,
7. Start a new assembly cycle from step 4, this time starting from bolt named "2",
8. Every two cycle, remove the bolts completely from their seats and photograph the seat cone surfaces and bolts surfaces. Ensure that each bolt is placed in its designated seat cone position,
9. At the 20^{th} cycle, besides the photos, measure the length of each of the titanium bolts using the ultrasonic thickness gauge to determine any plastic deformation of the bolts.

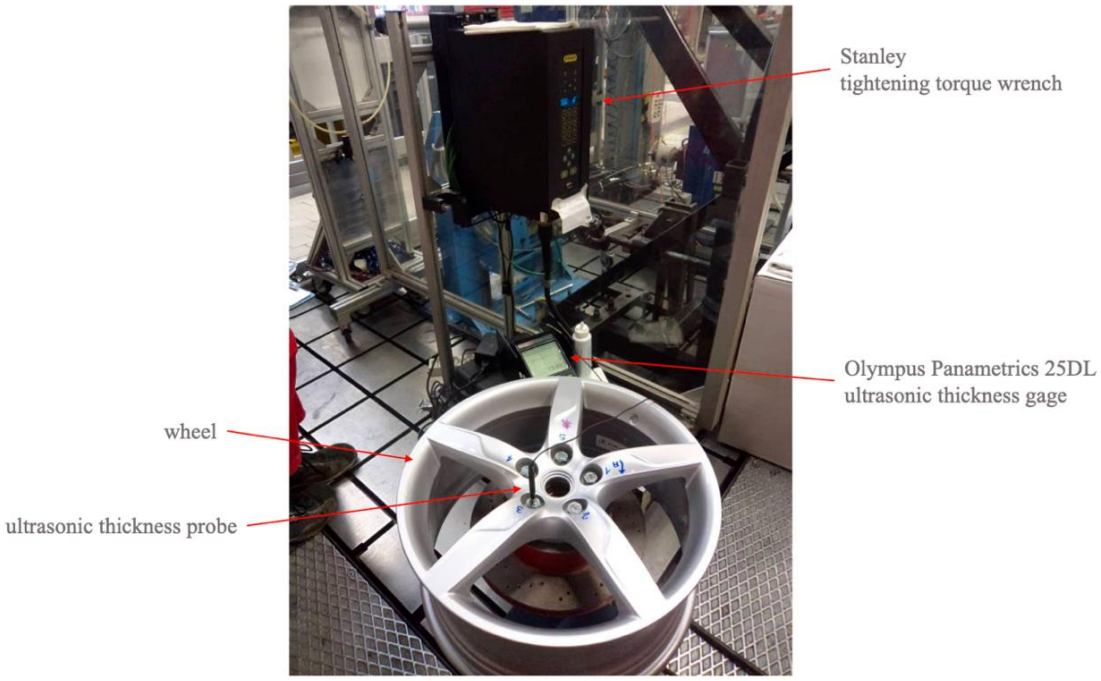

Figure 61: laboratory test bench installation for tightening test – example of test bench

The validation of the aluminium front rim (Figure 62) led to the results in Figure 63: the tension achieved on bolts 1, 4 and 5 remains rather constant, while bolts 2 and 3 have achieved a lower result due to slightly damage on the conical surface of the wheel bolt, as it can be noted in Figure 64.

Figure 62: front aluminium wheel before tightening test

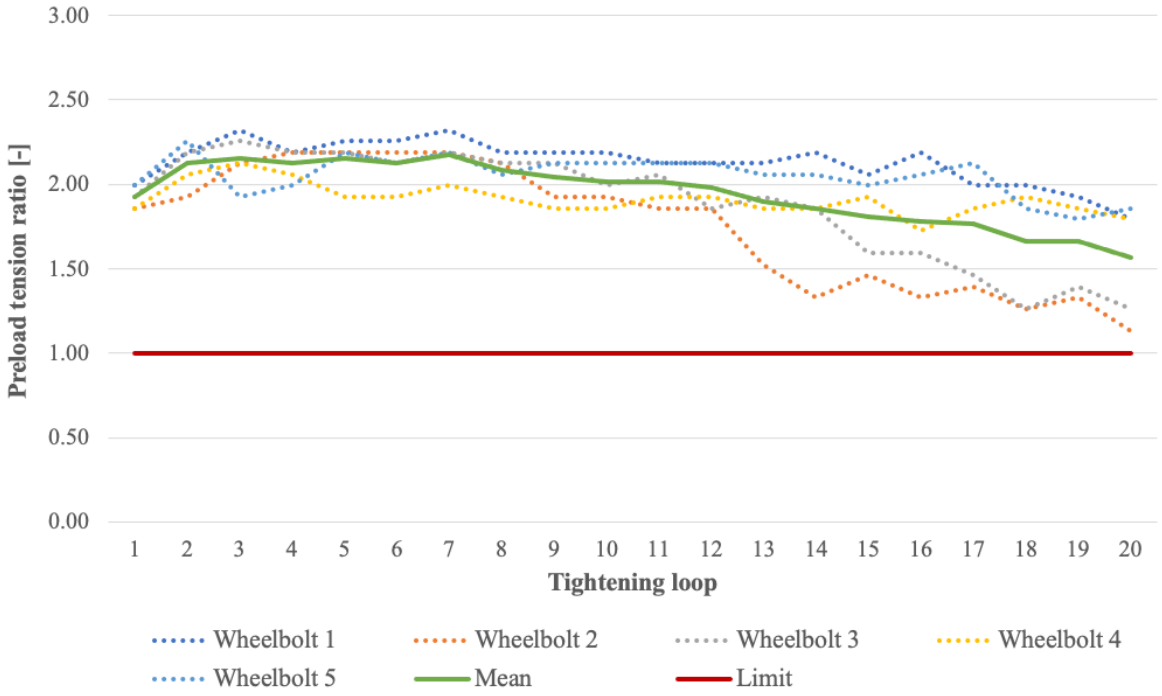

Figure 63: tightening test for front aluminium wheel rim

Figure 64 reveals circumferential marks on the cone of the conical seat of bolts 2 and 3, distinguishing them from the other bolt seats. Meanwhile, Figure 65 depicts the bolts and its surfaces, showing that the Molykote solid lubricant is evenly distributed between the rim seat and the bolt cone. Although a circumferential mark can also be observed on bolt 3 and on bolt 1 (even though the latter did not show tension reductions), the observed variation among the bolts is scattered and can be attributed to various factors, such as the manual application of the Molykote on the cone seat, the zinc plating of the nut, and the tolerances of the cone-on-cone coupling and thread.

Despite this variation, the tightening performance on the aluminium rim achieved an average preload ranging from 1.5 to 2.2 times the minimum preload required, exceeding the threshold limit.

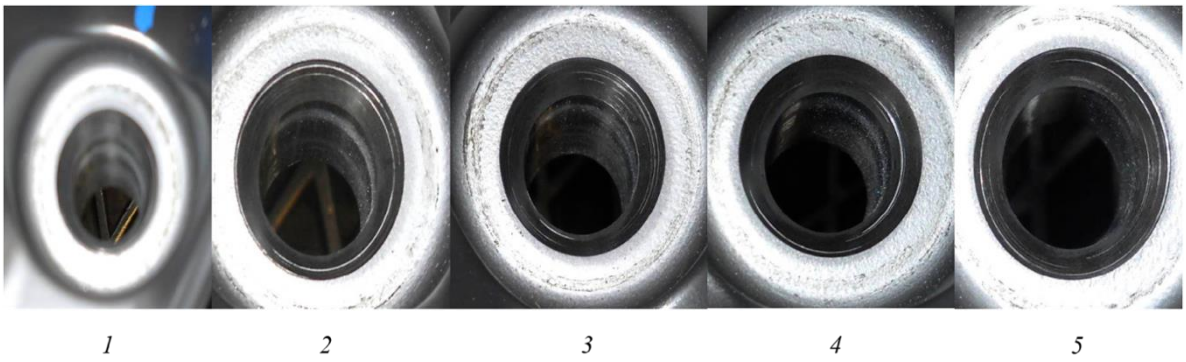

Figure 64: conical surface status of front aluminium wheel after tightening test

Figure 65: conical surface status of wheel bolts after front aluminium wheel tightening test

Previously, it has been seen that the minimum preload required by the composite wheel compared to the aluminium one is only 0.1% higher. However, considering the thermal effects which can lead to a reduction of the static tension by 10% and the historical data from the supplier of the subsequent dynamic tightening settling with a loss of tension equal to another 10%, it was decided to increase the tightening torque from 120 Nm to 150 Nm, with an increase of 25%. This increase should lead to full compensation of the effects of settling, without compromising the tightening.

The first test carried out on the wheel (Figure 66) is the standard bolt tightening up to 20 tightenings. The tightening strategy is completely like the aluminium rim, with the only difference of torque increased to 150Nm.

Figure 67 depicts the graphs of the tightening trend in static conditions for the front wheel. The trend is constant, only the bolt 3 had a trend with a tendency to slightly deteriorate. However, this trend is to be considered acceptable and better than the trend of bolts 2 and 3 for the aluminium front wheel.

Furthermore, the 25% increase in torque raised the average preload value by 25%, demonstrating the fact that, despite the technical differences of the two components tested, the frictions between the two rims are comparable.

Figure 68 and Figure 69 show the conical surfaces of the rim inserts in composite material and its bolts. As in the previous graph, upon careful analysis of Figure 69, it is possible to notice a small circumferential mark on the cone of bolt 3, while the surfaces of the inserts appear to be perfect to the eye. This confirms the reliability of the solution on multiple tightenings.

Figure 66: front CFRP wheel before tightening test

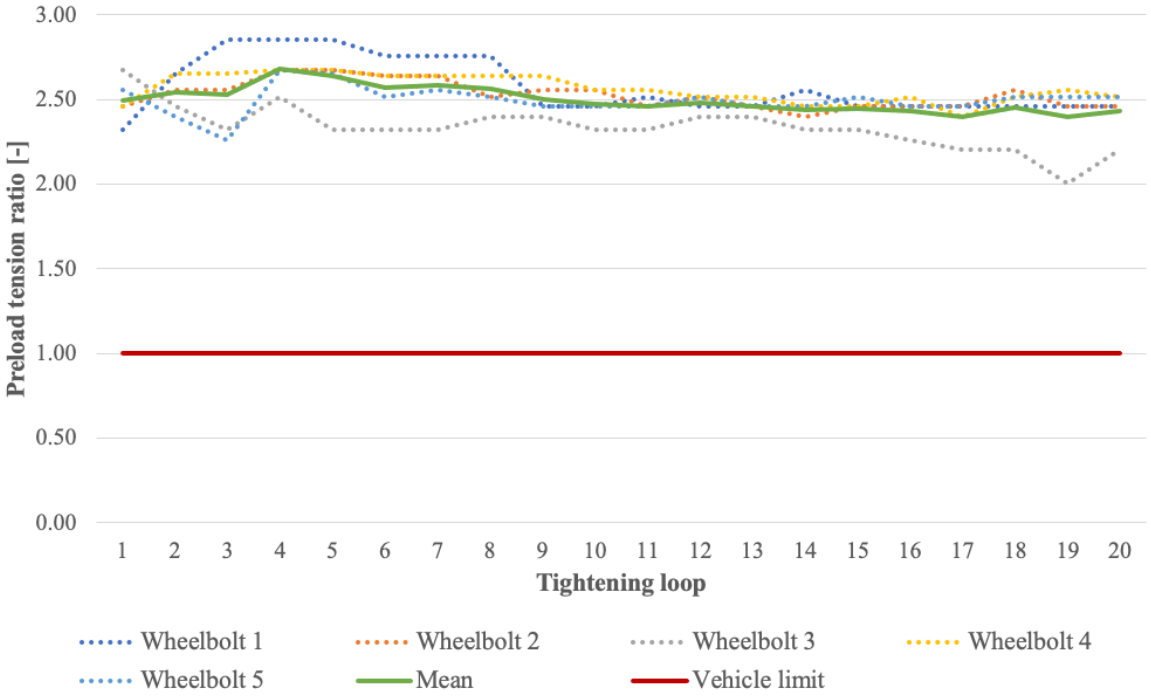

Figure 67: tightening test for front CFRP wheel rim

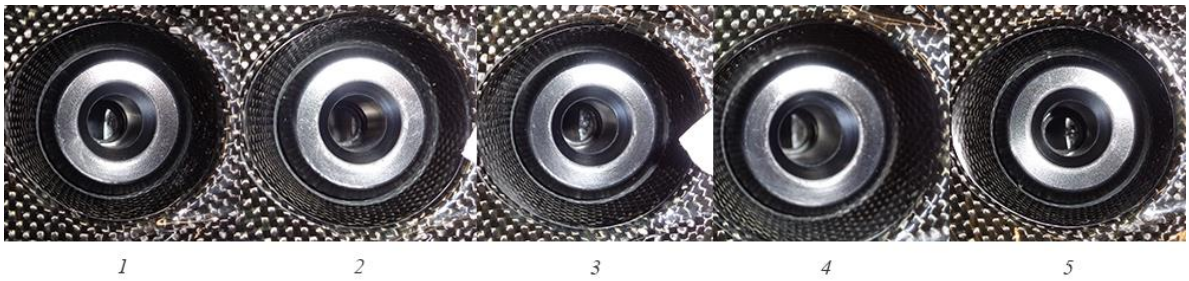

Figure 68: conical surface status of front CFRP wheel after tightening test

Figure 69: conical surface status of wheel bolts after front CFRP wheel tightening test

At this stage of the development and preparatory to the tests in the vehicle, a new test standard only to approve the CFRP rim was developed: 10 tightenings with repetition of the thermal cycle in the oven, the cycle developed for the creep effect test (see Figure 56). Like the previous test on samples, the preload on each screw is measured in two different time steps: after each tightening before the thermal cycle and after the thermal cycle once the ambient temperature has been restored. The aim of this test is twofold: to verify the stability of the tightening under cold conditions and to assess the decay in clamping force due to the thermal creep of the CFRP wheel assembly. The average preload of the five bolts is then evaluated.

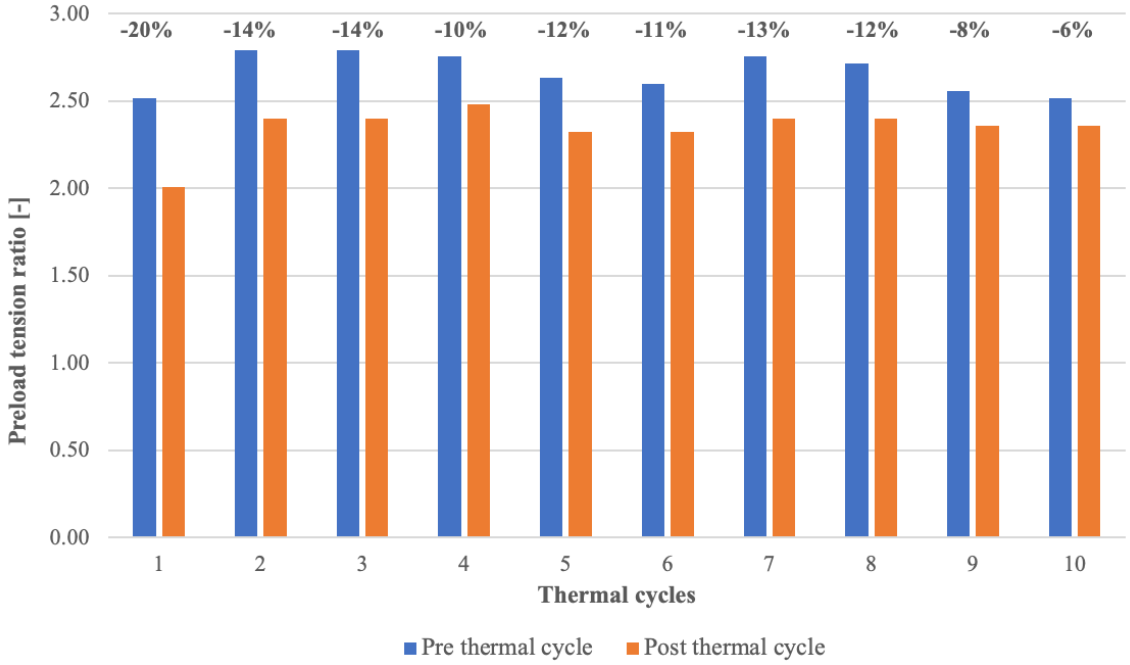

Figure 70: pre and post thermal cycle average preload and percentage decay above each cycle

The result, in Figure 70, shows an expected behaviour as regards the percentage of clamp loss after each thermal cycle. Cycle after cycle, it can be noticed a substantially constant reduction up to a settling, although it shows percentages almost double compared to what was tested on individual laboratory samples (see Figure 58). The first tightening records an average loss of 20%, a value that already drops by 6 percentage points on the second tightening. From the fourth tightening, the value settles around 10% and remains constant until the ninth cycle, where it drops below 10%. The average initial preload is in line with the average of the first 10 tightenings of the previous laboratory test. Furthermore, it is interesting to note that the absolute value of the preload on the bolt after the thermal cycle is substantially the same from the second tightening to the end of the test.

Chapter 6
THERMAL TESTS

6.1 Thermal behaviour of composite materials

The thermal behaviour of the composite matrix is an important characteristic that defines the thermo-mechanical properties of the material [136].

In the FMEA process, this point received the most attention, with a Risk Priority Number of 720. The need for temperature testing during wheel development is new, as aluminium wheels do not require it, since brief exposure to high temperatures close to or above T6 heat treatment aging temperature does not alter the alloy's mechanical properties.

The resin used for the RTM and the wheel is a viscoelastic thermoset polymer based on epoxide groups. The epoxy resin consists of two parts that are cross-linked. These two parts are also indicated with a letter: *"A"* for the epoxy resin and *"B"* for the co-reagent *"hardeners"*. The mix percentage varies according to the type of resin and the characteristics to be obtained [137].

The fundamental characteristic of the composite to be quantified is the Glass Transition Temperature (Tg), a parameter of great interest in the study of amorphous regions in semi-crystalline materials [138]. This temperature can be determined in multiple ways [139], the method used is dynamic mechanical analysis (DMA).

DMA involves the study of the molecular effects due to the relaxation of the polymer subjected to temperature [140], with the aim of determining the mechanical characteristics and the molecular transition as a function of time and temperature. This is made possible by testing specimens to small sinusoidal cyclic strain and measuring the resulting stress response and the phase angle between the two quantities.

These two quantities are respectively called *storage modulus* (curve A in Figure 71) and *tan delta* (curve B in Figure 71). Storage modulus (E') indicates the stiffness as ratio between stress and strain while tan delta ($\tan\delta$) indicates the loss modulus as the out-of-phase between stress and strain.

The storage modulus and the tan delta varies with the increasing of time and temperature in five regions: glass plateau, leathery region, rubbery plateau, elastic of rubbery flow and liquid flow. Tg is the temperature watershed between "*glass*" and "*leather region*" [141,142].

Glass transition temperature has been determined thanks to DMA 800Q from TA Instruments according to international standard ASTM D7028 [143]. For intellectual properties reason, the absolute temperature value cannot be published, so the author

decides to convert all the data accordingly to an arbitrary constant[4]. Testing was performed on a full composite panel (resin, binder and fibre). Figure 72 is a good representation of how the materials will behave in the wheel.

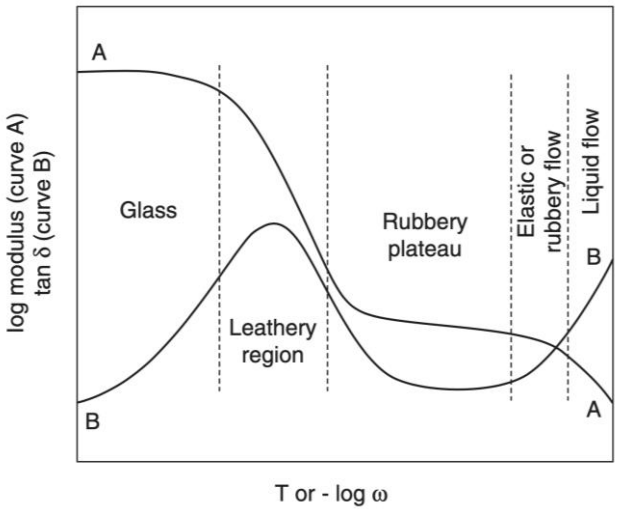

Figure 71: diagram of storage modulus (log modulus, curve A) and damping (tan delta, curve B) characteristics for a linear amorphous polymer with distinct physical states assumed by the polymer at raising temperature from [141]

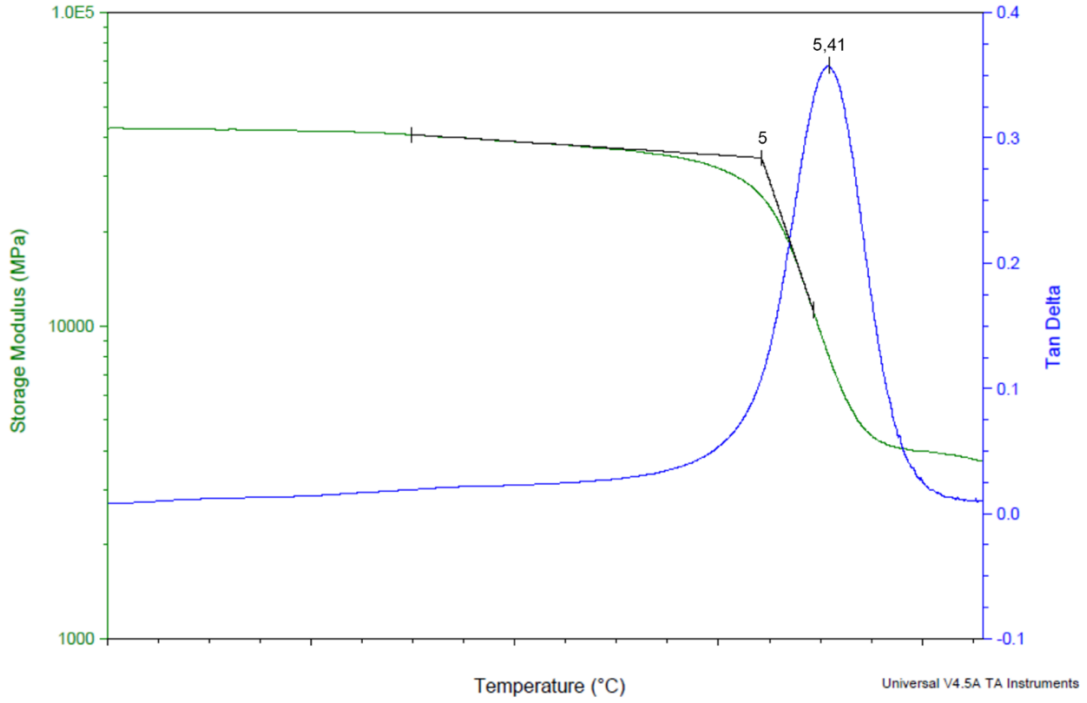

Figure 72: DMA performed on a full composite panel representative of the final product accordingly to ASTM D7028 [143]

[4] All the temperature with °C* in this dissertation are referred to a temperature converted with an arbitrary constant for intellectual properties purpose.

To understand how critical this limit could be, before embarking on this project, some tests were carried out on two different vehicle missions: the italian mountain road "Trento/Bondone" and the Fiorano track (for more details, see Section *6.5 Vehicle tests*). These have been performed on a F12tdf equipped with CFRP aftermarket wheels from the supplier. This vehicle is different from 488, but the only front and rear wheels aftermarket fittable on a Ferrari were these ones. During the test, front brake disk and wheel temperatures were monitored. In Table 16 it can be found the temperatures from the three more important points detected: two were thermal strip applied and one was a thermo-couple installed between brake disk and rim (see Figure 73).

	Temperature points		*Trento/Bondone road*	*Fiorano track*
Dynamic	A	Thermal strip on the spoke-to-hub	<3,7	<3,7
	B	Thermal strip on TBC barrel	<3,7	4.0
	C	Thermo couple between brake disk and wheel	3.7	5.0
Heat-soak	A	Thermal strip on the spoke-to-hub	<3,7	5.0
	B	Thermal strip on TBC barrel	<3,7	5.2
	C	Thermo couple between brake disk and wheel	7.0	9.0

Table 16: temperatures in °C detected on the vehicle missions with F12tdf*

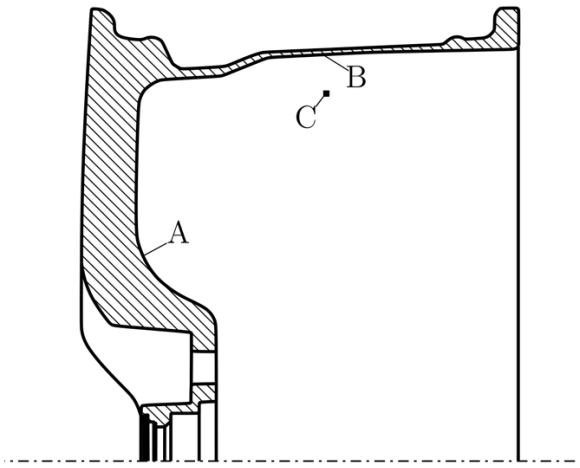

Figure 73: position of thermal strips (A, B) and thermo-couple (C) points detected

The glass transition temperature is below the temperature detected with CFRP aftermarket wheels on the F12tdf, but it did not damage the wheel thanks to the presence of thermal barrier coating. Although this good result, it has been decided to better investigate all the performance of the TBC applied and to optimize it.

6.2 Thermal Barrier Coating via Plasma Spray application

Thermal Barrier Coatings (TBC) are popular for their use in metal-based components subjected to high operating temperature, such as gas turbine and aircraft engines. The credit goes to TBC coatings for making turbines and aircraft engines more performing and efficient, thanks to thermal insulation and protection against corrosion at high temperatures [144,145]. TBC are composed by at least two layers of metal-ceramic materials, a bond coat and a topcoat. The materials commonly used for bond coats are two, MCrAlY (where M is Ni or Co or a mix of both) or Al_2O_3; while topcoat are always a mix of ceramic YSZ or YSZ and $La_2Zr_2O_7$ [144]. Usually MCrAlY is used as a bond layer between the metallic component and top layer YSZ because of its better properties in high oxidation resistance and similar YSZ coefficient of thermal expansion [146,147].

In the last decades, several researcher and engineers tried to apply it to a different substrate material: Fibre Reinforced Polymers (FRP). Kim *et al.*, in their *"Thermal barrier coating for carbon fiber-reinforced composite materials"* [148], presents a bibliography of the state of the art on the application of TBC on FRP. Furthermore, they test CFRP samples with and without TBC protection over a methane gas burner at temperature from 500°C up to 700°C. The CFRP samples were produced in VARTM with a 63.5% of volume fraction and then applied a double layer thermal barrier coating based on aluminium oxide (Al_2O_3) as bond coat and a mix of 30% of potassium silicate (K_2SiO_2) and 70% of distilled water. The results were impressive: at 700°C the surface temperature of samples with TBC were up to 228°C lower than samples without, and the mechanical performance in the first case was reduced only of 50% while in the second case up to 95%. Unlike the metallic components, the reason why on FRP materials is applied Al_2O_3 bond coat instead of more common MCrAlY is explained by Liu *et al.* [149] and Wang *et al.* [150] and lies in the fact that Ni or Co have got a high melting point, i.e. about 1450°C, and its deposition will likely damage the CFRP substrate.

The wheel supplier understood the efficacy of thermal barrier coatings in advance and in 2015 patented a method to apply it on the CFRP wheel [151]. For the Ferrari wheel, he proposed a triple layer metallic-ceramic-metallic thermal barrier coating with bond and top coats made of aluminium oxide (Al_2O_3) and a middle coat of yttria stabilized zirconia (7-8% YSZ). According to his experiment, like the ones done from Kim *et al.* [148], the temperature on FRP should be reduced up to 2,5°C* as in Figure 75. The experiment has been performed in a thermal exposure rig similar to the schematic one in Figure 74, where two CFRP samples, one with TBC application and one without, are hit by radiations generated from a infrared lamp and heat from the hot wind thanks to a fan placed under the lamp.

The promised results bring the temperature of the composite within the limits set in the wheel product sheet. Unlike Kim *et al.*, the third layer is added to help increase the reflectivity of the ceramic surface, improving its resistance to brake disk radiation.

This triple layers thermal barrier coating is applied with Air Plasma Spray (APS) technology on the back of the spokes and on the rim barrel. Accordingly with Sens *et al.* [151], the TBC is applied with the following manufacturing cycle:

1) Surface treatment of thermal exposure area with grit blaster to abrade the resin layer,
2) Pre-heating of composite component,
3) Metallic bonding layer thermally sprayed onto abraded resin layer,
4) Ceramic thermal protection layer thermally sprayed onto bonding surface,
5) Metallic bonding layer thermally sprayed onto middle surface.

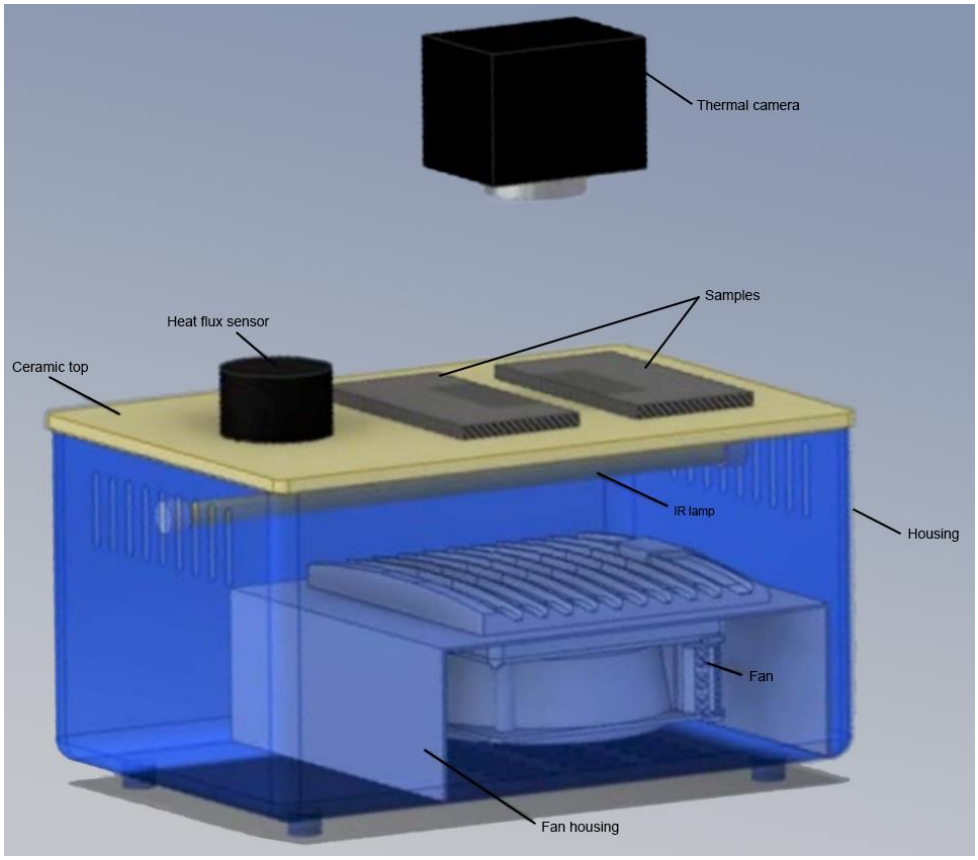

Figure 74: scheme of the thermal exposure rig

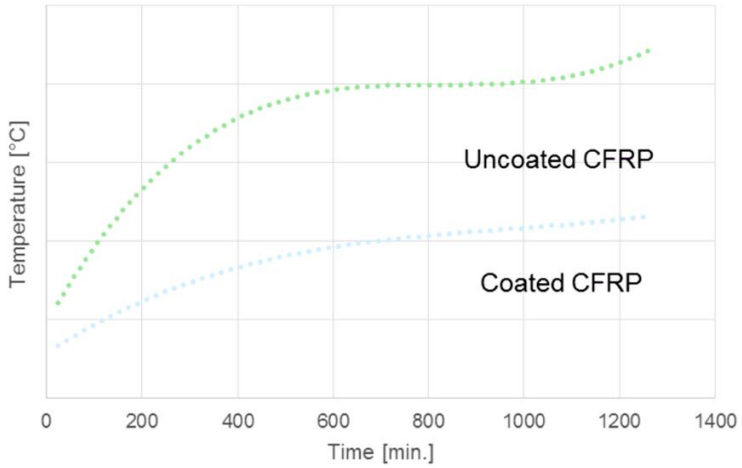

Figure 75: typical thermal exposure results of uncoated CFRP sample compared with coated sample

On the different part of the wheel, thickness in Figure 76 are achieved. Thickness ranges from a minimum of 300 µm to a maximum of 450 µm overall.

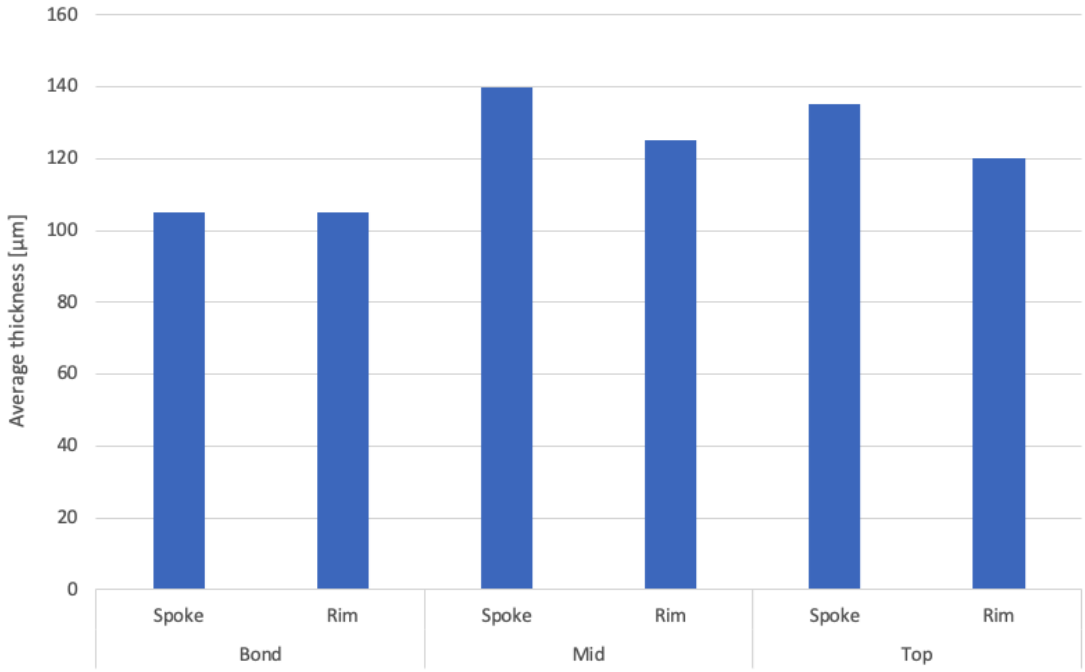

Figure 76: average TBC thickness per layer achieved on the CFRP wheel

According to the experiment done by Abedi *et al.* [147], the bond coat thickness should be around 100 µm to guarantee high strength adhesion and YSZ mid coat should be less than 300 µm to not crack due to high level of residual stresses produced during YSZ deposition.

The supplier has tested the adhesion according to ASTM D4541-17 [152].

From the bibliography made by Boccarusso *et al.* [153], the main failures of the TBCs from the substrate or from the bond coat can be oxidative and thermal fatigue type due to the residual stresses induced by the different coefficients of thermal expansion; but this is mainly valid for metals subject to high temperatures such as turbine blades. Since this is an application on a wheel, mainly subject to thermo-mechanical fatigue and living in an environment that is often humid, salty, or exposed to atmospheric agents, the mainly issues to be verified concern the actual increase in thermal capacity on the wheel and resistance to environmental tests, in particular the salt spray corrosion test.

In the following paragraphs, the tests and the validation done by the vehicle manufacturer to certify the safety of the wheel for a high demanding application like a Ferrari vehicle will be proposed. It consists in two activities, the first developed on a specific test rig in laboratory followed by vehicle tests.

6.3 Thermal laboratory test

From the preliminary activity carried out on the supplier's aftermarket wheels, the limit of 5.2°C* was found, higher than the Tg of the resin. Despite this, a single heatstroke did not damage the wheel, but what if this were repeated several times in the life of the component?

The laboratory test aims to repeatedly simulate the behavior of a heat stroke on a rim with tyre fitted. The Vehicle Reliability Department has estimated that in the life of a Ferrari sports car, up to 50 heat soaks could be generated in the same rim sector. Therefore, the target of the test is 50 heatstroke cycles, at a temperature equal to the Tg of the rim measured on the thermal barrier coating of the barrel.

The bench setup consisted in two industrial thermal guns controlled by a PLC that simulate the heat coming from the braking system and a series of aluminium shields to heat the rim barrel only in one area of interest (and always in the same area, see Figure 77). The industrial thermal guns were positioned at the same distance between the brake disk and the rim barrel.

(a) *(b)*

Figure 77: bench setup for heat soak test

The measuring tools were installed:

1) From the valve, real-time tyre pressure monitoring system (Figure 78a),
2) One thermocouple on the TBC, brake disk side (Figure 78b),
3) Two thermocouples on the barrel, tyre side (Figure 78c)

(a)

(b)

(c)

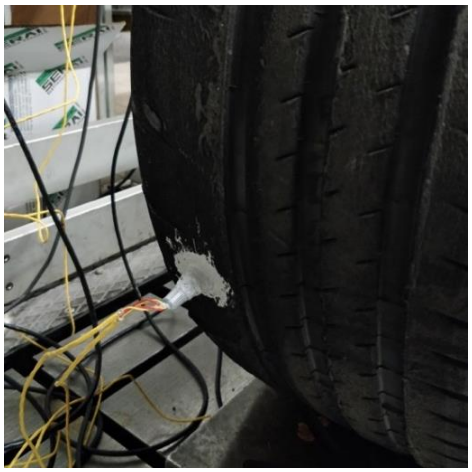

(d)

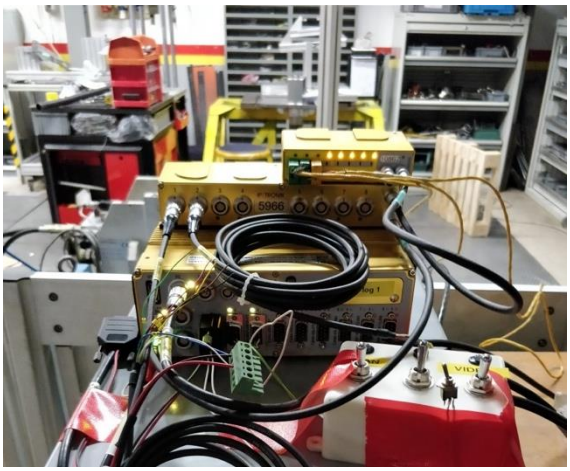

(e)

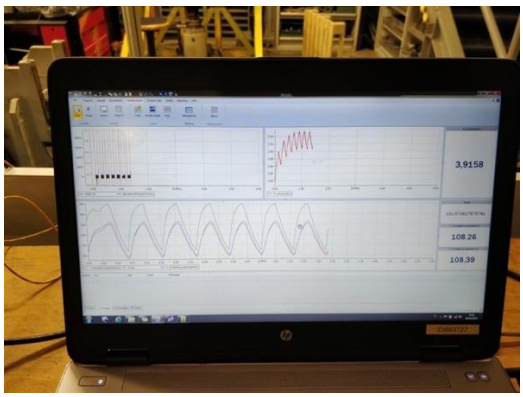

(f)

Figure 78: measuring and electronics tools for heat soak test

To allow the installation of thermocouples on the barrel, tyre side, a hole in the tyre for the wiring has needed (Figure 78d) then sealed not to lose air. The PLC system was connected to the computer and constantly monitor the thermocouples and tyre pressure sensors, turning off and on automatically the thermal guns (Figure 78e-f), simulating the cycles.

The test was conducted at a nominal hot pressure at 3bar, to generate more stress on the barrel. The pressure was controlled by an inflation valve before the pressure sensor.

6.4 Thermal laboratory results and discussion

The test was performed with success, 50 thermal cycles have been completed without damaging the wheel.

In Figure 79, the details about the digital control of the heat guns is presented:

- below 2.7°C*, the heat guns are turned on,
- when 5.0°C* is reached on the barrel, TBC side, the heat guns are turned off. This temperature is the temperature limit.

This cycle was repeated 50 times.

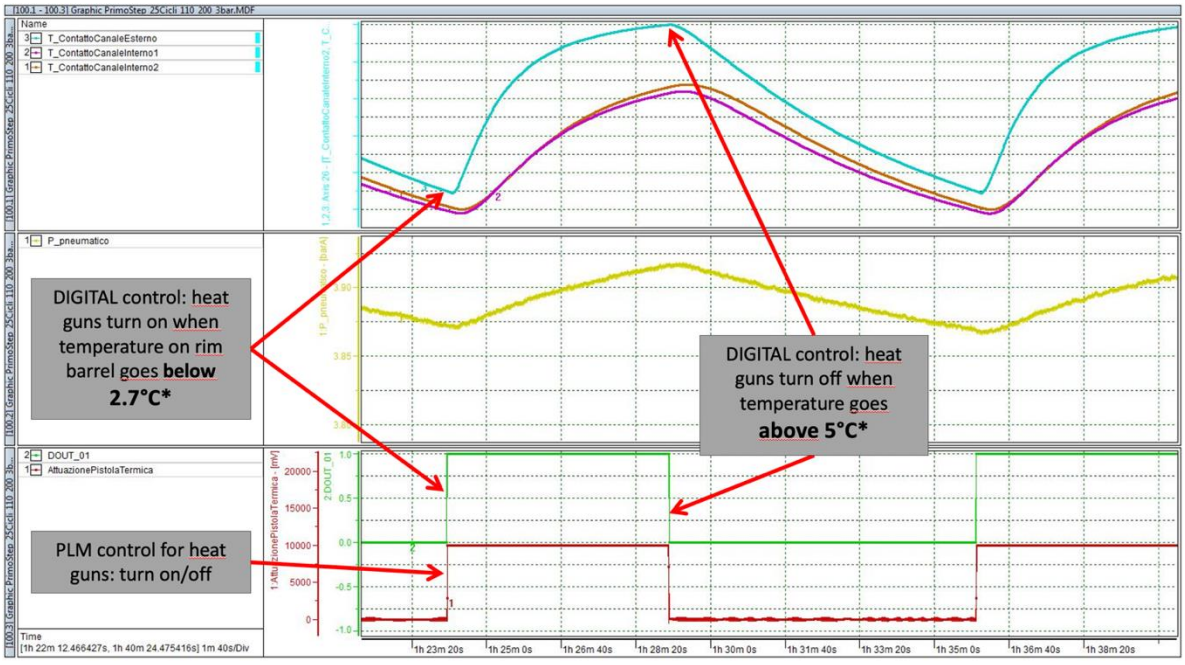

Figure 79: first thermal soak cycle with details about the rig functionality

In addition, Figure 79 presents the real performance of the thermal barrier coating on the wheel for each cycle: when the temperature on the rim barrel is 5.0°C*, on the other side is 4.1°C*. This is just -0.9°C*, not exactly the 2.5°C* expected from the supplier laboratory test. When cooled down, temperature on the TBC side went to the target expected of 2.7°C*, while the temperature on the tyre side went to 2.5°C*, -0,2°C* compared to TBC side. Furthermore, yellow line represents the tyre pressure variation: this was the first

parameter observed to understand if something is going wrong. The pressure had a normal behaviour where increase when heated and decrease when cooled, always between 2.7 and 3.0 bar. In Table 17 for each cycle, the details about temperature and time at each temperature step are summarized.

	Rim TBC side	*Rim tyre side*
Cycle start[°C*]	2.7	2.5
Cycle end [°C*]	5.0	4.1
Tyre pressure	Between 2.7 – 3.0 bar	
Rising time	4'50''	
Descending time	6'45''	
Time @ T>4.5 [°C*]	4'16''	-
Time @ T>4.7 [°C*]	2'55''	-
Time @ T>5.0 [°C*]	-	-

Table 17: analysis of one heat soak cycle: details about temperature and time reached on rim barrel, TBC side or tyre side

Each cycle took 4 minutes and 50 seconds to reach the temperature limit, then took 6 minutes and 45 seconds to cool down to 2.7°C*. This leaded the wheel to be subjected to a temperature higher than 4.5°C* for about 4 minutes and higher than 4.7°C* for about 3 minutes.

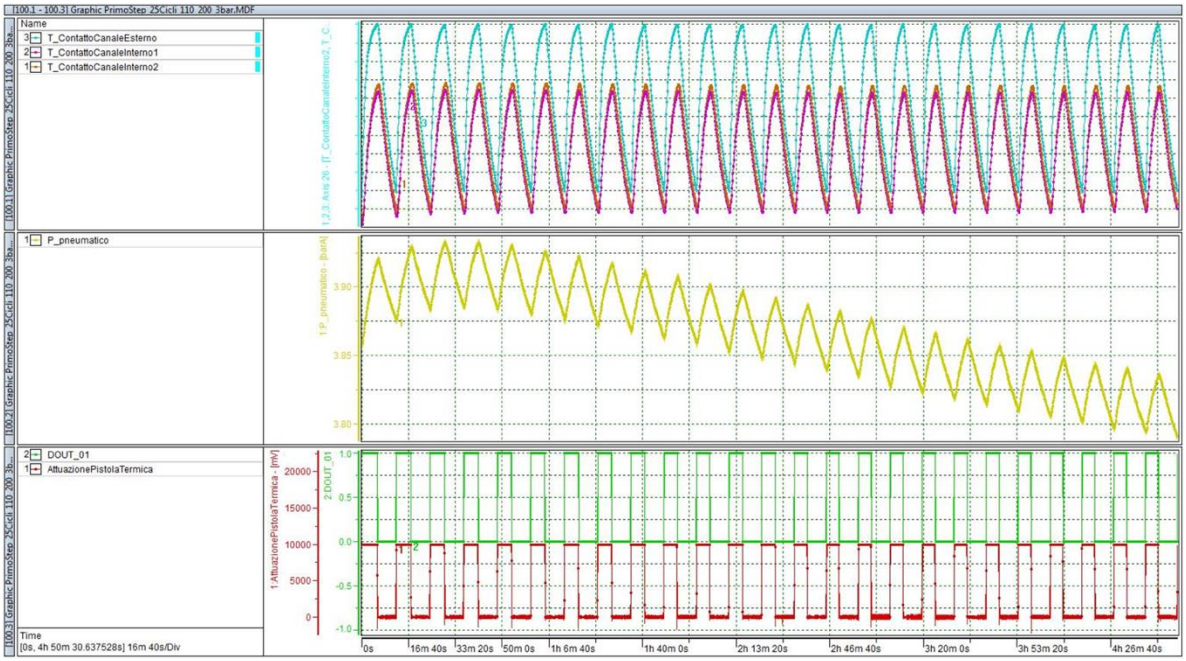

Figure 80: temperature and pressure behavior of last 25 heat soak cycles

In Figure 80 it is reported the last 25 cycles of heat soak. Tyre pressure had a downward trend, but this has been considered physiological and probably caused from some air leaked from the tyre hole sealed. Overall times at temperature above 4.5°C*, 4.7°C* and 5.0°C* are presented in Table 18.

T: 2.7 - 5.0 °C* 50 cycles	***Rim TBC side***	***Rim tyre side***
Time @ T>4.5 [°C*]	3h 55′ 20′′	-
Time @ T>4.7 [°C*]	2h 25′ 50′′	-
Time @ T>5.0 [°C*]	-	-

Table 18: overall times at temperatures >4.5, 4.7, 5.0°C for 50 cycles with temperature limit of 5.0°C**

Because the test at the Tg went well, we have decided to find the real limit achievable on a laboratory test rig; thus on the same wheel we increase the temperature limit to 5.2°C*, the same temperature read from the F12tdf vehicle test.

Each cycle now pushes the wheel above the Tg, at least on the thermal barrier coating. Indeed, in Table 19 there are temperature and timing analysis, as for previous test, for one cycle: starting point was always 2.7°C* for temperature on TBC side and surprisingly also on the tyre side too; when temperature limit was reached on TBC side, on tyre side the temperature raised up to 4.9°C*. This means that CFRP is probably at or close to the Tg.

	Rim TBC side	***Rim tyre side***
Cycle start [°C*]	2.7	2.7
Cycle end [°C*]	5.2	4.9
Tyre pressure	Between 2.7 - 3.0 bar	
Rising time	5′45′′	
Descending time	6′55′′	
Time @ T>4.5 [°C*]	5′06′′	3′30′′
Time @ T>4.7 [°C*]	4′00′′	1′26′′
Time @ T>5.0 [°C*]	2′35′′	-

*Table 19: analysis of one heat soak cycle: details about temperature and time reached on rim barrel, TBC side or tyre side, with temperature limit of 5.2°C**

The test continued until the 12th cycle, when the softened matrix of the composite was no longer able to contain the pressure of the tyre which stressed the barrel, irreparably damaging the composite, fracturing the TBC which then detached and curled up on the rim, thus allowing the pressure to flow out and the tyre to deflate (Figure 81, red cycle on yellow line). On the temperature instead, the peak of the blue line red circled in Figure 81 correspond at the instant when thermocouple detached from the wheel.

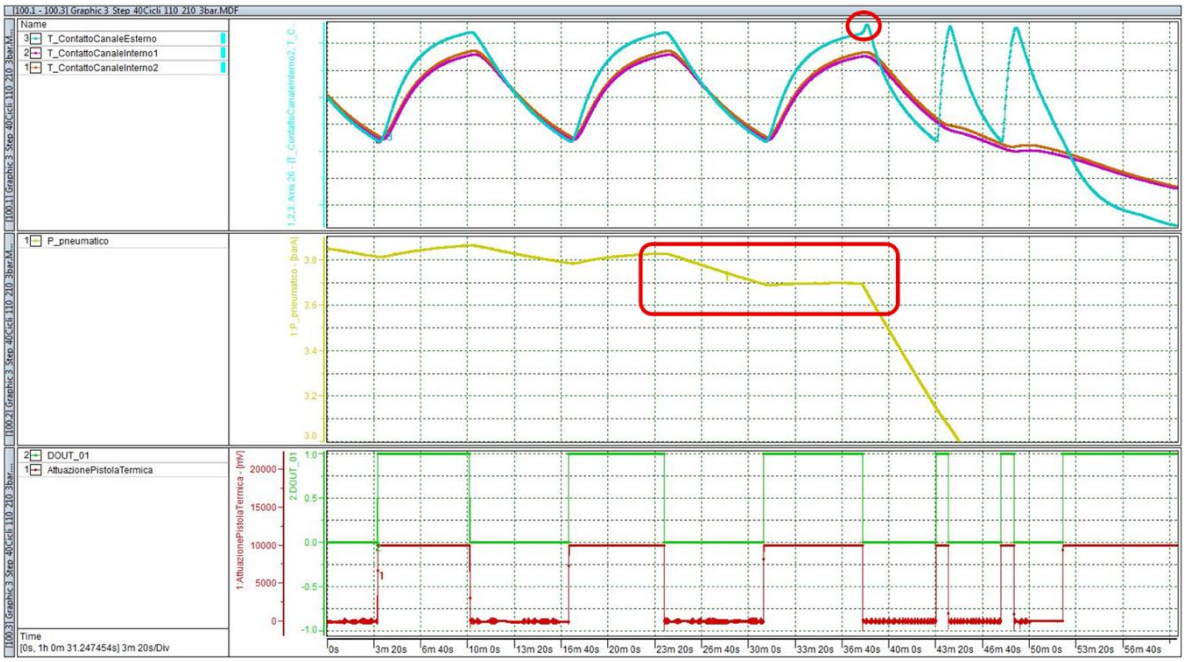

Figure 81: detail about 12th cycle at temperature limit of 5.2°C: red circled the moment of the failure*

(a) *(b)*

Figure 82: damage occurred to the wheel: (a) back view, (b) rim view from TBC side

In Figure 82a, b it is possible to see the visual damage.

Overall, the wheel lasted 33 minutes before collapsing at a temperature above the Tg (Table 20).

T: 2.7 - 5.2 °C* 12 cycles	***Rim TBC side***	***Rim tyre side***
Time @ T>4.5 [°C*]	1h 1′ 02′′	42′ 00′′
Time @ T>4.7 [°C*]	48′ 00′′	17′ 12′′
Time @ T>5.0 [°C*]	33′ 00′′	-

Table 20: overall time at temperatures >4.5, 4.7, 5.0°C for 12 cycles with temperature limit of 5.2°C**

6.5 Vehicle tests

Thanks to the heatstroke laboratory tests, the wheel limit during a heat soak has been found. Even if the results from F12tdf test with aftermarket wheels highlighted the critical issue on the heat soak, the back of the spoke remained a question point, clarified with vehicle tests.

The purpose of the tests in the vehicle was to subject the components to high thermal stress, representative of both road and sporting use from a demanding customer perspective, through targeted tests, with the aim of collecting information on the maximum temperatures reached and their trend during the tests, through dedicated sensors. The first aspect had the aim of demonstrating that the limit temperatures are below the Tg of the component, the second instead was aimed at the building of a thermal model for the wheel.

Thanks to the collaboration with the Ferrari F1 Racing Department, a specific instrumentation was developed. Two special TPMS sensors were installed on the front left wheel with appropriate reinforcements and bondings, each connected to four thermocouples. These were arranged on the rim barrel at constant angular intervals both on the tyre side (internal, see Figure 83a, b) and on the TBC side (external, see Figure 83 d, e). One of the four external thermocouples has been connected on top of the spoke (see Figure 83c).

This arrangement made it possible to study the dynamic thermal load during the various tests performed and to investigate the effects of heat stroke on the barrel. The diagram installation of the sensors is represented on Figure 83b, d.

The vehicle missions chosen to monitor the temperatures were the *"Alpine downhill"* of the Trento – Bondone road (Figure 84), which with its average gradient of 6.7% is able to put the braking system under stress in a road perspective and the Fiorano track in a sporty perspective, famous circuit for its very demanding on the braking system (Figure 85).

The *"Alpine downhill"* was carried out on a sunny day, with temperatures between 11°C in Bondone and 18°C in Trento. Table 21 shows the descent times.

	Customer driving	***Max performance***	***F12tdf reference***
Time	19' 23''	15' 06''	17' 25''
Avg. speed [km/h]	52.0	67.5	63.3

Table 21: time and average speed Trento - Bondone downhill

At the end of the downhill, the vehicle was immediately stopped in a square to simulate the heatstroke.

(a)

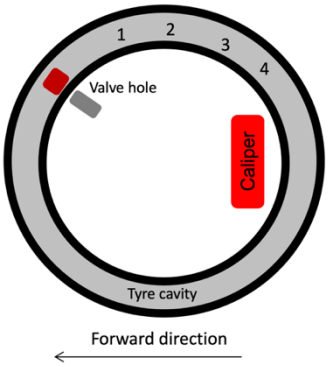

(b)

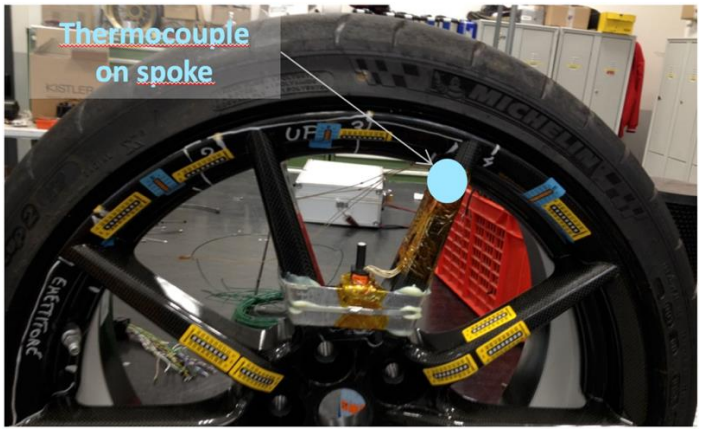

(c)

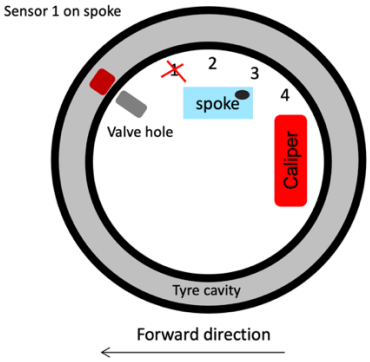

(d)

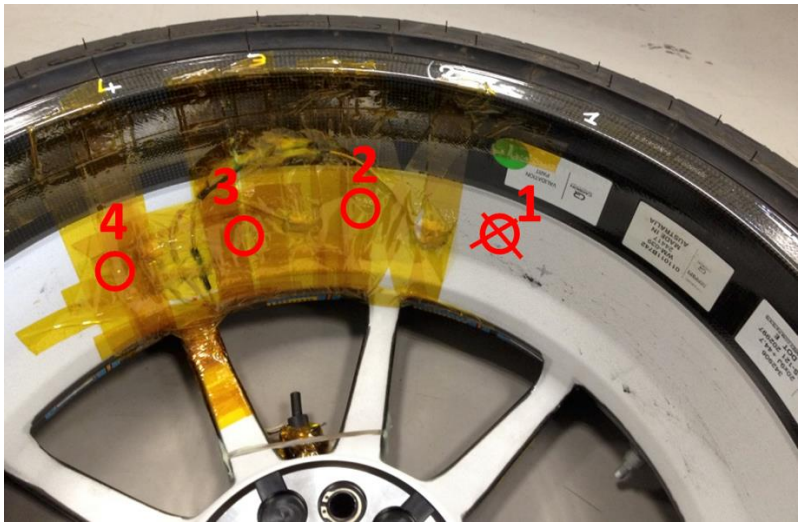

(e)

Figure 83: positioning of the thermocouples on the front left wheel: (a), (c), (e) thermocouples, (b), (d) installation diagram

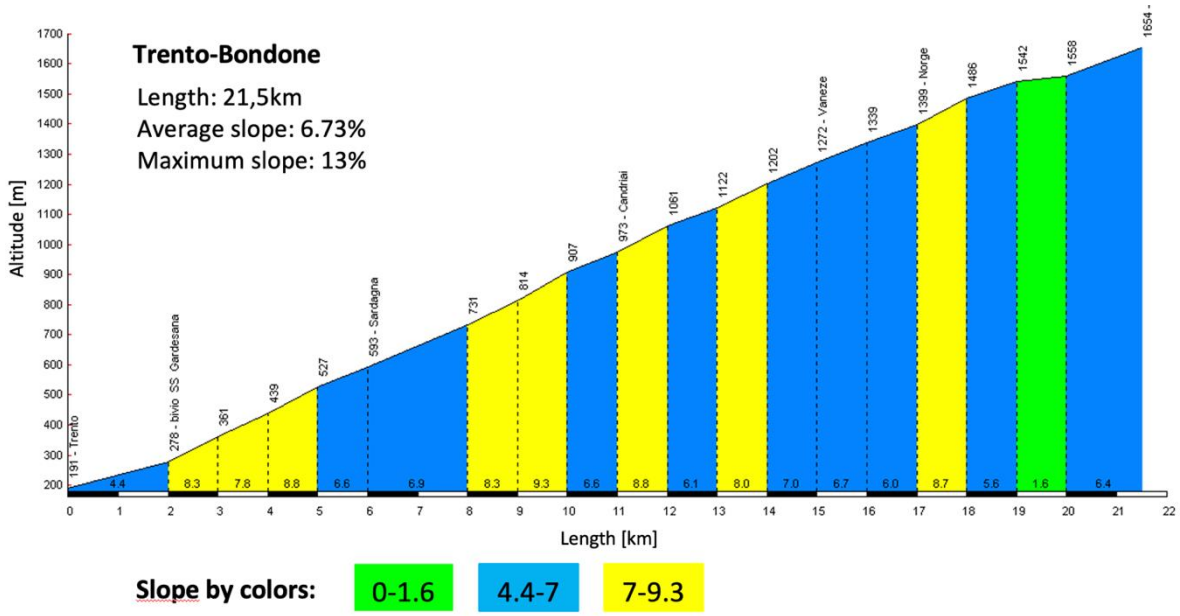

Figure 84: detail about Trento - Bondone road from [154]

Many tests were carried out on the Fiorano track, but the most important were two: the "10 laps" and the "5 laps with heatstroke".

Both were carried out on the same sunny day, at a temperature ranging from 17°C in the first test to 24°C in the second, performed in the afternoon.

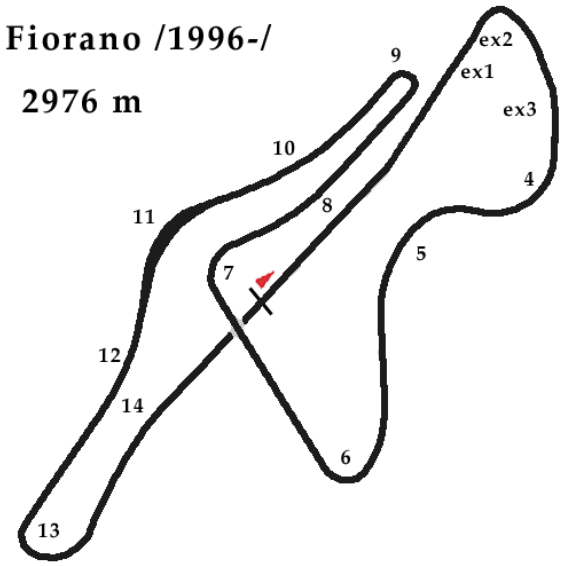

Figure 85: Fiorano track from [155]

6.6 Vehicle test results and discussion

The trends and maximum temperatures reached for the three tests mentioned in the previous paragraph are reported.

6.6.1 Alpine downhill at max performance

The Alpine downhill in max performance was completed in 15' 06" at an average speed of 67.5km/h, at the end of which the heatstroke was performed.

Results of the thermal reached on the rims are summarized respectively in Figure 86, Figure 87 and Table 22.

During dynamic driving, the maximum temperature reached was 2.7°C*; while during the heat soak the maximum temperature was reached on external thermocouple 2 of 4.5°C*. Bearing in mind that the Alpina downhill in max performance is an indication of the car's maximum performance on normal asphalt and that the downhill was covered 4 minutes faster than a customer pace, the rim does not present any problems in terms of driving on public roads.

An additional consideration is that the Alpine downhill was performed at an ambient temperature between 10 and 20°C. Even if the rim temperatures were estimated based on a 30°C ambient, linearizing the results would still keep them below the threshold of concern.

6.6.2 10 laps of Fiorano track

The 10 laps Fiorano session was completed at an average pace of 1'21.50, with 1.5 laps to cool down at the end of the session.

From the analysis of the data in Figure 88, Figure 89 and Table 23, it can be stated that the temperatures seen on the track during the dynamic tests were very far from the threshold values. Furthermore, if the system is cooled regularly, there is no risk of damaging the component in the subsequent heatstroke with the vehicle stationary. The cool down laps are not only a good practice recommended by the manufacturer, but an explicit request presented in the vehicle's use and maintenance manual: the cool down allows not only the brakes but all the vehicle fluids to return to the temperatures suitable for the use of a road car avoiding anomalies and premature ageing.

6.6.3 5 laps plus heatstroke of Fiorano track

The 5 laps plus heatstroke session was done at an average pace of 1'21.50, too. However, in this case, at the end of the test no cool down laps were completed, simulating a maneuver that is considered *"misuse"*, such as a possible driving mistake that could result in the car running off the track and into the sand.

5 laps were enough to bring the temperatures of the engine and brake fluid systems to normal, however two more laps could probably be needed on the wheels, as it can be seen from the telemetry in Figure 88 and Figure 89. Figure 90, Figure 91 and Table 24 show the results of the telemetry and the maximum temperatures reached.

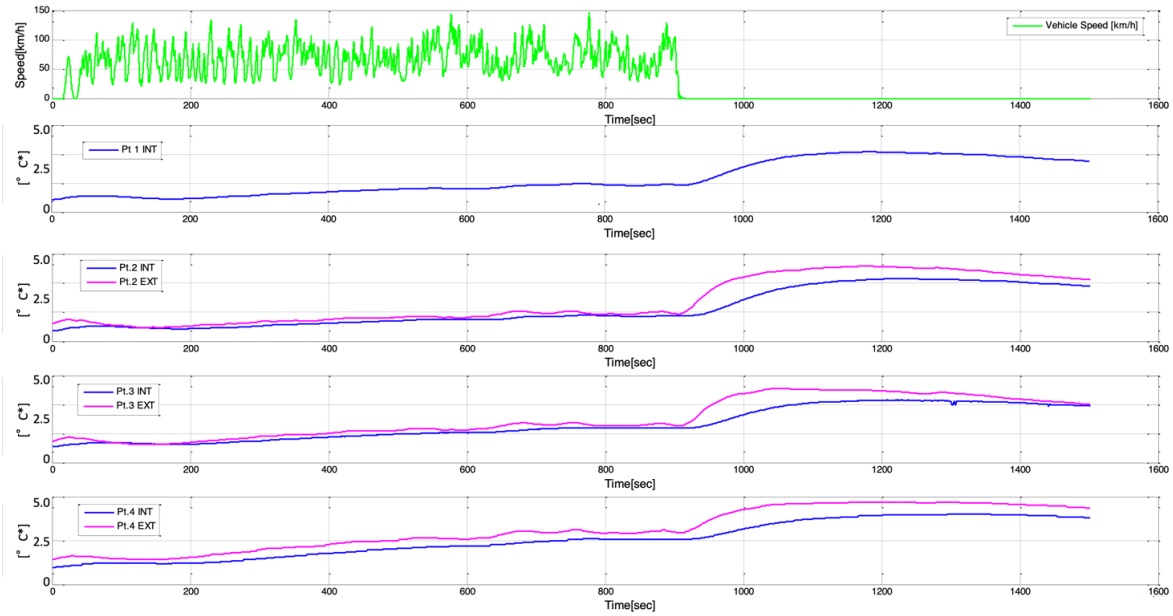

Figure 86: telemetry from Alpine downhill - thermocouples rim barrel: in blue tyre side (internal), in purple TBC side (external)

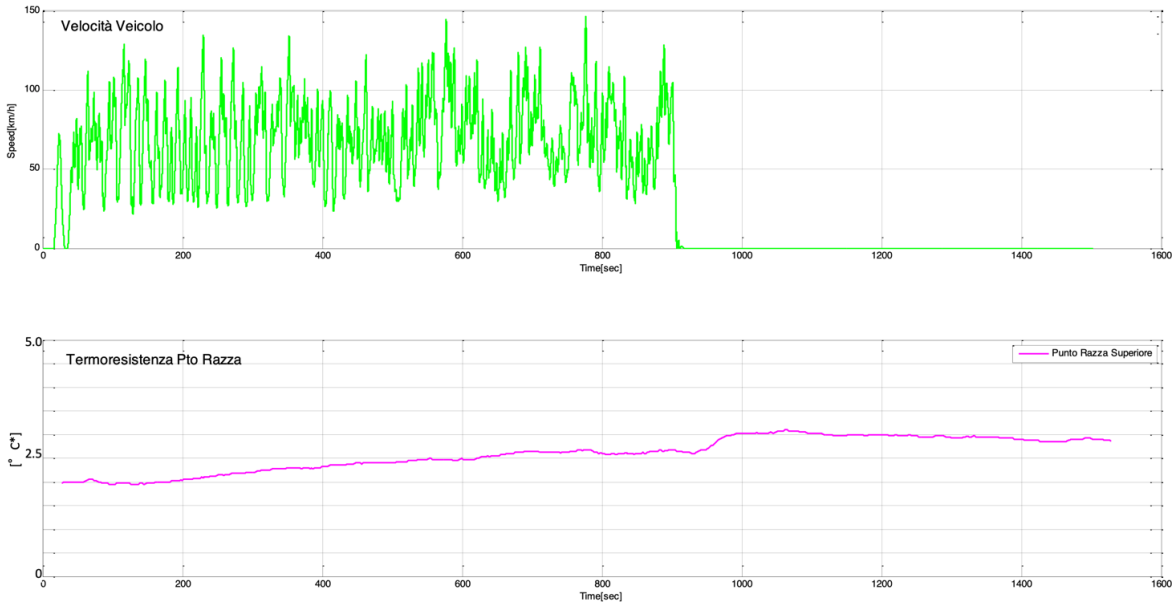

Figure 87: telemetry from Alpine downhill - thermocouple on spoke

Internal	***Temperature [°C*]***	***External***	***Temperature [°C*]***
Pt1	3.8	Pt spoke	3.1
Pt2	3.9	Pt2	4.5
Pt3	3.9	Pt3	4.4
Pt4	3.2	Pt4	3.6

Table 22: max temperature [°C] achieved on Alpine downhill test*

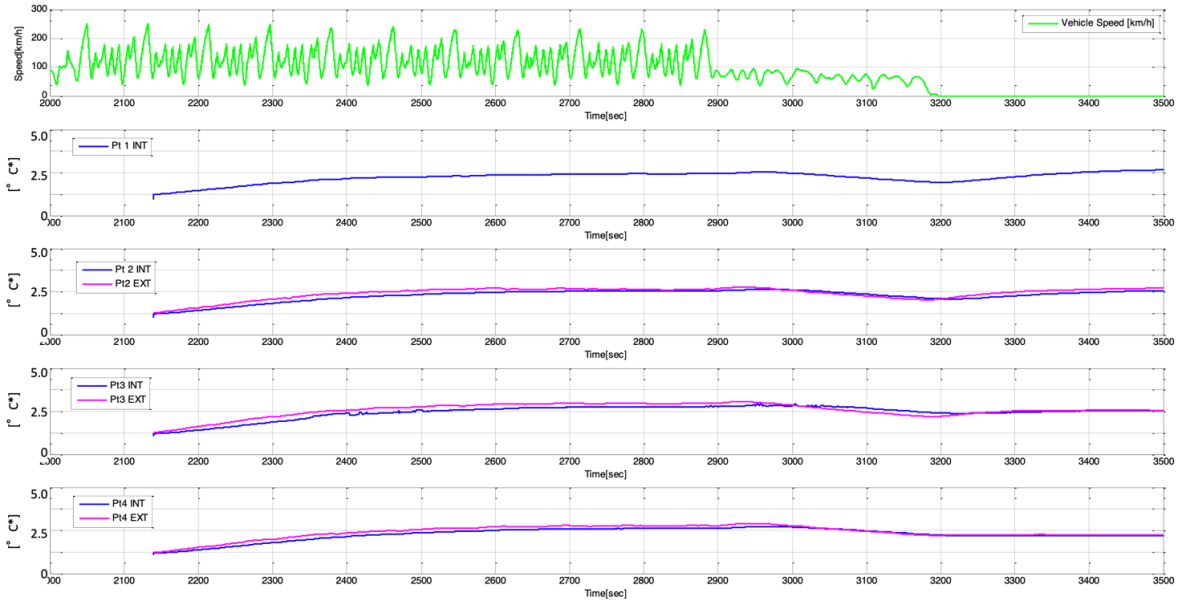

Figure 88: telemetry from 10 laps of Fiorano track - thermocouples on rim barrel: in blue tyre side (internal), in purple TBC side (external)

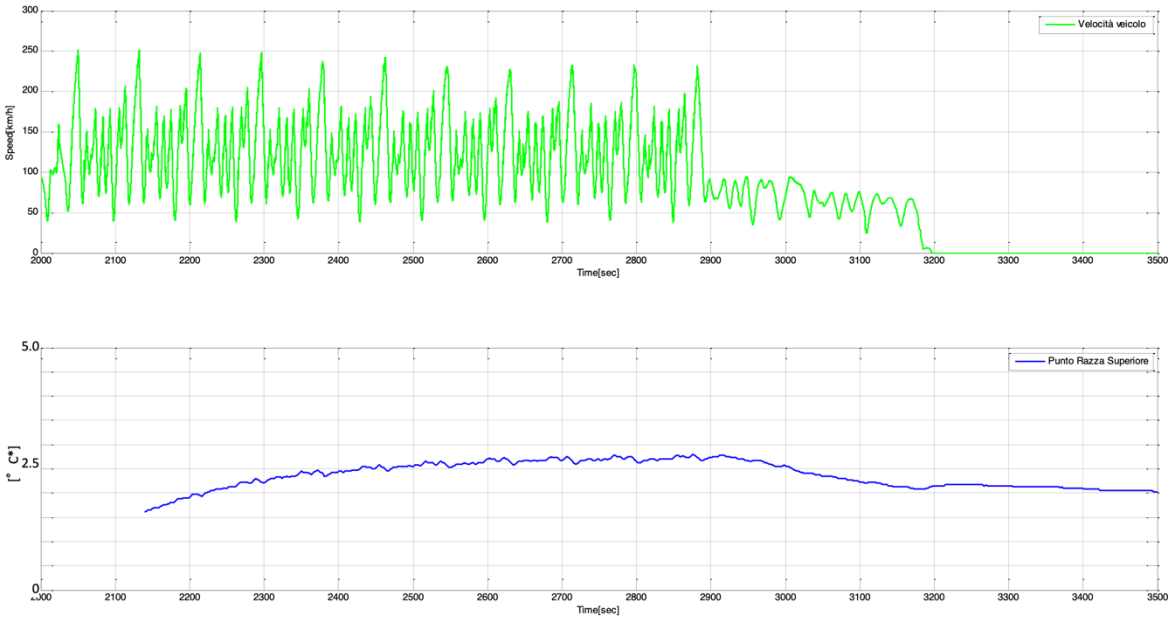

Figure 89: telemetry from 10 laps of Fiorano track - thermocouple on spoke

Internal	***Temperature [°C*]***	***External***	***Temperature [°C*]***
Pt1	2.5	Pt spoke	2.7
Pt2	2.8	Pt2	2.7
Pt3	2.8	Pt3	3.0
Pt4	2.7	Pt4	2.9

Table 23: max temperature [°C] achieved in 10 laps of Fiorano track*

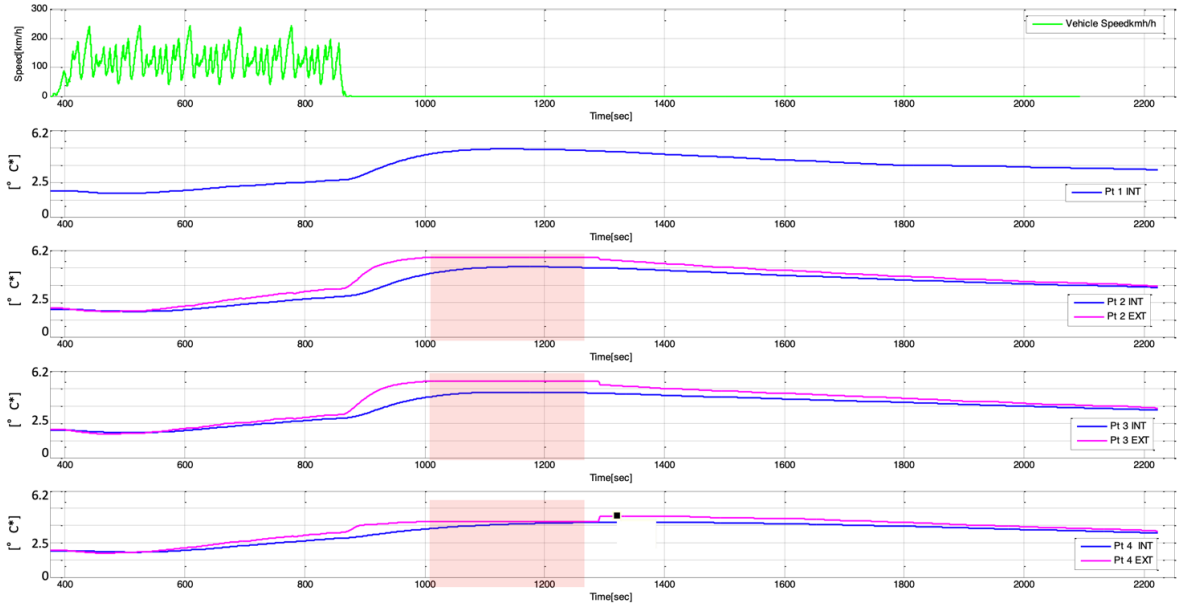

Figure 90: telemetry from 5 laps of Fiorano track plus heat soak - thermocouples on rim barrel: in blue tyre side (internal), in purple TBC side (external)

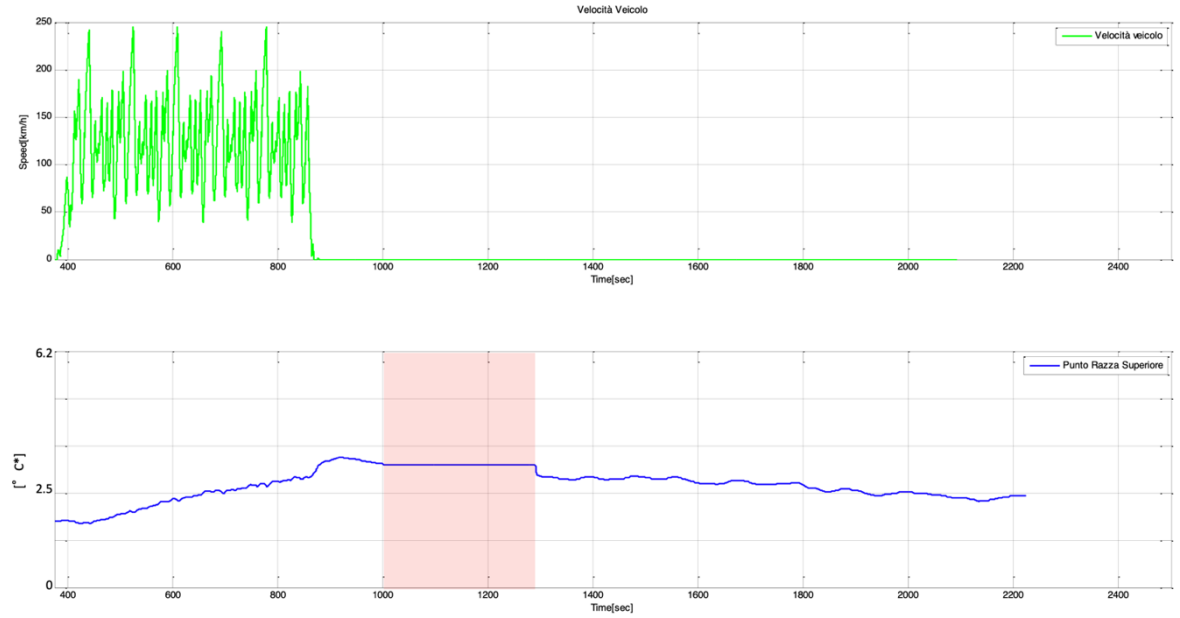

Figure 91: telemetry from 5 laps of Fiorano track plus heat soak - thermocouple on spoke

Internal	***Temperature [°C*]***	***External***	***Temperature [°C*]***
Pt1	4.9	Pt spoke	3.4**
Pt2	5.0	Pt2	5.7**
Pt3	4.7	Pt3	5.5**
Pt4	4.0	Pt4	4.4**

Table 24: max temperature [°C] achieved in 5 laps of Fiorano track plus heat soak. Transmission from external thermocouples were frozen, temperatures with ** are estimated*

Figure 90 and Figure 91 telemetry graphs have “red areas” from second 1000 to 1300: during the heat stroke temperature peak, the data transmission from the TPMS sensor that read the external thermocouples was freezed due to excessive temperature. Therefore, only the internal thermocouple channels were reliable. The temperature data in Table 24 were estimated based on the thermal trends in possession from previous tests.

During this heatstroke, peaks above the glass transition temperature of 5.0°C* were reached (see Figure 92). None of the four wheels showed pressure losses or other anomalies during the entire test.

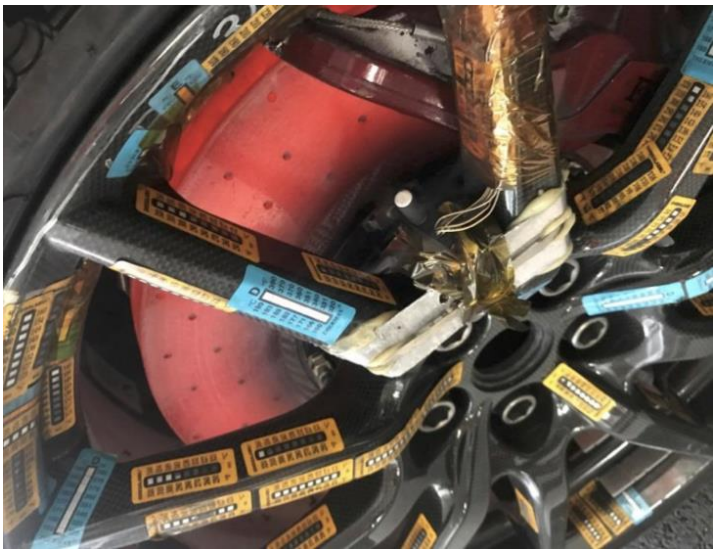

Figure 92: photo of incandescent front brake disk as soon as the car was stopped for heatstroke

6.7 Further improvements added

Now interpolating the data of these vehicle tests with the previous second test carried out on the bench, comparing Table 19 and Table 24, we find that in the vehicle test the internal thermocouple reached a temperature of 5.0°C*, against 4.9°C * achieved in bench test. The heat soak at temperature above 5.0°C* in the vehicle test lasted about 200 seconds, while each test bench cycle lasted about 150 seconds at similar temperature but measured on the TBC. Therefore, it must be expected a progressive damage to the rim barrel with relative loss of pressure if similar maneuvers are performed successively.

Thanks to the data acquisition carried out, it was possible to build a thermal model of the wheel heating dynamics, starting from the decelerations of the car. To guarantee safety in customer use, from the 488 Pista and subsequently all cars equipped with rims in composite material, this thermal model has been integrated into the vehicle dashboard which provides for the switching on of two warning lamps (Figure 93):

1. Yellow warning light: not permanent warning lamp, if the algorithm detects rim temperatures above a specific threshold and the car speed drops below a certain value, it warns the driver to continue driving to cool the vehicle,

2. Red warning light: permanent warning lamp, if the customer has not cooled the car and the yellow light is still turned on and the car is stopped, the algorithm estimates the temperatures of the rims and brake discs. If these are similar to those detected during a heat stroke and above a specific threshold, the red warning light turns on with the warning message to go to the dealer to check the wheels.

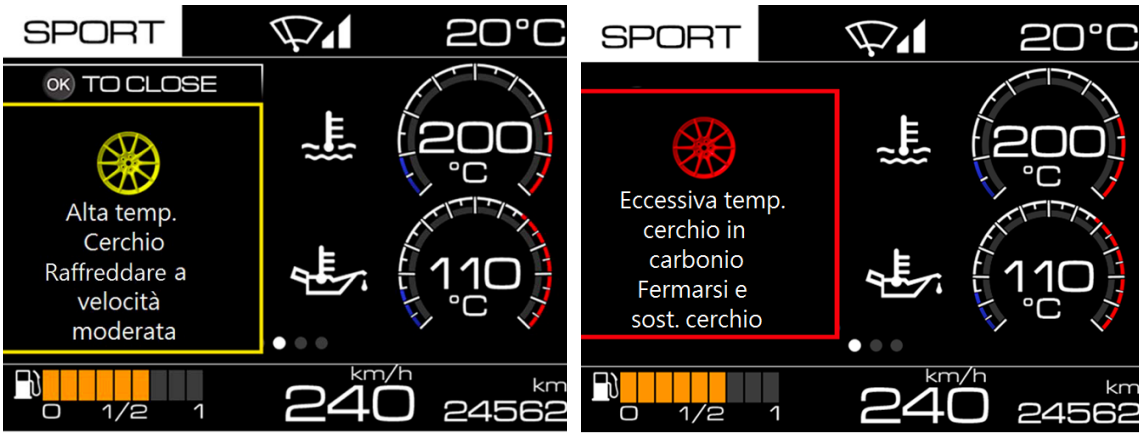

(a) *(b)*

Figure 93: Ferrari 488 Pista dashboard temperature warning messages: (a) yellow warning and (b) red warning

Each carbon rim is equipped with a heat-sensitive strip (like a thermal tape, Figure 94) applied circumferentially on the rim barrel in correspondence of the brake disk. This thermosensitive strip is calibrated with a safety margin of approximately 0.5°C* on the Tg of the wheel's polymer matrix and it's like an historic litmus test for the rim. By checking this strip, the dealer can understand whether or not the wheel has seen heat strokes and in case of positivity, replace the wheel in advance of damage.

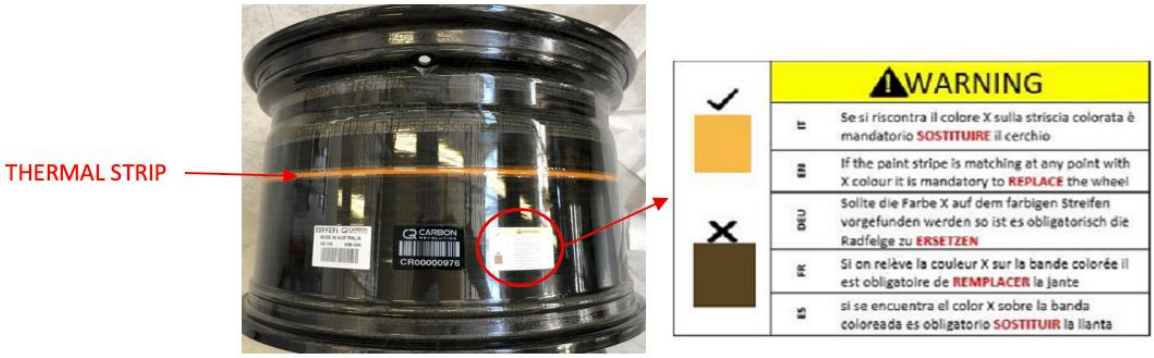

Figure 94: thermal strip applied on the barrel and warning label for dealer users

Chapter 7
ENVIRONMENTAL VALIDATION

"*A Ferrari is forever*" [156]. Taking a cue from a well-known diamond slogan invented by Mary Frances Gerety [157], Ferrari cars must last over the years, like diamonds.

The operating conditions for a wheel of a sports car can be very diverse: from the collector customer who keeps the car in the garage using it occasionally to the customer who races on the track every week, from the Middle East customer in a very hot and wet environmental conditions, to the Russian customer in a cold and dry. The functionality of the wheel must be guaranteed in all conditions and all around the world. For this reason, all Ferrari wheels are tested under tight specific aesthetic standards covering all these scenarios and the rim in composite material could not be outdone.

Environmental tests can be divided into aesthetic and structural. At the second chapter in paragraph 2.3.6 Other validation requirements an overview of the environmental tests performed is presented.

The fifth point of the DFMEA that emerged was: "*resistance to corrosion ageing*". Corrosion and ageing are two major factors that can affect the appearance and structural performance of automotive aesthetic components such as wheels. As seen in previous chapters, CFRP wheels need to be jointed to the vehicle via fastening, and this is done with CFRP-to-metal joint. When joining electrochemically dissimilar materials in an ambient with an electrolyte, such as water or simply, humidity, a galvanic corrosion process could start. This corrosion process is not only unattractive but it's also structurally dangerous as it can lead to the failure of the component. This corrosion process is present in most of the CFRP-to-metal joint [158–161].

The ageing of a CFRP is an on-going development damage to the component depending on the polymer matrix type, the fibre type and their volume fraction, or the mix of these two, operating for enough time in hot or cold temperature, high relative humidity and moisture concentration, under UV radiations and other environmental conditions. Ageing can lead to the yellowing, fading, discoloration or loss of gloss of aesthetic components, as well as the loss of strength and stiffness [162].

This chapter shows how the FMEA addressed the issue of *"resistance to corrosion ageing"*.

7.1 From the FMEA to the laboratory

During the activity of FMEA the performance of the wheel, intended as an assembly fastened to the vehicle, and of the polymeric matrix were questioned. The first aspect concerns the galvanic chain formed by the assembly of wheel components together with bolts, the brake disk and vehicle hub in a humid and salty environment; while the second aspect concerns the adhesion and the corrosion of the thermal barrier coating to the underlying substrate [163,164].

One of the most effective and versatile validation test to evaluate corrosion resistance of materials and coatings is the Neutral Salt Spray test (NSS test) [165–167] called also Salt Fog test, and it is commonly used in the automotive, aerospace, and marine industries.

It consists in exposing a test specimen to a fine mist of saltwater spray in a controlled chamber and at controlled humidity and temperature. The duration of the test and the concentration of the salt solution varies from standard to standard and can be setup to simulate different environments and test cycles. After the test, the specimen is evaluated for signs of corrosion, such as pitting corrosion [160], rust [158] or discoloration [162]. Thus, it is easy to understand how this test is the key to a good assessment of wheel ageing.

Mandel *et al.* [168] have proposed a methodology for calculating the galvanic corrosion effects in a 5% NaCl environment of an Al6060 T6 jointed with a CFRP plate through finite element calculation and then verified it experimentally with a very high correlation; however, the phenomenon of galvanic corrosion must be physically tested because of many variables to be considered.

Ferrari used this test to evaluate:

1. Quality of the paint coat,
2. Moisture absorption rate of the coat and the resin,
3. Galvanic corrosion between assembled components,
4. Level of corrosion of thermal barrier coating.

The test has been performed with the wheel fully assembled with his wheel bolts, hub and brake disk and was left in vertical position (as fitted on the vehicle), sprayed with the salt spray fog with chemical composition of 5% NaCl solution and pH between 6.5 and 7.2 in a 35°C temperature and 95% humidity as for Fiore *et al.* [160]. The standard test duration time is 500 hours, nonetheless in this specific case the test duration time has been doubled to apply a safety factor and to get confidence on the result.

Furthermore, to assess the structural strength of the wheel and the adhesion of the thermal barrier coating to the spokes and the barrel, the wheel was tested at cornering fatigue monitoring, as presented in chapter 3, the stiffness of the wheel and visually inspecting aluminium components and coatings.

Initially, an aftermarket wheel from the supplier was tested to identify and resolve any potential issues, due to the experimental nature of the activity.

7.2 CFRP aftermarket wheel neutral salt spray test

The aftermarket wheel tested can be found in Table 25. The result investigation has been done with optical microscope and SEM analysis. It consists in a RTM rim manufactured with an epoxy resin system with a Tg above 4.75°C*, painted with transparent coating with variable thickness from 40 to 100 μm and with a triple coatings Al_2O_3-YSZ-Al_2O_3 thermal barrier. Assembled with Al6061 T6 inserts and backplate with hard anodization with 30÷50 μm thickness. Inserts got steel AISI 316 anti-rotation pins and zinc-plated steel press-in circlip (see Figure 95).

	Aftermarket wheel
Rim technology	RTM – epoxy resin with Tg > 4.75°C*
Final paint	Transparent – thickness 40÷100 μm
Thermal protection	Multi-coating plasma spray Al_2O_3-YSZ-Al_2O_3 - thickness 300÷500 μm
Inserts	Al6061 T6 black hard anodization thickness 30÷50 μm
Anti-rotation pins	Steel AISI 316
Circlip for inserts	Press-in circlip steel zinc-plated – thickness 30 μm
Backplate	Al6061 T6 hard anodization - thickness 30÷50 μm

Table 25: CFRP wheel configuration proposed

(a) *(b)*

(c) *(d)*

Figure 95: aftermarket wheel in neutral salt spray test: (a) top view, (b) rim view, (c) back view, (d) detail about backplate area

The wheel was tested according to ASTM B117 [165] without being mounted on the vehicle hub because it did not fit due to a different wheel bolts PCD and centering diameter. The outcome immediately after the test is presented in Figure 96.

(a) *(b)*

Figure 96: aftermarket wheel after neutral salt spray test: (a) top view, (b) back view

At a first evaluation, it can be seen corrosion dripping around the inserts (Figure 96a) and oxide formation on the entire rear part in contact with the thermal barrier coating (Figure 96b).

Each oxide formation has been analyzed with SEM to figure out what caused it. Each sample was taken and then flushed with demineralised water in order to remove the residual salt from the test. Next to each photo, its SEM analysis is reported for:

1) the formation of aluminium oxide from the inserts (Figure 97a), confirmed by SEM (Figure 97b),
2) the formation of aluminium oxide from the backplate (Figure 98a), confirmed by SEM (Figure 98b). It can be found also a large amount of fluoride, most likely from the assembly grease used to press-in the circlip,
3) the formation of aluminium oxide bubbles on the spokes (Figure 99a), confirmed by SEM analysis (Figure 99b),
4) the formation of aluminium oxide on the edge of the application of the TBC on the rim (Figure 100) and on the spokes (Figure 101), with a SEM spectrum similar to Figure 99b.

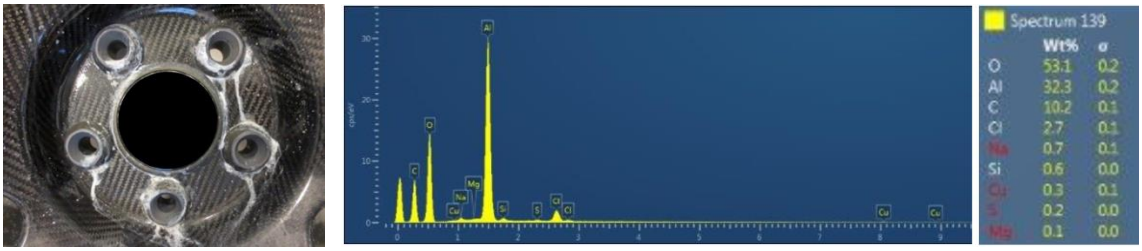

(a) *(b)*

Figure 97: (a) oxide formation from inserts, (b) SEM analysis

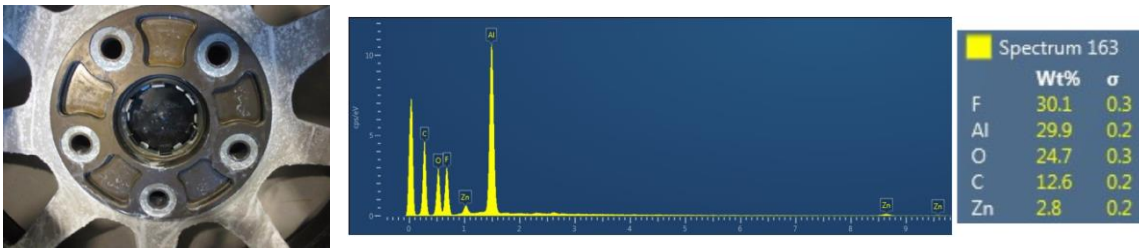

(a) *(b)*

Figure 98: (a) aluminium oxide formation from backplate, (b) SEM analysis

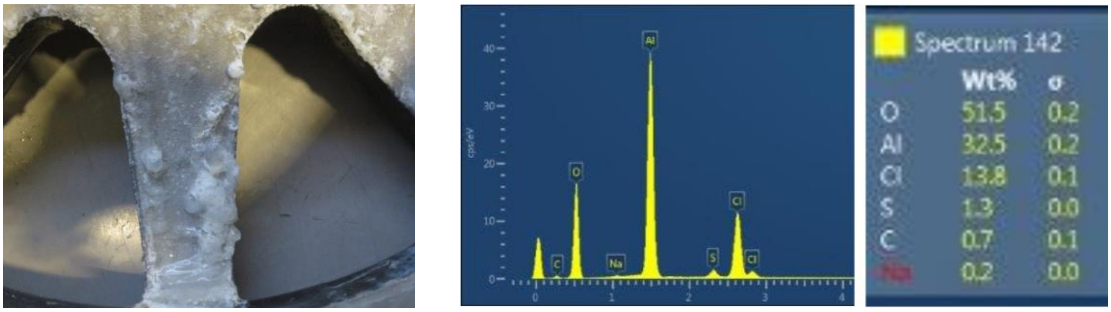

(a) *(b)*

Figure 99: (a) aluminium oxide bubbles on the spokes, (b) SEM analysis

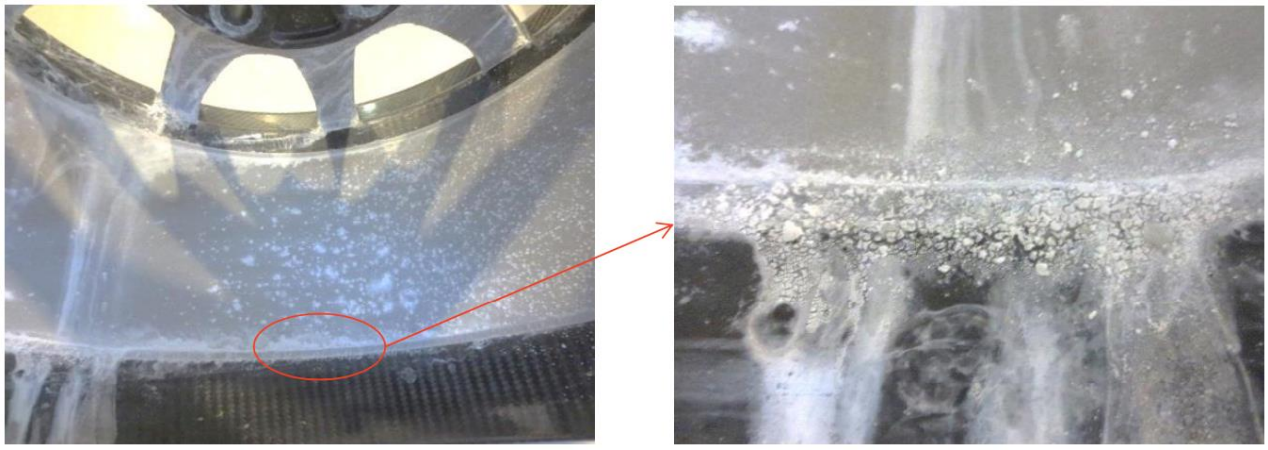

Figure 100: detail about oxide formation on the thermal barrier coating on the rim barrel

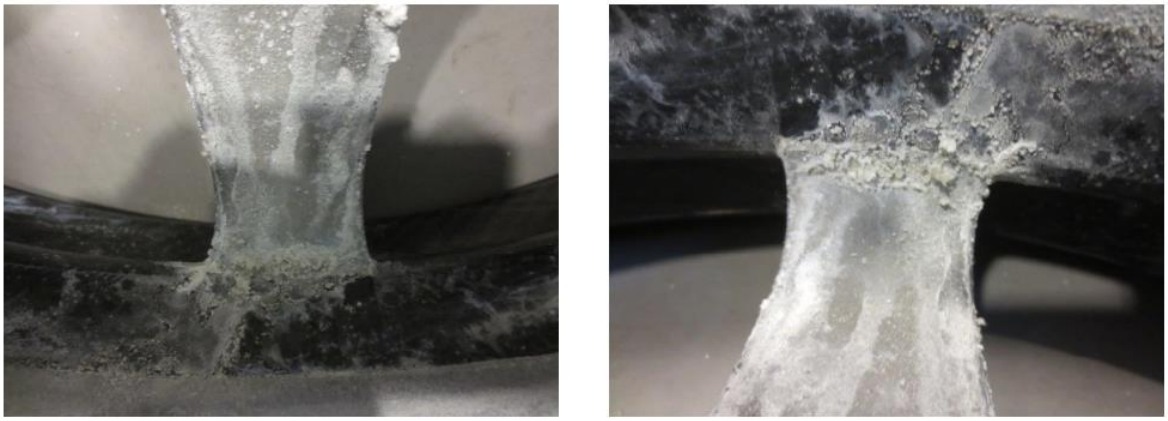

Figure 101: detail about oxide formation on the thermal barrier coating on the spokes

Furthermore, after rinsing the wheel with demineralized water, the formation of swelling by the thermal barrier coating on the spokes (Figure 102a) and on the barrel (Figure 102b), and spontaneous delaminations of the thermal barrier coating from the spokes (Figure 103) have been noticed. These happened specifically in the area of the spoke with the smallest radius where the coating adhesion is more challenging.

Inserts were removed from the wheel and analyzed together also with steel circlip (Figure 104 and Figure 105).

(a) *(b)*

Figure 102: swelling of the thermal barrier coating: (a) on the spokes, (b) on the rim barrel

Figure 103: spontaneous delamination of TBC from back of the spokes

(a) *(b)* *(c)*

Figure 104: inserts removed from the wheel: (a) top view, (b) back view, (c) side view

(a) *(b)*

Figure 105: (a) circlip removed from (b) backplate. The visible damages on the circlips were caused during their disassembly and analysis

Covered by the white aluminium oxide residue, severe pitting corrosion was found on the edges of the inserts in contact with the carbon, where the water, the electrolyte, could establish the electrochemical bond. These have been observed thanks to stereo microscope (Figure 106).

On the other hand, zinc-plated circlip and aluminium backplate did not shown clear sign of corrosion.

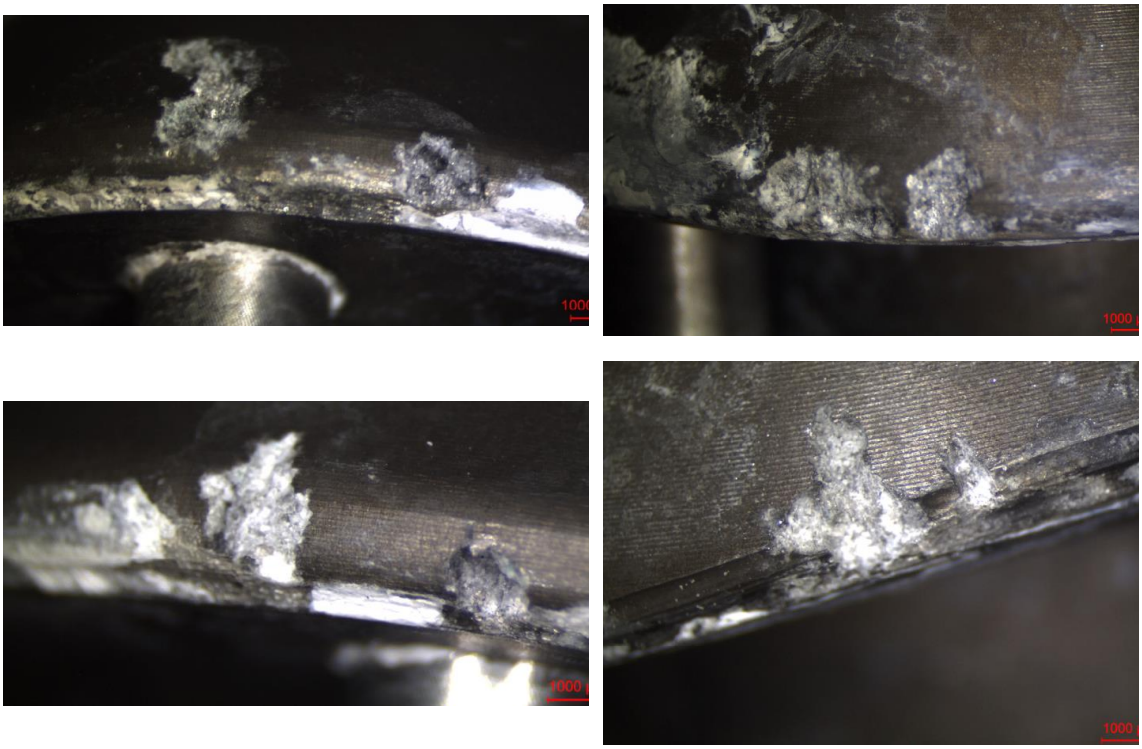

Figure 106: pitting corrosion on the edge of the inserts observed with a stereo microscope analysis

Therefore, the result of the first neutral salt spray test showed a heavy degree of corrosion of the inserts, seat of the bolts, while the backplate and the circlips showed no corrosion.

The thermal barrier coating presented a widespread state of corrosion, several swellings with detachments of the coating on the spoke-to-rim connection where the radius is smaller.

7.3 Causes investigation and potential remedies

Several neutral salt spray tests have been performed after this first one. In each test, improvements have been tried.

In the following paragraphs, the causes investigation and the potential remedies tried are listed.

7.3.1 Inserts corrosion causes investigation and improvements

The root cause of heavy degree of corrosion is galvanic corrosion.

Figure 107, from [169], shows galvanic series for metals in seawater. It is clear that graphite (CFRP) and aluminium alloys have a huge difference in terms of electrode potentials, with CFRP positive and so called cathode and aluminium, negative and so called anode.

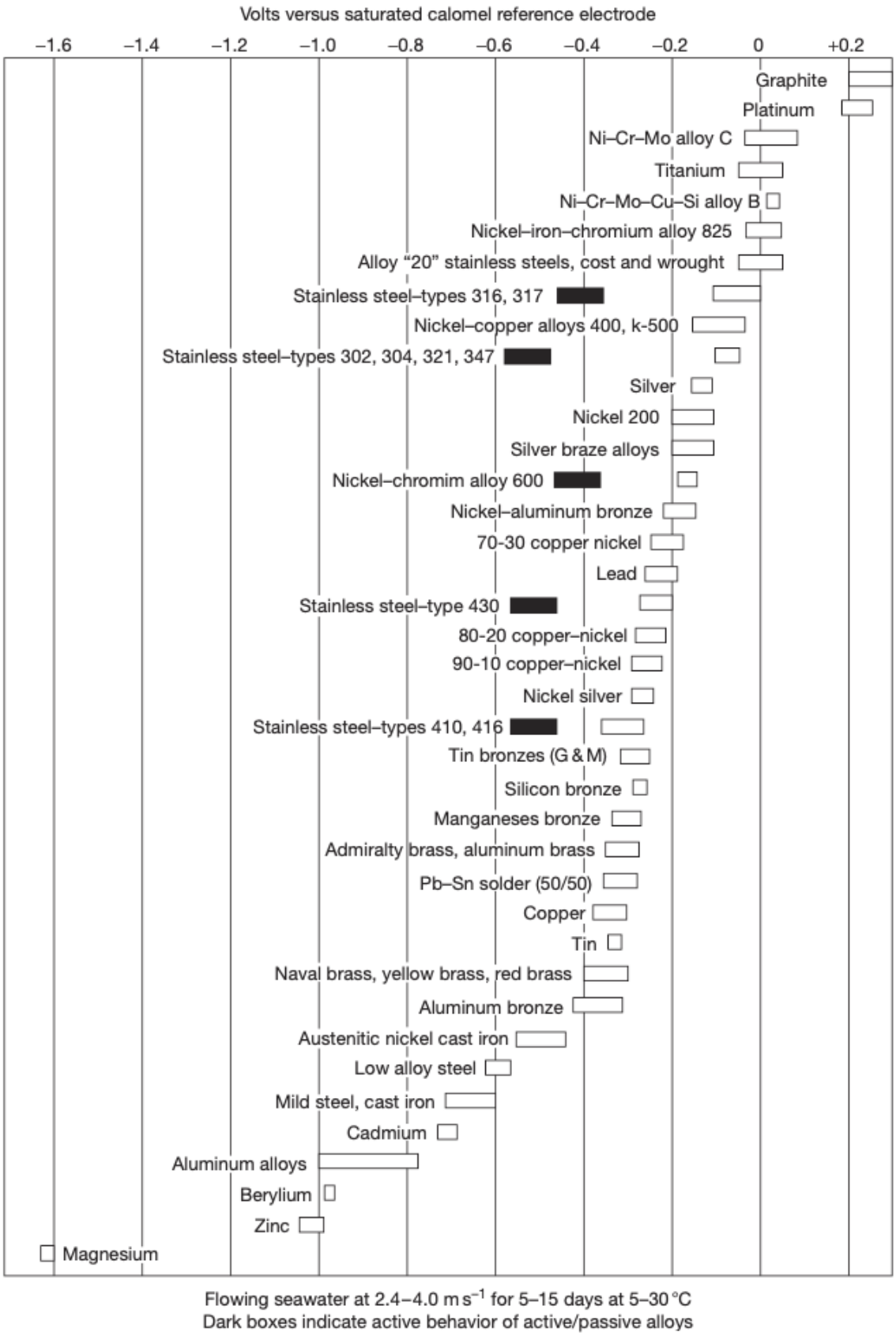

Figure 107: galvanic series for metals in seawater with moderate flow. From [169]

For Schneider *et al.* [170], to initiate the galvanic corrosion in the coupling between two or more different materials, these conditions must be present:

1) electrical contact between the materials,
2) the materials are immersed in the same electrolyte,
3) according also to Tostmann [171], more than 50mV of potential difference must exist between the different materials.

Morimoto *et al.* [161] presented an analytical analysis of the phenomenon between aluminium and CFRP thanks to the Pourbaix diagram. Interpolating the two polarization curves for aluminium (anode) and graphite (cathode), it's easy to understand that aluminium (anode) could suffer from the pitting corrosion close to the contact between the components to a more extensive severe corrosion.

In Figure 108 a simplified scheme of the galvanic corrosion of the wheel tested is proposed.

Accordingly with Morimoto *et al.*, the pitting corrosion occurs between aluminium insert, the anode, and CFRP laminate, the cathode, on the small edge where salt water, the electrolyte, could generate an electrical contact. By contrast, in the same joint but between backplate, the anode, and CFRP laminate was not possible to generate corrosion, probably because of the geometry of the backplate that allow the salt water not to enter between them.

In Figure 108 it's also represented the wheel bolt: on the first test was not present, it will be present in all following 488 Pista wheel testing, fully installed with hub and brake disk. In this case a sealing effect from salt water from the titanium wheel bolt clamped it is expected.

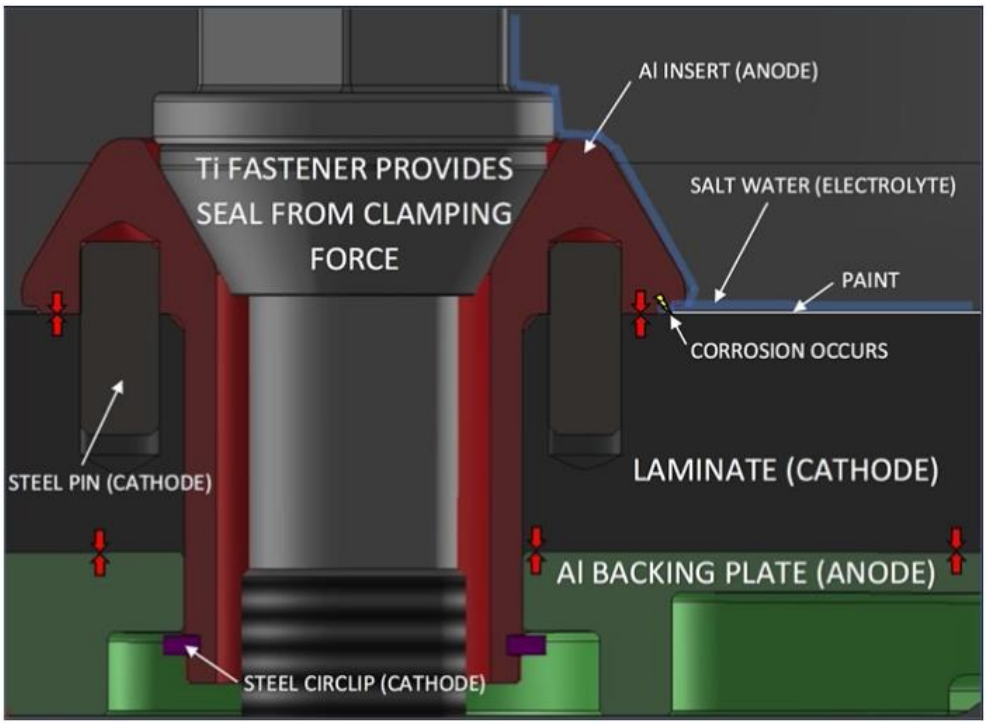

Figure 108: galvanic corrosion scheme of the wheel

Thus, two areas have been investigated: the first a better insulation of the insert from either laminate and salt water, the second an increase in the small radius where apparently all pitting corrosion started probably due to its propension to generate the electrical contact.

Improvements introduced to resolve this issue were (see Figure 109):

- to improve insulation between laminate and insert, a glass fiber ply has been added as first layer of laminate and insert coating has been incremented to a thickness of minimum 60 μm,
- to avoid cathode effect from steel pin, a fiberglass dowel pin has been introduced.

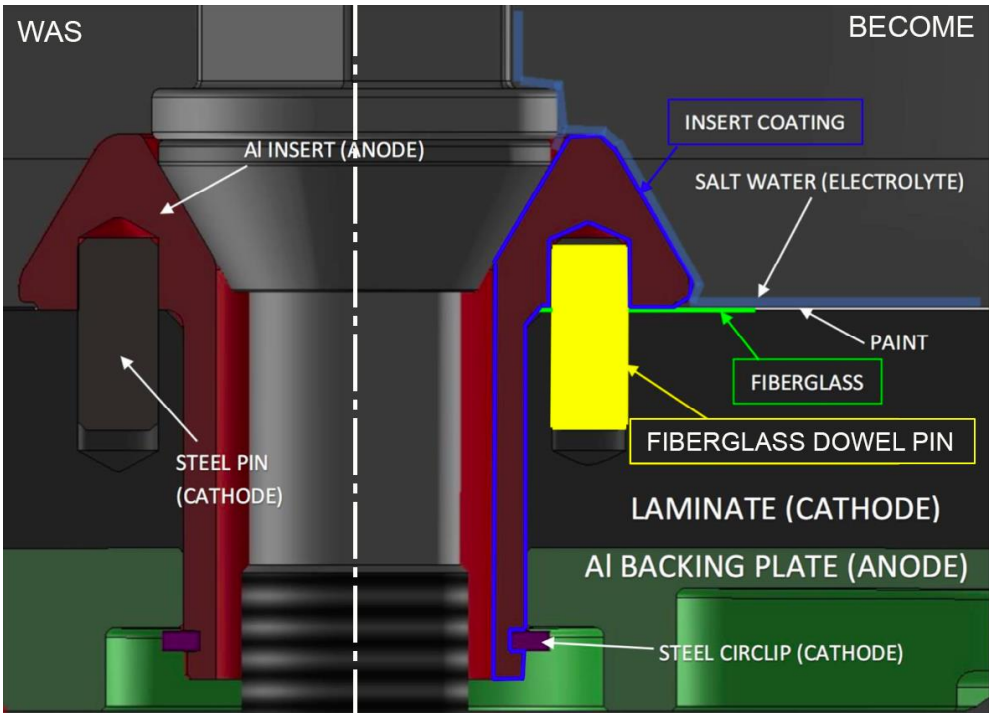

Figure 109: insert galvanic corrosion solutions: on the left, the first trial; on the right the list of improvements

In the final wheel configuration, another difference has been introduced: the material chosen for the insert is not the tested aluminium alloy Al6061 but it is an Al7075. This is due to the high compression load generated from the bolt when tightened, for which it was necessary to switch to an alloy with at least 50% higher yield tensile strength.

Aluminium alloys from 7xxx series suffer from corrosion and, in particular, from a phenomenon called *Stress Corrosion Cracking* (SCC) or *corrosion fatigue* [172]. As clearly resumed by Umamaheshwer Rao *et al.* [173], this phenomenon is a crack process that occurs in susceptible alloys, as 7xxx series, and it can be really harmful as it is difficult to predict, especially on a wheel fitted to the vehicle. SSC requires the following conditions to happen: the material needs to be susceptible to the SCC phenomenon, the component needs to be loaded with a level of tensile stress higher than certain threshold value and a specific condition that promote cracking must be present, as for example, pitting corrosion.

Aluminium alloys 7075 are widely used also in aerospace. To prevent SCC phenomena, T73 or T7351 heat treatment is necessary. This heat treatment is aged more than standard T6 to provide a good SC resistance [174].

Thus, the inserts are made of Al7075 T7351 from SAE Standard AMS-QQ-A-225 [117]. An extensive FEA optimization activity has been performed to find the best geometry for the insert that can be easily anodized, without small radius to not generate points where pitting corrosion could start, to increment the stiffness of the insert and to reduce the stress inside it when tightened. The resulting geometry can be seen in Figure 110b.

a) *b)*

Figure 110: composite wheel inserts: a) proposed version and b) final version with GFRP dowel pin

7.3.2 Thermal Barrier Coating corrosion causes investigation and improvements

The hypothesis of the genesis of the bubbles and the detachment of the TBC from the rim can be attributed to corrosion of the bond coat with the rim. The coating is porous [147,164] which also assists with thermal insulation. On the contrary, this porosity allows water to penetrate the coating. When the electrolyte reached the resin surface and this has been breached by carbon fibre, localized galvanic cells in the bond coat are created (Figure 111). This leads to corrosion with generation of alumina oxide. As it corrodes, the oxide forces the interlayer to expand, generating bubbles in the coating. Lastly, where the adhesion was weaker, TBC delaminated from the surface.

Therefore, the root cause is to be considered in galvanic corrosion of the bond coat with carbon fibre below.

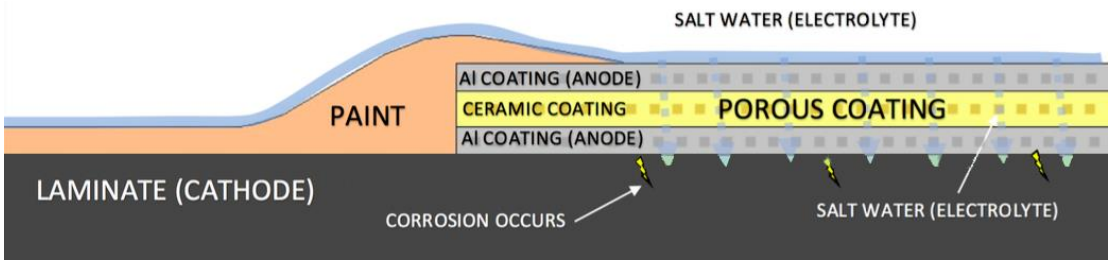

Figure 111: diagram of the TBC galvanic corrosion

A barrier must therefore be created between TBC and carbon fibre: a double fiberglass insulative layer will help ensure no breaches are possible and to avoid the opportunity for a galvanic cell to develop. Furthermore, the paint coating, that is blended over the edge of the TBC in all areas, needs to be improved to insulate better the edge of the coating (Figure 112).

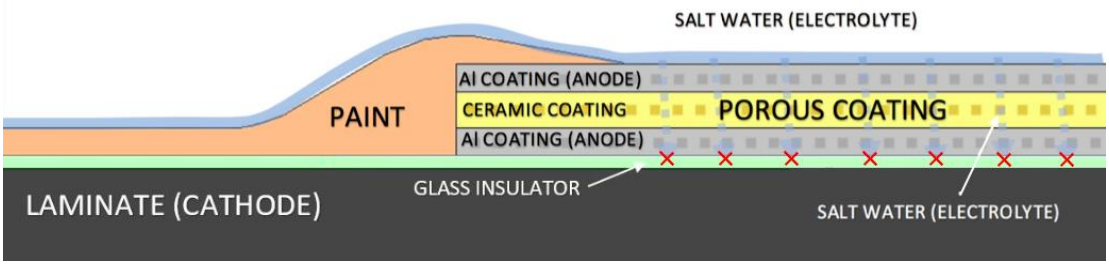

Figure 112: diagram of the TBC galvanic corrosion improvements

7.4 Final production wheel neutral salt spray test

After more than five neutral salt spray tests with complete wheel assembled, tests with only small samples and dozens of analysis hours, the final wheel configuration was identified and tested.

All the improvements described in previous chapter were implemented and, in Figure 113, it is represented the pre-production wheel assembled with hub, brake disk and titanium wheel bolts ready to start the test.

The test has been performed for the standard 500h for aesthetic performance and doubling the number of hours for structural concerns. Before taking all sections for analysis, the wheel has been sent to the supplier to perform a cornering fatigue test up to 250k cycles to certify its structural consistency.

Figure 113: pre-production wheel assembled with hub, brake disk, titanium bolts ready to start neutral salt spray test

The first aspect under analysis is the painting. When inspecting the outcome of the aftermarket wheel, no particular attention was paid to the performance of the paint because this is not a structural performance related to safety concern; however, this thing cannot be ignored in the final validation test of the pre-production wheel.

The outcome of 500 hours of NSS test is borderline acceptable as some paint blistering started to come out after 300 hours only on the side of the spoke in the rear area just near the edge where TBC ends. In Figure 114, three phases of NSS duration are presented.

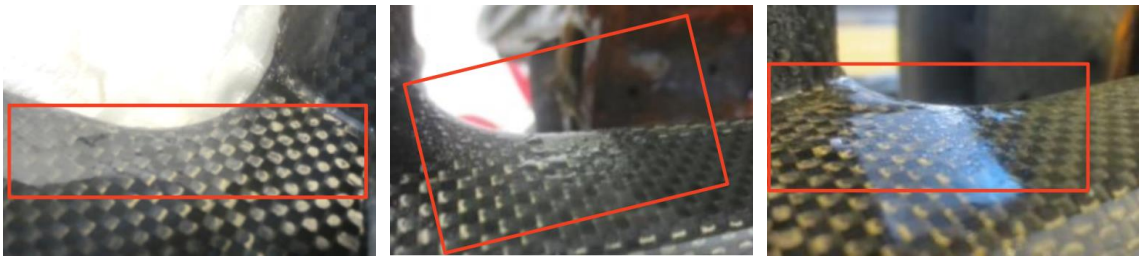

(a) (b) (c)

Figure 114: paint performance in NSS test, (a) after 300h there are no blisters, (b) after 400h some blisters started to grow, (c) after 500h blister present, only near the back of the spoke radius

With a specific analysis on a wheel painted without TBC application which did not present this outcome, it was understood that this phenomenon is, in all probability, due to TBC particles which escape from the masking of the wheel during the TBC application and that remain trapped between the paint and the resin, generating galvanic corrosion which has the effect of swelling the paint above. In Figure 115 and Figure 116 details of the blistering effect on the wheel are shown.

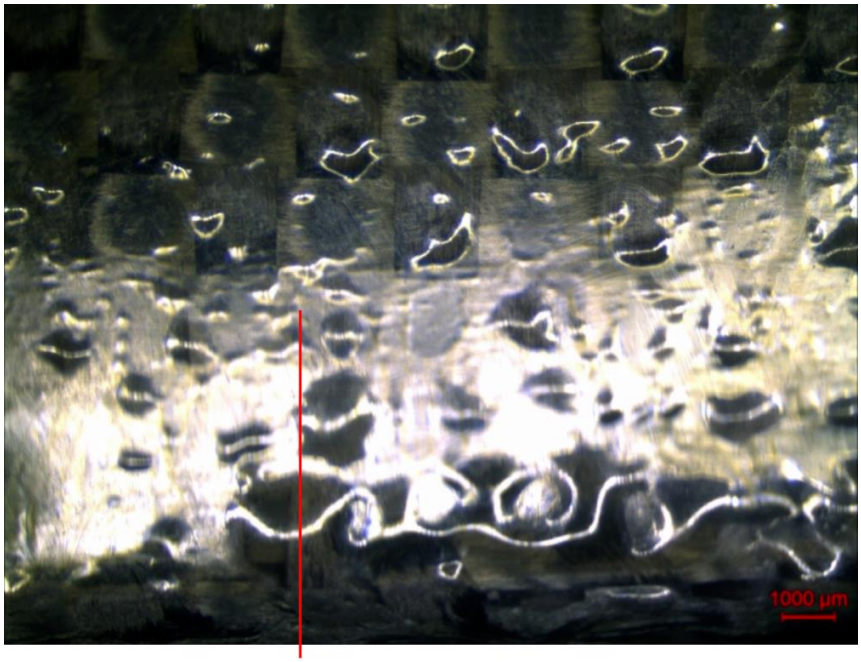

Figure 115: details of paint blisters under microscope. Red line is there the section has been done.

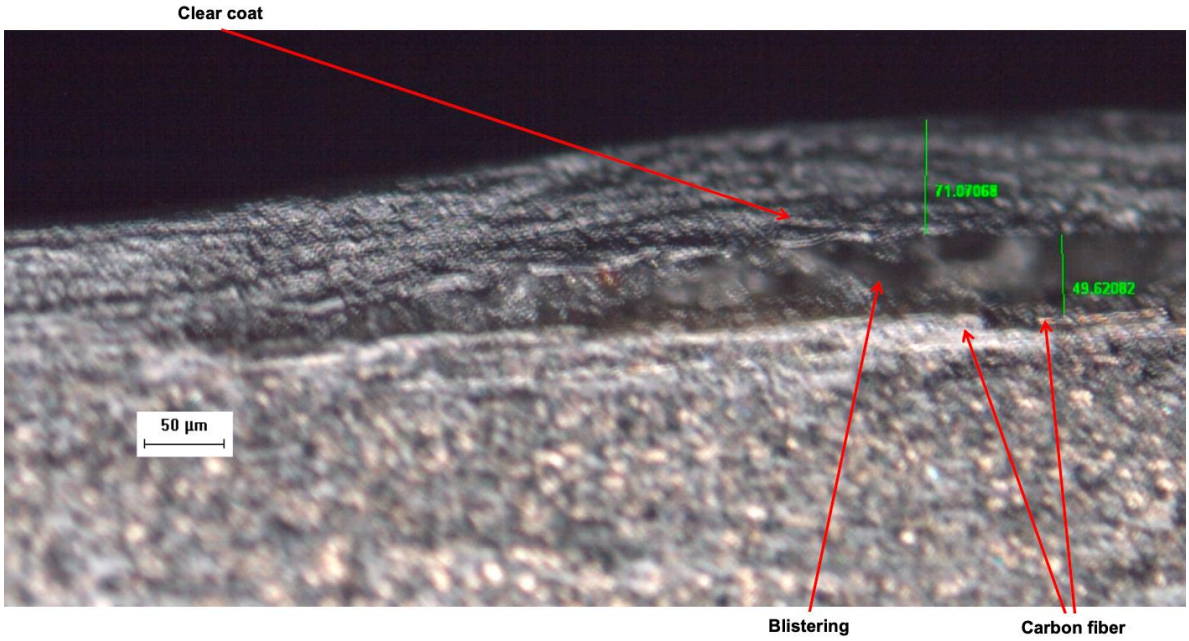

Figure 116: section viewed under the microscope

Second aspect under analysis are the inserts. Their performance after 1000 hours and a cornering fatigue test, shown in Figure 117, were good and the test returned inserts with just some pitting corrosion point at the very top of the edge between titanium wheel bolt and insert cone.

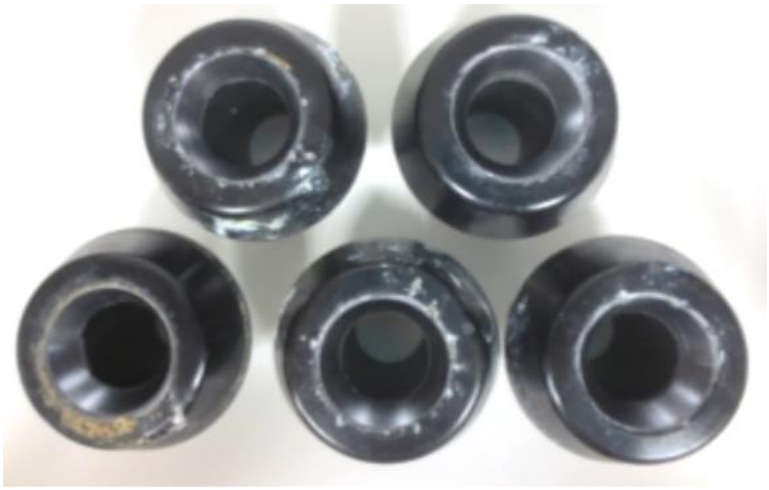

Figure 117: inserts after NSS test

After the test, chemical composition (Table 26) and thickness of anodization have been measured, finding an average value of 55 µm.

	Si	Fe	Cu	Mn	Mg	Cr	Zn	Ti
Std for Al7075 [117]	0.40 max	0.50 max	1.20 - 2.00	0.20 max	2.10 - 2.90	0.18 - 0.28	5.10 - 6.10	0.20 max
Measured	0.09	0.24	1.35	0.02	2.78	0.21	5.21	0.03

Table 26: inserts chemical composition

Third aspect investigated was the backplate. In Figure 118 and Figure 119 the backplate can be seen. The contact with the hub, hardly attacked from corrosion and which generated red rust, also attacked the aluminium of the backplate in the centering diameter leaving some pitting corrosion points as shown in Figure 118b.

(a) *(b)*

Figure 118: backplate after NSS test - side in contact with the hub and brake disc: (a) global view, (b) detailed view of red circled area

From the other side, the aspect is almost as new apart for two pitting points at the very edge of the centering diameter towards the composite wheel moulding, one of these detailed in Figure 119a.

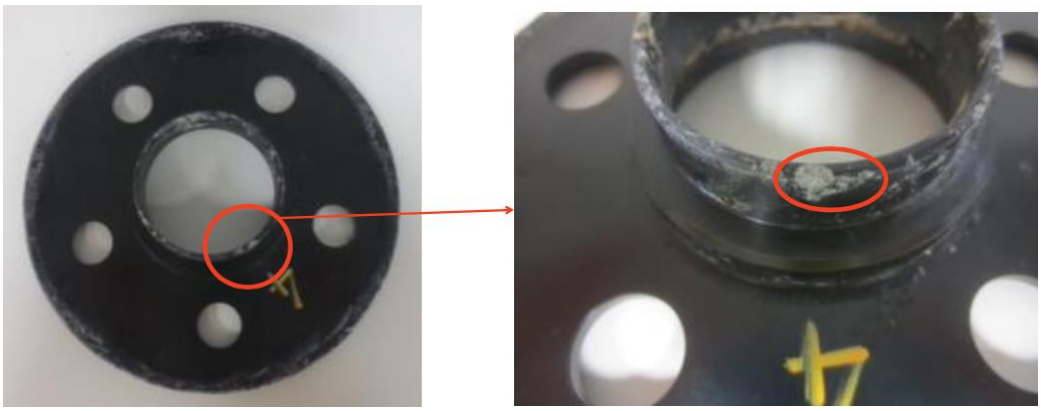

(a) *(b)*

Figure 119: backplate after NSS test - side in contact with the moulded wheel: (a) global view, (b) detailed view of red circled area

After the test, chemical composition (Table 27) and thickness of anodization have been measured, finding an average value of 46 μm.

	Si	Fe	Cu	Mn	Mg	Cr	Zn	Ti
Std for Al6061 [175]	0.40 - 0.80	0.70 max	0.15 - 0.40	0.15 max	0.80 - 1.20	0.04 - 0.35	0.25 max	0.15 max
Measured	0.53	0.31	0.30	0.12	0.98	0.14	0.03	0.03

Table 27: backplate chemical composition

Globally, the performance of the aluminium components is satisfied as they are designed to be easily replaced in case of hard corrosion happen.

Last aspect investigated was the TBC adhesion on the new barrel over a double layer of GFRP.

Figure 120: back view of the wheel assembly after 1000h NSS test

In Figure 120, back view of the wheel assembly after the NSS test is presented.

It is important to note that the red rust residue found on the underside of the rim barrel should not be mistaken as a sign of significant corrosion: this is coming from the corrosion of the hub that for gravity dropped on the barrel. Attention, instead, must go to the other sides of the barrel, in particular to the area circled in green: this time the electrolyte has not generated any corrosion of the aluminium oxide.

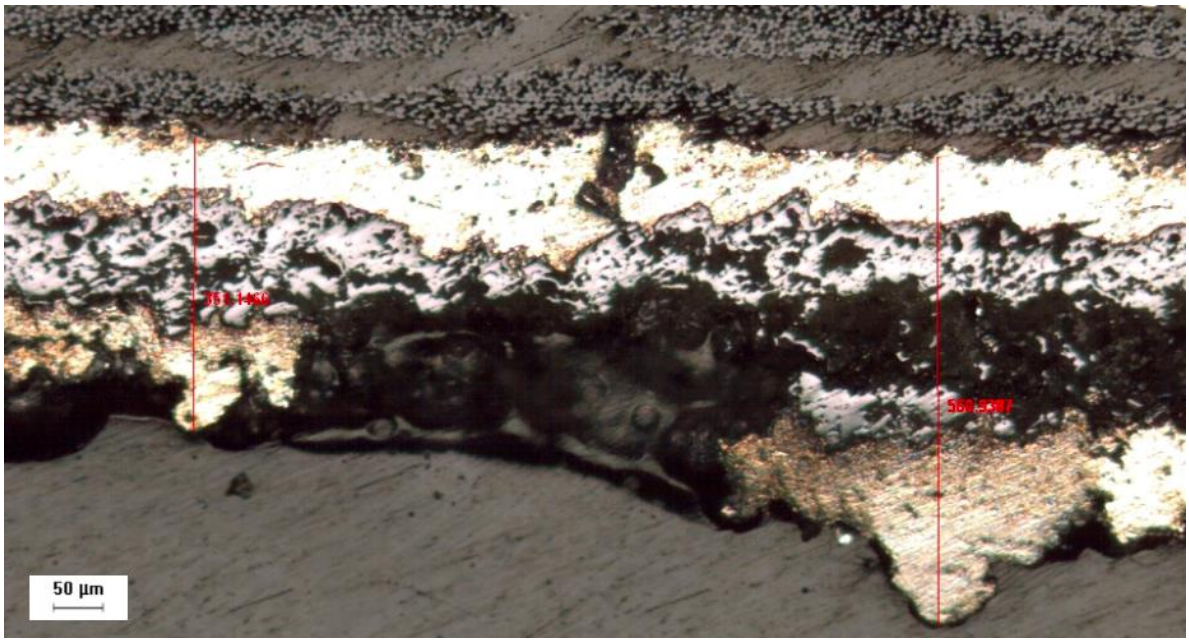

Figure 121: section of TBC area

By sectioning the barrel in that area (Figure 121), the three layers of TBC and the two layers of glass fiber are noted, but no infiltration and bubbles are present as in Figure 102 and Figure 103 or Figure 116 for the paint. In the section, the thickness of the TBC varies from 300 µm to 560 µm, with the lack of the third layer in the central area of the image.

After the NSS test, the wheel has performed a cornering fatigue test up to OEM standard cycles, completing the test with less than 15% of stiffness loss. This result revealed a greater degradation versus the test results presented in chapter 3 (6% of stiffness loss, see Figure 19). This can be attributed to the variability in the production process, as there are still some hand-made processes that have yet to be fully optimized as this was a pre-production wheel.

However, the cornering fatigue result is in line with the results of other wheels tested; therefore, from structural aspect, the composite can be considered immune to ageing caused by NSS test (humidity and salt), but not to the galvanic corrosion that is generated from the assembly of aluminium components. Even the TBC, thanks to the GF double protection plies, is resistant to the demanding OEM test standards without detachments from the barrel and spoke surfaces.

Chapter 8
CONCLUSION

The composite wheel presented in this dissertation is the first of its kind developed by Ferrari and one of the earliest to be made available in the market as an alternative to standard cast or forged aluminium wheels. In addition, two other composite wheels were developed for two different projects.

The composite material offers a weight advantage of between 20-30% compared to forged wheels, and between 30-40% compared to cast wheels, depending on the wheel style. Despite this mass reduction, the wheel maintains its bending stiffness, providing significant reductions in rotating inertia of up to 35% compared to forged wheels and up to 45% compared to cast wheels. This leads to a significant improvement in responsiveness to steering input and changes of direction, as well as faster and more precise behaviour of the Anti-Lock Braking System (ABS) during extreme braking manoeuvre.

Although the advantage in acceleration and braking without slipping of the tyres was not perceived by the Ferrari test drivers, the chronometer confirmed a minimal reduction in the laptime at Fiorano's track. The reduction of the wheel's weight on the total unsprung mass leads to a variable gain between 5% and 15%, making it difficult to perceive the advantage in ride comfort and road holding, also confirmed by the relevant literature.

At the conclusion of this extensive exposition, it is fitting to summarize the salient points gleaned from the Failure Modes and Effects Analysis.

The analysis highlights the five major challenges associated with developing a wheel made from unconventional materials, as detailed in Section *2.7 Failure Mode and Effect Analysis application*. The primary concern is the structural integrity of the wheel, which must be able to withstand the rigors of rough terrain and the cyclic, repetitive loads applied throughout its lifespan. These challenges are similar to those faced by most wheels made from metal alloys, and these have been compared with a reference aluminium wheel. However, there are other unique challenges that stem from the use of Carbon Fibre Reinforced Polymers as the chosen material and the design of the wheel, which is made up of moulded wheel assembled with inserts and a backplate aluminium alloy. Some of the specific challenges include the temperature behaviour of the epoxy matrix, environmental aging, and the process of assembling the wheel within the car.

Fatigue tests were conducted on the wheels after being numerically analysed. These tests showed that for sports car wheels, the cornering fatigue test is the preferred method since both wheels tested under radial fatigue showed no weaknesses. Therefore, it can be confirmed that the dimensioning load for sports car wheels is the bending moment.

The numerical analysis results can detect weaknesses in both wheels in advance, with greater precision on wheels made of traditional materials. However, an accurate stress-

life curve is still necessary. For wheels made of composite material, the Tsai-Wu failure index was used, with a high safety margin of 1.67, due to the material's first application.

The experimental tests confirmed that the aluminium wheel was oversized, and the initiation points of the cracks are strongly influenced by the wheel's style, as confirmed in the literature. The wheel made of composite material successfully passed the test, showing a different fatigue behaviour compared to metal alloys. During the test, the stiffness of the wheel decreased with a globally linear trend until it reached a certain level of aging, after which it accelerated. This occurred when the foam inside had been considerably damaged and started to detach from the laminate. For the tested wheel, this acceleration point was reached just after a 20% initial stiffness loss. Therefore, the cornering fatigue test can also be considered a "litmus test" for verifying the construction quality of the wheel.

The lateral and radial impact tests were both useful in understanding the strength of the composite wheel. These tests are unlikely to cause aluminium alloys to fail, given the experience gained over the years on these. Additionally, Ferrari exclusively uses only Flow-Forming production technology to manufacture the barrel of aluminium wheels, which deforms the forged or cast blank on the rim mould, resulting in a lighter barrel without compromising its impact resistance by locally yielding the material.

Surprisingly, the aluminium-composite comparative tests showed that the laboratory and road tests were unrelated. The aluminium wheel performed well in laboratory tests, while the composite wheel passed the test, showing areas for improvement, particularly by optimizing the layup of the barrel in the inner flange area. However, the experimental test conducted in the vehicle, in which the car was driven over an obstacle of predetermined dimensions, demonstrated how excellent the composite wheel is at absorbing roughness and impacts from the ground. The impact speeds against the obstacle at which damage to the rim or the undrivability of the car were found are the same for both materials. The difference is that where the composite material cracks, the aluminium alloy deforms.

From a customer's point of view, a CFRP rim slowly loses air from the rim, allowing the vehicle to be driven safely. On the other hand, a deformed alloy rim causes strong vibrations and imbalances in the vehicle, making it undrivable and forcing the user to stop the car and change the wheel. The failure mode is therefore a slow loss of air from the rim, which is detected by the TPMS sensor, making the failure mode safe and predictable. Finally, a more in-depth diagnosis of why there is no correlation between bench and vehicle tests and how to make bench tests more representative will be an important topic for further development.

An inherent feature of all composite materials made with epoxy resin is their ability to withstand high temperatures. This was the most critical point that emerged from the FMEA, particularly in terms of the resistance to the high thermal loads generated by the braking system of a sports car. The supplier has proposed equipping the rim with a thermal barrier coating, which significantly lowers temperatures.

Laboratory tests were conducted to determine the structural limit of the component, followed by an analysis of the component in the vehicle on customer routes in the

mountains and on the track. The result was a safe component, with temperatures generated by the braking system that can only become critical due to misuse on the track. Furthermore, the failure mode of the wheel subjected to heat stroke is, as in the radial impact test, tyre deflation, keeping the failure mode detectable.

Thanks to the development of a proprietary algorithm by Ferrari and a special thermal tape applied 360° on the barrel, it is possible to determine in advance the driving conditions on the track that could push the component to the limit. The driver is then warned to perform certain manoeuvres to cool down the component and avoid possible damage, which can then be unequivocally controlled by the dealer thanks to the thermal tape on the rim. This system further enhances the safety of the component, lowering the RPN index of the FMEA.

The thermal barrier coating on the rim is porous and appears light in colour and reflective. To perform at its best, it needs to be cleaned frequently. In order to be able to remove it in the near future, further development of epoxy matrices compatible with HP-RTM processes with higher Tg will be needed.

The fourth aspect to consider is the attachment of the wheel to the vehicle.

The analytical calculation of the installation of an aluminium wheel and a composite wheel was reviewed, and the following conclusions were drawn. The clamped assembly made up of the composite wheel is 3.4 times more yielding compared to the aluminium wheel. Although the bolting preload is comparable, as it mainly depends on the tangential forces that try to make the rim slide on the brake disk, the dynamic variation of the preload on the wheel bolt depends on the lateral forces. On the wheel bolt installed with the composite rim, the load variation is more than twice that generated with an aluminium rim. Moreover, the variation of the compression load on the clamped members with the composite rim is just over half compared to the aluminium one.

In terms of experimental tests, wheel bolts tightening tests were performed in the laboratory on samples and full wheel rims.

The test on representative samples of the layup and the volume fraction of the composite rim allowed us to choose the highest value of the volume fraction with which the lowest embedment is obtained after thermal cycling.

The validation of the bench bolt tightening was carried out after choosing to increase the tightening torque from 120 Nm to 150 Nm to prevent joint relaxation phenomena due to the combination of thermal and dynamic effects. The resulting preload on the test demonstrated that 25% more torque than the aluminium rim converted into approximately 25% screw preload. Furthermore, the friction between the rim cones and stud and on the thread was constant over the 20 tightenings. The tightening test with the thermal cycle to simulate the thermal effects to which the rim will be subjected in the vehicle reaffirmed how the tightening is constant over all ten repetitions. Additionally, it was observed that the clamping members settled after the second tightening and showed a tendency to flatten from the fourth tightening onwards.

The last but not least important aspect is the wheel's resistance to environmental conditions and daily use over time. In particular, the aspect of galvanic chains that may

occur between components made of different materials in contact with an electrolyte fluid was studied. The salt spray test was used for this purpose. Three galvanic chains were mainly found in the first test: aluminium insert with carbon fibre, anti-rotational pin in steel with aluminium insert, and alumina of the thermal barrier coating with the carbon fibre.

To address these issues, the design of the aluminium insert was optimized, and the thickness of the hard anodizing of the aluminium was increased to insulate it. The steel anti-rotational dowel pins were replaced with inert fiberglass dowel pins, and a double plies of glass fibre was added on the surfaces where the thermal barrier coating is applied as an insulator between the alumina of the thermal barrier and the carbon fibre.

These improvements have substantially interrupted the galvanic chains. However, special attention must be given to the masking of the wheel during the application of the thermal barrier. If alumina powder is interposed between the composite and the subsequent aesthetic coating, the alumina could react to form aluminium oxide, which swells the paint, creating an unwelcome blistering effect on the surface.

In conclusion, the development of the new composite wheel design has addressed several critical aspects, from mechanical performance to environmental resistance.

Overall, the new composite wheel design shows promising results for high-volume production of reliable and efficient wheels for sports cars. It represents a significant step forward in the field of automotive engineering and paves the way for further developments in composite materials and their applications in the automotive industry.

Acknowledgements

The author would like to thank *Ferrari* for the opportunity to undertake this interesting educational path, which has allowed him to learn a different methodological approach to problem analysis starting from the search and study of existing literature. This has enabled him to better understand the causes of problems and to develop effective solutions.

The author would also like to thank *Carbon Revolution* for their technical support on composite wheel investigation.

References

[1] Merriam-Webster.com Dictionary, "Wheel.," (n.d.). https://www.merriam-webster.com/dictionary/wheel (accessed October 25, 2022).

[2] G. Genta, L. Morello, The Automotive Chassis, Springer New York, 2009. https://doi.org/10.1007/978-1-4020-8676-2.

[3] G. Leister, Passenger car tires and wheels: Development - manufacturing - application, Springer International Publishing, 2018. https://doi.org/10.1007/978-3-319-50118-5.

[4] J. Kinstler, The Science and Methodology of SAE Wheel Fatigue Test Specifications, SAE Transactions. 114 (2005) 816–826. https://www.jstor.org/stable/44718964.

[5] SAE J328:2021 Wheels - Passenger Car and Light Truck Performance Requirements and Test Procedures, SAE Technical Papers. (2021). https://doi.org/10.4271/J328_202107.

[6] ISO 3006:2015 Road vehicles — Passenger car wheels for road use — Test methods, ISO Standard. (2015).

[7] JIS D 4103:2015 Automobile parts - Wheels - Performance requirements and marking, Japanese Industrial Standard. (2015).

[8] GB/T 5334-2005 Performance requirements and test methods of passenger car wheels, National Standard of the People's Republic of China. (2005).

[9] ECE R124. Regulation No 124 of the Economic Commission for Europe of the United Nations (UN/ECE) — Uniform provisions concerning the approval of wheels for passenger cars and their trailers., (2006).

[10] SAE J2562:2021 Biaxial Wheel Fatigue Test, SAE Technical Papers. (2021).

[11] V. Grubisic, G. Fischer, Automotive Wheels, Method and Procedure for Optimal Design and Testing, SAE Transactions. 92 (1983) 508–525. https://www.jstor.org/stable/44644390.

[12] V. Grubisic, G. Fischer, Procedure for optimal lightweight design and durability testing of wheels, International Journal of Vehicle Design. 5 (1984) 659–671.

[13] F. Ballo, R. Frizzi, G. Mastinu, D. Mastroberti, G. Previati, C. Sorlini, Lightweight Design and Construction of Aluminum Wheels, in: SAE Technical Papers, SAE International, 2016. https://doi.org/10.4271/2016-01-1575.

[14] R. Shang, W. Altenhof, H. Hu, N. Li, Rotary Fatigue Analysis of Forged Magnesium Road Wheels, International Journal of Materials and Manufacturing. 1 (2009) 9–15. https://doi.org/10.2307/26282629.

[15] P.R. Raju, B. Satyanarayana, K. Ramji, K.S. Babu, Evaluation of fatigue life of aluminium alloy wheels under bending loads, Fatigue Fract Eng Mater Struct. 32 (2009) 119–126. https://doi.org/10.1111/j.1460-2695.2008.01316.x.

[16] L. Wang, Y. Chen, C. Wang, Q. Wang, Fatigue life analysis of aluminum wheels by simulation of rotary fatigue test, Strojniski Vestnik/Journal of Mechanical Engineering. 57 (2011) 31–39. https://doi.org/10.5545/sv-jme.2009.046.

[17] M. Firat, U. Kocabicak, Analytical durability modeling and evaluation-complementary techniques for physical testing of automotive components, Eng Fail Anal. 11 (2004) 655–674. https://doi.org/10.1016/j.engfailanal.2003.05.018.

[18] U. Kocabicak, M. Firat, Numerical analysis of wheel cornering fatigue tests, Eng Fail Anal. 8 (2001) 339–354. https://doi.org/10.1016/S1350-6307(00)00031-5.

[19] X. Wang, X. Zhang, Simulation of dynamic cornering fatigue test of a steel passenger car wheel, Int J Fatigue. 32 (2010) 434–442. https://doi.org/10.1016/j.ijfatigue.2009.09.006.

[20] Z.G. Zheng, T. Sun, X.Y. Xu, S.Q. Pan, S. Yuan, Numerical simulation of steel wheel dynamic cornering fatigue test, Eng Fail Anal. 39 (2014) 124–134. https://doi.org/10.1016/j.engfailanal.2014.01.021.

[21] A. Dey, H. Jugade, V. Jain, M. Adhikary, Cracking phenomena in automotive wheels: An insight, Eng Fail Anal. 105 (2019) 1273–1286. https://doi.org/10.1016/j.engfailanal.2019.01.069.

[22] S. Bhattacharyya, M. Adhikary, M.B. Das, S. Sarkar, Failure analysis of cracking in wheel rims - material and manufacturing aspects, Eng Fail Anal. 15 (2008) 547–554. https://doi.org/10.1016/j.engfailanal.2007.04.007.

[23] Z. Zheng, S. Yuan, T. Sun, S. Pan, Fractographic study of fatigue cracks in a steel car wheel, Eng Fail Anal. 47 (2015) 199–207. https://doi.org/10.1016/j.engfailanal.2014.09.010.

[24] M. Carboni, S. Beretta, A. Finzi, Defects and in-service fatigue life of truck wheels, Eng Fail Anal. 10 (2003) 45–57. https://doi.org/10.1016/S1350-6307(02)00036-5.

[25] M.M. Topaç, S. Ercan, N.S. Kuralay, Fatigue life prediction of a heavy vehicle steel wheel under radial loads by using finite element analysis, Eng Fail Anal. 20 (2012) 67–79. https://doi.org/10.1016/j.engfailanal.2011.10.007.

[26] E. Bonisoli, C. Rosso, S. Venturini, D. Rovarino, M. Velardocchia, Improvements on Design and Validation of Automotive Steel Wheels, in: Mechanisms and Machine Science, Springer Science and Business Media B.V., 2019: pp. 1639–1649. https://doi.org/10.1007/978-3-030-20131-9_162.

[27] M. Firat, R. Kozan, M. Ozsoy, O.H. Mete, Numerical modeling and simulation of wheel radial fatigue tests, Eng Fail Anal. 16 (2009) 1533–1541. https://doi.org/10.1016/j.engfailanal.2008.10.005.

[28] P.R. Raju, B. Satyanarayana, K. Ramji, K.S. Babu, Evaluation of fatigue life of aluminum alloy wheels under radial loads, Eng Fail Anal. 14 (2007) 791–800. https://doi.org/10.1016/j.engfailanal.2006.11.028.

[29] L. Chen, S. Li, H. Chen, D.M. Saylor, S. Tong, Study on the design method of equal strength rim based on stress and fatigue analysis using finite element method,

Advances in Mechanical Engineering. 9 (2017). https://doi.org/10.1177/1687814017692698.

[30] K. Archibald, W. Lee, R. Rotundo, M. Melara, J. Gorsegner, C. Au, Development of a biaxial fatigue load file to emulate the services demanded of a motor sport vehicle, in: SAE Technical Papers, SAE International, 2012. https://doi.org/10.4271/2012-01-0798.

[31] D. Shang, X. Liu, Y. Shan, E. Jiang, Research on the stamping residual stress of steel wheel disc and its effect on the fatigue life of wheel, Int J Fatigue. 93 (2016) 173–183. https://doi.org/10.1016/j.ijfatigue.2016.08.020.

[32] P. Li, D.M. Maijer, T.C. Lindley, P.D. Lee, A through process model of the impact of in-service loading, residual stress, and microstructure on the final fatigue life of an A356 automotive wheel, Materials Science and Engineering A. 460–461 (2007) 20–30. https://doi.org/10.1016/j.msea.2007.01.076.

[33] J. Hu, L.X. Du, J.J. Wang, Q.Y. Sun, Cooling process and mechanical properties design of hot-rolled low carbon high strength microalloyed steel for automotive wheel usage, Mater Des. 53 (2014) 332–337. https://doi.org/10.1016/j.matdes.2013.07.036.

[34] M. Zanchini, D. Longhi, S. Mantovani, F. Puglisi, On the Ride Comfort Effect of Unsprung Mass Reduction Using a Composite Wheel Rim, in: V. Niola, A. Gasparetto, G. Quaglia, G. Carbone (Eds.), Mechanism and Machine Science, Springer, 2022: pp. 282–289. https://doi.org/10.1007/978-3-031-10776-4_33.

[35] W.F. Milliken, D.L. Milliken, Race car vehicle dynamics, Society of Automotive Engineers, 1995.

[36] A. Watts, A. Vallance, A. Whitehead, C. Hilton, A. Fraser, The Technology and Economics of In-Wheel Motors, 2010.

[37] R. Wang, Y. Chen, D. Feng, X. Huang, J. Wang, Development and performance characterization of an electric ground vehicle with independently actuated in-wheel motors, J Power Sources. 196 (2011) 3962–3971. https://doi.org/10.1016/j.jpowsour.2010.11.160.

[38] T.Z. Shi, D.F. Wang, S.M. Chen, Investigation of Negative Influences on Ride Comfort Performance of In-Wheel Motor Vehicles with High Unsprung Mass, 2015.

[39] W. Wang, X. Chen, J. Wang, Unsprung mass effects on electric vehicle dynamics based on coordinated control scheme, in: 2019 American Control Conference (ACC), IEEE, 2019: pp. 971–976.

[40] D. Hrovat, Influence of unsprung weight on vehicle ride quality, J Sound Vib. 124 (1988) 497–516. https://doi.org/10.1016/S0022-460X(88)81391-9.

[41] Froes F. H., Eliezer D., Aghion E., The science, technology, and applications of magnesium, Jom. 50 (1998) 30–34. https://doi.org/10.1007/s11837-998-0411-6.

[42] M. Zanchini, D. Longhi, S. Mantovani, F. Puglisi, On the ride comfort effect of unsprung mass reduction using a Composite Wheel Rim, in: The International Conference of IFToMM ITALY, 2022: pp. 282–289. https://doi.org/10.1007/978-3-031-10776-4_33.

[43] F. Lei, R. Qiu, Y. Bai, C. Yuan, An integrated optimization for laminate design and manufacturing of a CFRP wheel hub based on structural performance, Structural and Multidisciplinary Optimization. 57 (2018) 2309–2321. https://doi.org/10.1007/s00158-017-1861-7.

[44] G. Anandraj, V. Chaudhari, S. Kangde, A Comprehensive Study on the Design and Development Methodology of Automotive Steel Wheel Rims Undergoing Highly Transient Cornering Events, in: SAE Technical Papers, SAE International, 2021. https://doi.org/10.4271/2021-01-0827.

[45] Y. Zhang, Y. Shan, X. Liu, T. He, An integrated multi-objective topology optimization method for automobile wheels made of lightweight materials, Structural and Multidisciplinary Optimization. 64 (2021) 1585–1605. https://doi.org/10.1007/s00158-021-02913-3.

[46] D. Wang, S. Zhang, W. Xu, Multi-objective optimization design of wheel based on the performance of 13° and 90° impact tests, International Journal of Crashworthiness. 24 (2019) 336–361. https://doi.org/10.1080/13588265.2018.1451229.

[47] J.H. Bae, K.C. Jung, S.H. Yoo, S.H. Chang, M. Kim, T. Lim, Design and fabrication of a metal-composite hybrid wheel with a friction damping layer for enhancement of ride comfort, Compos Struct. 133 (2015) 576–584. https://doi.org/10.1016/j.compstruct.2015.07.113.

[48] X. Jiang, H. Liu, R. Lyu, Y. Fukushima, N. Kawada, Z. Zhang, D. Ju, Optimization of Magnesium Alloy Wheel Dynamic Impact Performance, Advances in Materials Science and Engineering. 2019 (2019). https://doi.org/10.1155/2019/2632031.

[49] D. Wang, W. Xu, Y. Wang, J. Gao, Design and optimization of tapered carbon-fiber-reinforced polymer rim for carbon/aluminum assembled wheel, Polym Compos. 42 (2021) 253–270. https://doi.org/10.1002/pc.25822.

[50] SAE J3204:2020 Aftermarket Composite Wheels Made of Matrix Material and Fiber Reinforcement Intended for Normal Highway Use - Test Procedures and Performance Requirements, (n.d.). https://doi.org/10.4271/J3204_202009.

[51] S. Aggarwal, R. Elsen, Design and Fabrication of CFRP Wheel Centre for FSAE Race-Car, in: SAE Technical Papers, SAE International, 2019. https://doi.org/10.4271/2019-28-0117.

[52] F. Rondina, S. Taddia, L. Mazzocchetti, L. Donati, G. Minak, P. Rosenberg, A. Bedeschi, E. Dolcini, Development of full carbon wheels for sport cars with high-volume technology, Compos Struct. 192 (2018) 368–378. https://doi.org/10.1016/j.compstruct.2018.02.083.

[53] W. Chai, X. Liu, Y. Shan, X. Wan, E. Jiang, Research on simulation of the bending fatigue test of automotive wheel made of long glass fiber reinforced thermoplastic considering anisotropic property, Advances in Engineering Software. 116 (2018) 1–8. https://doi.org/10.1016/j.advengsoft.2017.11.004.

[54] A.P. Vassilopoulos, T. Keller, Fatigue of Fiber-reinforced Composites, 2011. https://doi.org/10.1007/978-1-84996-181-3.

[55] A.P. Vassilopoulos, Fatigue Life Prediction of Composites and Composite Structures, 2020.

[56] K.L. Reifsnider, A. Talug, Analysis of fatigue damage in composite laminates, Int J Fatigue. 2 (1980) 3–11. https://doi.org/10.1016/0142-1123(80)90022-5.

[57] P. Alam, D. Mamalis, C. Robert, C. Floreani, C.M. Ó Brádaigh, The fatigue of carbon fibre reinforced plastics - A review, Compos B Eng. 166 (2019) 555–579. https://doi.org/10.1016/j.compositesb.2019.02.016.

[58] T. Fujii, F. Lin, Fatigue Behavior of a Plain-Woven Glass Fabric Laminate under Tension/Torsion Biaxial Loading, J Compos Mater. 29 (1995) 573–590. https://doi.org/10.1177/002199839502900502.

[59] S.W. Tsai, E.M. Wu, A General Theory of Strength for Anisotropic Materials, J Compos Mater. 5 (1971) 58–80. https://doi.org/10.1177/002199837100500106.

[60] M. Zanchini, D. Longhi, S. Mantovani, F. Puglisi, M. Giacalone, Fatigue and failure analysis of aluminium and composite automotive wheel rims: Experimental and numerical investigation, Eng Fail Anal. 146 (2023) 107064. https://doi.org/10.1016/j.engfailanal.2023.107064.

[61] K. Dang Van, G. Cailletaud, J. Flavenot, A. le Douaron, H.P. Lieurade, Criterion for high cycle fatigue failure under multiaxial loading, in: M.W. Brown, K.J. Miller (Eds.), Biaxial and Multiaxial Fatigue, EGF 3, Mechanical Engineering Publications, London, 1989: pp. 459–478.

[62] K. Dang Van, B. Griveau, O. Message, On a new multiaxial fatigue limit criterion: theory and application, in: M.W. Brown, K.J. Miller (Eds.), Biaxial and Multiaxial Fatigue EGF 3, Mechanical Engineering Publications, London, 1989: pp. 479–496.

[63] M. Biancalana, Zanchini M, Wheel rim of a vehicle, EP3650243, 2021.

[64] S. Wang, S. Bhandari, S.C. Chaduvula, M.J. Atallah, J.H. Panchal, K. Ramani, Secure Collaboration in Engineering Systems Design, J Comput Inf Sci Eng. 17 (2017). https://doi.org/10.1115/1.4036615.

[65] E. Red, D. French, G. Jensen, S.S. Walker, P. Madsen, Emerging Design Methods and Tools in Collaborative Product Development, J Comput Inf Sci Eng. 13 (2013). https://doi.org/10.1115/1.4023917.

[66] SAE J175:2021 Wheels - Lateral Impact Test Procedure - Road Vehicles, (n.d.). https://doi.org/10.4271/J175_202107.

[67] AK-LH08:2006 Räder Anforderungen und Prüfungen, Arbeitskreis Lastenheft, Arbeitskreis der Firmen: Audi AG, Bayerische Motorenwerke AG, DaimlerChrysler AG, Porsche AG, Volkswagen AG., (n.d.).

[68] Q. Gao, Y. Shan, X. Wan, Q. Feng, X. Liu, 90-degree impact bench test and simulation analysis of automotive steel wheel, Eng Fail Anal. 105 (2019) 143–155. https://doi.org/10.1016/j.engfailanal.2019.06.097.

[69] G. Previati, F. Ballo, M. Gobbi, G. Mastinu, Radial impact test of aluminium wheels—Numerical simulation and experimental validation, Int J Impact Eng. 126 (2019) 117–134. https://doi.org/10.1016/j.ijimpeng.2018.12.002.

[70] X. Wan, Y. Shan, X. Liu, H. Wang, J. Wang, Simulation of biaxial wheel test and fatigue life estimation considering the influence of tire and wheel camber, Advances in Engineering Software. 92 (2016) 57–64. https://doi.org/10.1016/j.advengsoft.2015.11.005.

[71] F.M. Santiciolli, R. Möller, I. Krause, F.G. Dedini, Simulation of the scenario of the biaxial wheel fatigue test, Advances in Engineering Software. 114 (2017) 337–347. https://doi.org/10.1016/j.advengsoft.2017.08.006.

[72] ISO 2808:2019 Paints and varnishes — Determination of film thickness, ISO. (2019).

[73] ISO 2409:2020 Paints and varnishes — Cross-cut test, ISO. (2020).

[74] SAE J400:2022 Test for Chip Resistance of Surface Coatings, in: SAE Technical Papers, SAE International, 2022. https://doi.org/10.4271/680046.

[75] ISO 20567-1:2017 Paints and varnishes — Determination of stone-chip resistance of coatings — Part 1: Multi-impact testing, ISO. (2017).

[76] ISO 6270:2017 Paints and varnishes — Determination of resistance to humidity, ISO. (2017).

[77] SAE J2792:2015 Test Methodology for Evaluating the Chemical Compatibility of Wheel Finishes with Various Chemicals, SAE Technical Papers. (2015).

[78] ISO 14993:2018 Corrosion of metals and alloys — Accelerated testing involving cyclic exposure to salt mist, dry and wet conditions, ISO. (2018).

[79] SAE J2635:2015 Filiform Corrosion Test Procedure for Painted Aluminum Wheels and Painted Aluminum Wheel Trim, SAE Technical Papers. (2015). www.sae.org.

[80] SAE J2527:2017 Performance Based Standard for Accelerated Exposure of Automotive Exterior Materials Using a Controlled Irradiance Xenon-Arc Apparatus, SAE Technical Papers. (2017).

[81] SAE J2633:2019 Wheel and Wheel Trim Weathering Testing for Paint Coatings, SAE Technical Papers. (2019).

[82] SAE J2316:2021 Performance Requirements and Test Procedures for Aftermarket Wheel Fastening Systems on Passenger Cars and Light Trucks, in: SAE Technical Papers, SAE International, 2021. https://doi.org/10.4271/820340.

[83] S. v. Hoa, 2.1 Manufacturing of Composites – An Overview, in: Comprehensive Composite Materials II, Elsevier, 2018: pp. 1–23. https://doi.org/10.1016/B978-0-12-803581-8.10074-8.

[84] Processes - Discover Composites, Https://Discovercomposites.Com/What-Are-Composites/Processes/. (n.d.).

[85] O.A. Ekuase, N. Anjum, V.O. Eze, O.I. Okoli, A Review on the Out-of-Autoclave Process for Composite Manufacturing, Journal of Composites Science. 6 (2022). https://doi.org/10.3390/jcs6060172.

[86] T. de Souza, T. Bastian, T. Lawson, A. Denmead, WO2022241510A1 ATTACHMENT ARRANGEMENT FOR COMPOSITE WHEELS, 2022.

[87] T. Gueorguiev, M. Kokalarov, B. Sakakushev, Recent Trends in FMEA Methodology, in: 2020 7th International Conference on Energy Efficiency and Agricultural Engineering, EE and AE 2020 - Proceedings, Institute of Electrical and Electronics Engineers Inc., 2020. https://doi.org/10.1109/EEAE49144.2020.9279101.

[88] G. Ványi, Improving the effectiveness of FMEA analysis in automotive – a case study, Acta Universitatis Sapientiae, Informatica. 8 (2016) 82–95. https://doi.org/10.1515/ausi-2016-0005.

[89] SAE J1739: 2009 Potential Failure Mode and Effects Analysis in Design (Design FMEA), Potential Failure Mode and Effects Analysis in Manufacturing and Assembly Processes (Process FMEA), SAE Technical Papers. (2009).

[90] ISO 9001:2015 Quality management systems - Requirements, ISO. (2015).

[91] IATF 16949:2016 - Technical Specification Quality management system requirements for automotive production and relevant service parts organisations., IATF Books, Standards and Publications. (2016).

[92] G. Goldoni, S. Mantovani, Damage modelling strategies for unidirectional laminates subjected to impact using CZM and orthotropic plasticity law, Compos Struct. 275 (2021). https://doi.org/10.1016/j.compstruct.2021.114493.

[93] Y. Zhou, D. Jiang, Y. Xia, Tensile mechanical behavior of T300 and M40J fiber bundles at different strain rate, J Mater Sci. 36 (2001) 919–922. https://doi.org/10.1023/A:1004803202658.

[94] N.S. El-Tayeb, R.M. Gadelrab, A.W. Profe, Friction and wear properties of E-glass fiber reinforced epoxy composites under different sliding contact conditions, Wear. 192 (1996) 112–117. https://doi.org/10.1016/0043-1648(95)06770-1.

[95] A.J. Denmead, M.D. Silcock, T. Corbett, S. Agius, B. Trippit, Shaped Preform for Face Portion of a Composite Wheel, WO/2019/033173, 2019.

[96] M. Holmes, High volume composites for the automotive challenge, Reinforced Plastics. 61 (2017) 294–298. https://doi.org/10.1016/j.repl.2017.03.005.

[97] L. de Lorenzis, F. Grancagnolo, A. L'Erario, A. Maffezzoli, A. Miccoli, S. Rella, M. Spedicato, G. Zavarise, Analysis and Characterization of the Mechanical Structure

for the I-Tracker of the Mu2e Experiment, Nucl Phys B Proc Suppl. 248–250 (2014) 134–136. https://doi.org/10.1016/j.nuclphysbps.2014.02.027.

[98] K. Kluger, Fatigue life estimation for 2017A-T4 and 6082-T6 aluminium alloys subjected to bending-torsion with mean stress, Int J Fatigue. 80 (2015) 22–29. https://doi.org/10.1016/j.ijfatigue.2015.05.005.

[99] S. Mantovani, I. lo Presti, L. Cavazzoni, A. Baldini, Influence of Manufacturing Constraints on the Topology Optimization of an Automotive Dashboard, Procedia Manuf. 11 (2017) 1700–1708. https://doi.org/10.1016/j.promfg.2017.07.296.

[100] K. Dang Van, G. Cailletaud, J. Flavenot, A. le Douaron, H.P. Lieurade, Criterion for high cycle fatigue failure under multiaxial loading, in: M.W. Brown, K.J. Miller (Eds.), Biaxial and Multiaxial Fatigue, EGF 3, Mechanical Engineering Publications, London, 1989: pp. 459–478.

[101] K. Dang Van, B. Griveau, O. Message, On a new multiaxial fatigue limit criterion: theory and application, in: M.W. Brown, K.J. Miller (Eds.), Biaxial and Multiaxial Fatigue EGF 3, Mechanical Engineering Publications, London, 1989: pp. 479–496.

[102] S.W. Tsai, E.M. Wu, A General Theory of Strength for Anisotropic Materials, J Compos Mater. 5 (1971) 58–80. https://doi.org/10.1177/002199837100500106.

[103] F. Ballo, M. Gobbi, G. Mastinu, G. Previati, Motorcycle tire modeling for the study of tire-rim interaction, Journal of Mechanical Design, Transactions of the ASME. 138 (2016). https://doi.org/10.1115/1.4032470.

[104] R.G. Pelle, FEM Simulation of the Tire/Rim Seating Process, Tire Sci Technol. 22 (1994) 76–98. https://doi.org/10.2346/1.2139537.

[105] F. Ballo, G. Previati, G. Mastinu, F. Comolli, Impact tests of wheels of road vehicles: A comprehensive method for numerical simulation, Int J Impact Eng. 146 (2020). https://doi.org/10.1016/j.ijimpeng.2020.103719.

[106] C.L. Chang, S.H. Yang, Simulation of wheel impact test using finite element method, Eng Fail Anal. 16 (2009) 1711–1719. https://doi.org/10.1016/j.engfailanal.2008.12.010.

[107] X. Wan, X. Liu, Y. Shan, E. Jiang, H. Yuan, Numerical and experimental investigation on the effect of tire on the 13° impact test of automotive wheel, Advances in Engineering Software. 133 (2019) 20–27. https://doi.org/10.1016/j.advengsoft.2019.04.005.

[108] J. Stearns, T.S. Srivatsan, A. Prakash, P.C. Lam, Modeling the mechanical response of an aluminum alloy automotive rim, Materials Science and Engineering A. 366 (2004) 262–268. https://doi.org/10.1016/j.msea.2003.08.017.

[109] SAE J1441:2016 Subjective Rating Scale for Vehicle Ride and Handling, SAE Technical Paper. (2016).

[110] J.D. Parisen, Automobile Wheel Attachment Design Considerations, SAE Transactions. (1982) 1289–1295.

[111] J.D. Varin, Wheel Attachment Failures in Light-Duty Vehicles, Journal of Failure Analysis and Prevention. 17 (2017) 660–671. https://doi.org/10.1007/s11668-017-0297-0.

[112] M. Bailey, J. Bertoch, Mechanisms of wheel separations, SAE Technical Paper, 2009.

[113] D. Croccolo, M. de Agostinis, N. Vincenzi, Failure analysis of bolted joints: Effect of friction coefficients in torque-preloading relationship, Eng Fail Anal. 18 (2011) 364–373. https://doi.org/10.1016/j.engfailanal.2010.09.015.

[114] V. VDI, 2230 Blatt 1: Systematic Calculation of High Duty Bolted Joints-Joints with One Cylindrical Bolt, (2003).

[115] D. Croccolo, M. de Agostinis, N. Vincenzi, Influence of tightening procedures and lubrication conditions on titanium screw joints for lightweight applications, Tribol Int. 55 (2012) 68–76. https://doi.org/10.1016/j.triboint.2012.05.010.

[116] ISO 683-17:1999 Heat-treated steels, alloy steels and free-cutting steels — Part 17: Ball and roller bearing steels, ISO. (1999).

[117] AMSQQA225C Aluminum and Aluminum Alloy, Bar, Rod, Wire, or Special Shapes; Rolled, Drawn, or Cold Finished; General Specification For Stabilized , SAE Standards. (2018).

[118] R.G. Budynas, J.K. Nisbett, Shigley's mechanical engineering design, McGraw-hill New York, 2011.

[119] J. Bickford, Handbook of bolts and bolted joints, CRC press, 1998.

[120] G. Welsch, R. Boyer, E.W. Collings, Materials properties handbook: titanium alloys, ASM international, 1993.

[121] ISO 262:1998 - ISO general purpose metric screw threads — Selected sizes for screws, bolts and nuts, ISO. (1998).

[122] K.H. Brown, C. Morrow, S. Durbin, A. Baca, Guideline for Bolted Joint Design and Analysis: Version 1.0, n.d. http://www.ntis.gov/help/ordermethods.asp?loc=7-4-0#online.

[123] J.H. Bickford, Introduction to the Design and Behavior of Bolted Joints, CRC Press, 2007. https://doi.org/10.1201/9780849381874.

[124] E.M. Pulling, S. Brooks, C. Fulcher, K. Miller, Guideline for Bolt Failure Margins of Safety Calculations, Internal Sandia Report. (2005).

[125] G. Niemann, Elementi di macchine, ETS, 1986.

[126] R.E. Little, Bolted joints-how much give, Machine Design. 39 (1967) 173.

[127] R.C. Juvinall, Fundamentals of machine component design, (2007).

[128] C.C. Osgood, Saving weight on bolted joints, Machine Design. 51 (1979) 128–133.

[129] J.C. Musto, N.R. Konkle, Computation of member stiffness in the design of bolted joints, Journal of Mechanical Design, Transactions of the ASME. 128 (2006) 1357–1360. https://doi.org/10.1115/1.2338578.

[130] Aluminum Standards and Data, (2000).

[131] Metals Handbook Vol. 2: Properties and Selection: Nonferrous Alloys and Special-Purpose Materials, ASM International, 1990.

[132] ASTM G99-95a:2000 Standard Test Method for Wear Testing with a Pin-on-Disk Apparatus, ASTM. (2000).

[133] V. Kliment, Volumetric wear analysis of the explanted components of the hip joint, 2018.

[134] H. Kopfer, C. Friedrich, M. de Agostinis, D. Croccolo, FRICTION CHARACTERISTICS IN LIGHT WEIGHT DESIGN FOCUSING BOLTED JOINTS, 2012. http://www.asme.org/about-asme/terms-of-use.

[135] K.G. Budinski, Tribological properties of titanium alloys*, 1991.

[136] D.B. Shah, K.M. Patel, S.J. Joshi, B.A. Modi, A.I. Patel, V. Pariyal, Thermo-mechanical characterization of carbon fiber composites with different epoxy resin systems, Thermochim Acta. 676 (2019) 39–46. https://doi.org/10.1016/j.tca.2019.03.041.

[137] J.P. Greene, Thermoset Polymers, Automotive Plastics and Composites. (2021) 175–190. https://doi.org/10.1016/B978-0-12-818008-2.00002-7.

[138] B. Wunderlich, Nature of the glass transition and its determination by thermal analysis, in: ASTM Special Technical Publication, 1994: pp. 17–31. https://doi.org/10.1520/stp15363s.

[139] J.D. Menczel, R.B. Prime, P.K. Gallagher, Introduction, in: Thermal Analysis of Polymers, John Wiley & Sons, Inc., Hoboken, NJ, USA, 2008: pp. 1–6. https://doi.org/10.1002/9780470423837.ch1.

[140] R.P. Chartoff, J.D. Menczel, S.H. Dillman, Dynamic Mechanical Analysis (DMA), in: Thermal Analysis of Polymers, John Wiley & Sons, Inc., Hoboken, NJ, USA, 2008: pp. 387–495. https://doi.org/10.1002/9780470423837.ch5.

[141] E.A. Collins, J. Bares, F.W. Billmeyer, Experiments in polymer science, (1973).

[142] J.D. Ferry, Viscoelastic properties of polymers, John Wiley & Sons, 1980.

[143] ASTM D7028:2007 Standard test method for glass transition temperature (DMA Tg) of polymer matrix composites by dynamic mechanical analysis (DMA), ASTM. (2015).

[144] Y. Ozgurluk, K.M. Doleker, H. Ahlatci, A.C. Karaoglanli, Investigation of calcium–magnesium-alumino-silicate (CMAS) resistance and hot corrosion behavior of YSZ and La2Zr2O7/YSZ thermal barrier coatings (TBCs) produced with CGDS method, Surf Coat Technol. 411 (2021). https://doi.org/10.1016/j.surfcoat.2021.126969.

[145] V.I. Bogdanovich, M.G. Giorbelidze, Analysis of the ceramic layer microstructure influence on plasma spray thermal barrier coating performance, in: IOP Conf Ser Mater Sci Eng, Institute of Physics Publishing, 2018. https://doi.org/10.1088/1757-899X/286/1/012008.

[146] M.M. Dokur, G. Goller, Processing and characterization of CYSZ/Al2O3 and CYSZ/Al2O3+YSZ multilayered thermal barrier coatings, Surf Coat Technol. 258 (2014) 804–813. https://doi.org/10.1016/j.surfcoat.2014.07.077.

[147] H.R. Abedi, M. Salehi, A. Shafyei, Microstructural, mechanical and thermal shock properties of triple-layer TBCs with different thicknesses of bond coat and ceramic top coat deposited onto polyimide matrix composite, Ceram Int. 44 (2018) 6212–6222. https://doi.org/10.1016/j.ceramint.2018.01.006.

[148] H. Kim, J. Kim, J. Lee, M.W. Lee, Thermal barrier coating for carbon fiber-reinforced composite materials, Compos B Eng. 225 (2021). https://doi.org/10.1016/j.compositesb.2021.109308.

[149] A. Liu, M. Guo, J. Gao, M. Zhao, Influence of bond coat on shear adhesion strength of erosion and thermal resistant coating for carbon fiber reinforced thermosetting polyimide, Surf Coat Technol. 201 (2006) 2696–2700. https://doi.org/10.1016/j.surfcoat.2006.05.012.

[150] R. Wang, D. Song, W. Liu, X. He, Effect of arc spraying power on the microstructure and mechanical properties of Zn-Al coating deposited onto carbon fiber reinforced epoxy composites, Appl Surf Sci. 257 (2010) 203–209. https://doi.org/10.1016/j.apsusc.2010.06.065.

[151] S. Sens, E. Kwok, M.D. Silcock, A. Brighton, A.J. Denmead, N. Jones, H. Howse, WO2016168899A1 Method of producing thermally protected composite, 2015.

[152] ASTM D4541-17 Standard Test Method for Pull-Off Strength of Coatings Using Portable Adhesion Testers, ASTM. (2017).

[153] L. Boccarusso, M. Durante, A. Formisano, A. Langella, F.M.C. Minutolo, Thermal Barrier Coatings (TBCs) Produced by Air Plasma Spray: Repair by Grinding and Waterjet (WJ) Processes, in: Key Eng Mater, Trans Tech Publications Ltd, 2022: pp. 1746–1755. https://doi.org/10.4028/p-84e1pv.

[154] Monte Bondone da Trento, Https://Www.Idiaridellabicicletta.Com/Monte-Bondone-Da-Trento/. (2020).

[155] Circuito di Fiorano, Https://It.Wikipedia.Org/Wiki/Circuito_di_Fiorano. (n.d.).

[156] Ferrari Capital Markets Day, Https://Www.Ferrari.Com/It-IT/Corporate/Articles/Ferrari-Capital-Markets-Day-2022. (2022).

[157] Mary Frances Gerety - Wikipedia, Https://En.Wikipedia.Org/Wiki/Mary_Frances_Gerety. (n.d.).

[158] Y. Chen, M. Li, T. Su, X. Yang, Mechanical degradation and corrosion characterization of riveted joints for CFRP/Al stacks in simulated marine environments, Eng Fail Anal. 137 (2022). https://doi.org/10.1016/j.engfailanal.2022.106382.

[159] Y. Chen, M. Li, X. Yang, K. Wei, Durability and mechanical behavior of CFRP/Al structural joints in accelerated cyclic corrosion environments, Int J Adhes Adhes. 102 (2020). https://doi.org/10.1016/j.ijadhadh.2020.102695.

[160] V. Fiore, L. Calabrese, E. Proverbio, R. Passari, A. Valenza, Salt spray fog ageing of hybrid composite/metal rivet joints for automotive applications, Compos B Eng. 108 (2017) 65–74. https://doi.org/10.1016/j.compositesb.2016.09.096.

[161] T. Morimoto, J. Koyanagi, Cathodic protection tests for the galvanic corrosion of airframe grade CFRP/Al systems, in: 57th AIAA/ASCE/AHS/ASC Structures, Structural Dynamics, and Materials Conference, American Institute of Aeronautics and Astronautics Inc, AIAA, 2016. https://doi.org/10.2514/6.2016-1654.

[162] R.H. Martin, 3.32 Degradation of Polymer Matrix Composites, n.d. www.merl-ltd.co.uk.

[163] R. Darolia, Thermal barrier coatings technology: Critical review, progress update, remaining challenges and prospects, International Materials Reviews. 58 (2013) 315–348. https://doi.org/10.1179/1743280413Y.0000000019.

[164] H.R. Abedi, M. Salehi, A. Shafyei, Mechanical and thermal properties of double-layer and triple-layer thermal barrier coatings with different ceramic top coats onto polyimide matrix composite, Ceram Int. 43 (2017) 12770–12780. https://doi.org/10.1016/j.ceramint.2017.06.164.

[165] ASTM B117-19 Standard Practice for Operating Salt Spray (Fog) Apparatus, ASTM. (2019).

[166] ISO 9227:2017 Corrosion tests in artificial atmospheres — Salt spray tests, ISO. (2017).

[167] ISO 14993:2018 Corrosion of metals and alloys — Accelerated testing involving cyclic exposure to salt mist, dry and wet conditions, ISO. (2018).

[168] M. Mandel, L. Krüger, FE-simulation of Galvanic Corrosion Susceptibility of two Rivet Joints Verified by Immersion Tests, in: Mater Today Proc, Elsevier Ltd, 2015: pp. S197–S204. https://doi.org/10.1016/j.matpr.2015.05.010.

[169] H.P. Hack, 2.07 Galvanic Corrosion, n.d.

[170] M. Schneider, K. Kremmer, C. Lämmel, K. Sempf, M. Herrmann, Galvanic corrosion of metal/ceramic coupling, Corros Sci. 80 (2014) 191–196. https://doi.org/10.1016/j.corsci.2013.11.024.

[171] K.-H. Tostmann, Korrosion, John Wiley & Sons, 2001.

[172] T. Magnin, Recent advances in the environment sensitive fracture mechanisms of aluminium alloys, Materials Science Forum. 217–222 (1996) 83–94. https://doi.org/10.4028/www.scientific.net/msf.217-222.83.

[173] A.C. UMAMAHESHWER RAO, V. VASU, M. GOVINDARAJU, K.V.S. SRINADH, Stress corrosion cracking behaviour of 7xxx aluminum alloys: A literature review, Transactions of Nonferrous Metals Society of China (English Edition). 26 (2016) 1447–1471. https://doi.org/10.1016/S1003-6326(16)64220-6.

[174] L. Schwarmann, Comparison of the strength and damage tolerance of aluminium alloys, 1986.

[175] International Alloy Designations and Chemical Composition Limits for Wrought Aluminum and Wrought Aluminum Alloys, (2018). www.aluminum.org.